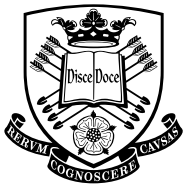

The University Of Sheffield.

Prediction of The Strength of Human Long Bone Using CT Based Finite Element Method

By:

Zainab Altai

A thesis submitted in partial fulfilment of the requirements for the degree of

Doctor of Philosophy

The University of Sheffield

Faculty of Engineering

Department of Mechanical Engineering

September 2018

The University Of Sheffield.

INSIGNEO
Institute for *in silico* Medicine

Prediction of The Strength of Human Long Bone Using CT Based Finite Element Method

By:

Zainab Altai

Supervisors:
Dr. Xinshan Li
Prof. Marco Viceconti

A thesis submitted in partial fulfilment of the requirements for the degree of Doctor of Philosophy

The University of Sheffield

Faculty of Engineering

Department of Mechanical Engineering

September 2018

ABSTRACT

Bone fracture is one of the most common injuries during life, both during the early age of childhood and when we get old. The main cause of fractures usually differs with age. For very young children (e.g. infants), fracture of bone is sometimes associated with child abuse as they have limited mobilities (e.g. non-ambulant). On the other hand, fracture of bone in the elderly usually occurs as result of bone disease and degeneration, such as osteoporosis. Hip fracture is the most common fracture at this age, with the percentage increasing in line with the growing risk of falls as one gets older. Fractures for these two age groups are particularly problematic because of the implications on the quality of life.

The discrimination of inflicted injury from accidental injury in children is very important to avoid the risk of further abuse, which could significantly affect the mental and physical development of the child. Computed tomography based finite element (CT/FE) models have been widely used to study the biomechanics of human bones. Although this technique has been extensively used in adults there are markedly fewer studies in children, mainly due to the lack of paediatric bone samples. Consequently, the current clinical method used to diagnose the cause of fractures in very young children is based on the clinical judgement and the description of the caretaker, with very little quantitative evidence. For example, until now, the injury tolerance (or bone strength) of a paediatric bone (within a certain age range) has been unclear. Consequently, there is a need for non-invasive tools in order to report on the paediatric bone strength under various loading conditions.

Predicting the risk of hip fracture in the elderly has major implications for the prevention of permanent disability, and the associated substantially reduced quality of life (due to reduced or a complete loss of mobility). Experimental investigation has reported that CT/FE models can accurately predict the strength of adult long bone, but the use of these strength predictions to discriminate patients at risk of fracture still needs further investigation, especially in respect to comparing their performance against the clinical gold standard, the bone mineral density (BMD) measurement.

In order to enhance our understanding of bone mechanics related to clinical diagnosis, therefore, this thesis investigated bone strength in these two distinct age groups. The work consisted of three studies detailed below.

Study I aimed to define the injury tolerance of very young children using a CT/FE model under bending and torsional loads. A range of femora strength of children aged from zero to three years old was reported under bending loads (0.25-27.9 Nm) and, for the first time, under torsional loads (1-31.4 Nm for external rotation and 1-30.7 Nm for internal rotation). These results were found to be in good agreement with the experimental data in the literature.

Study II applied the paediatric modelling approach to investigate a special case of reported spontaneous humeral fracture, which is still under debate. Three personalized humerus models were created spanning an age range of four to six months. Simulation results showed that spontaneous humeral fracture is highly unlikely to occur when an infant rolls from a prone to supine position without any external loads.

Study III aimed to improve the accuracy of the side fall CT/FE model in classifying fracture and non-fracture cases using a wide range of loading directions, and also attempts to achieve a more accurate prediction of fracture type, using three different boundary conditions: Linear, MPC and Contact model. The study showed that the Contact model achieved the biggest classification power improvement by an increase of 7% compared to BMD as a predictor. The MPC and Contact models were able to predict various hip fractures, including per-trochanteric fracture, which is rarely reported in the literature.

In conclusion, the CT/FE model is a valuable tool allowing the non-invasive investigation of bone strengths in a range of ages. In the paediatric application, this thesis reported, for the first time in the literature, a table of injury tolerance (under both bending and torsion) for very young children. It also successfully falsified the spontaneous humerus fracture hypothesis under the current assumptions. In the adult applications, a more refined boundary condition in the side fall FE model was proven to increase the classification accuracy and improve fracture type prediction. This places the FE method one step closer to more accurate predictions in fragile bone fractures.

LIST OF PUBLICATIONS

Altai, Z., Viceconti, M., Offiah, A.C., Li, X., 2018. Investigating the mechanical response of paediatric bone under bending and torsion using finite element analysis. Biomech. Model. Mechanobiol. 1–9. doi:10.1007/s10237-018-1008-9

Altai, Z., Qasim, M., Li, X., Viceconti, M., 2018. The effect of boundary constraints on patient classification using finite element predicted risk of fracture (in preparation).

Bhattacharya, P., **Altai, Z.**, Qasim, M., Viceconti1, M., 2018. A multiscale model to predict current absolute risk of femoral fracture in a postmenopausal population (Accepted). J Biomech.

Castro, A.P.G., **Altai, Z.**, Offiah, A.C., Shelmerdine, S.C., Arthurs, O.J., Li, X., Lacroix, D., 2018. Finite element modelling of the development infant femur using paired CT and MRI scans (submitted). Comput. Methods Biomech. Biomed. Engin.

Altai, Z., Viceconti, M., Li, X., Offiah, A.C. Spontaneous humeral fractures in infants while rolling from prone to supine position: CT based Finite element study (in preparation).

LIST OF CONFERENCE PROCEEDINGS

Altai, Z., Qasim, M., Li, X., Viceconti, M., (2016). Prediction of femur strength in sideways fall configuration using nonlinear contact analysis. Poster presented at the Insigneo Showcase in May 2016 (Sheffield, UK)

Altai, Z., Qasim, M., Li, X., Viceconti, M., (2016). Prediction of hip fracture risk using nonlinear contact analysis in sideways fall configuration. Presented at the 22nd Congress of the European Society of Biomechanics in July 2016 (Lyon. France)

Altai, Z., Viceconti, M., Li, X., Offiah, A.C. (2017). Prediction of paediatric femur under torsion loads. Poster presented at the Insigneo Showcase in May 2017 (Sheffield, UK)

Altai, Z., Viceconti, M., Li, X., Offiah, A.C. (2017) investigating the mechanical response of paediatric femur under torsion. Presented at the 23rd Congress of the European Society of Biomechanics in July 2017 (Seville, Spain)

Altai, Z., Qasim, M., Li, X., Viceconti, M., (2017). Non-linear Boundary Conditions for a more realistic prediction of femoral fracture during side-fall. Presented at the 14th U.S. National Congress on Computational Mechanics in July 2017 (Montreal, Canada)

Altai, Z., Viceconti, M., Li, X., Offiah, A.C. (2017). Investigating the mechanical response of the paediatric femur using computer models. Poster presented at the British Society of Paediatric Radiology National Meeting in November 2017 (Manchester, UK)

Altai, Z., Viceconti, M., Li, X., Offiah, A.C. (2018). Investigating a possible mechanism of spontaneous humeral fractures in infants while rolling. Poster presented at the Insigneo Showcase in May 2018 (Sheffield, UK)

Altai, Z., Viceconti, M., Li, X., Offiah, A.C. (2018) Investigating a possible mechanism of humeral fracture in non-ambulant children. Poster presented at the 8th World Congress of Biomechanics in July 2018 (Dublin, Ireland)

ACKNOWLEDGEMENTS

There are many people I would like to thank, for their kind support to produce this thesis.

First of all, I would like to thank both of my supervisors, Dr Xinshan Li and Professor Marco Viceconti, for all the help and guidance during the last four years, and for giving me the opportunity to work in such an interesting field of research. I knew “nothing” about biomechanics when I started my PhD, but your passion and enthusiasm to this field inspired and influenced me during my learning journey to go in deep and explore it. In every meeting with each of you I have learned new things. I am very much grateful that you always gave me the guidance necessary when I need it.

Also, I would like to thank Dr Muhammad Qasim for sharing his knowledge in finite element modelling and biomechanics. I will never forget all the help and advice I received during the first two years of my PhD.

I would like to extend my thank to Dr Amaka C. Offiah, for all the valuable advice in the paediatric field. It was a pleasure to work with you.

My special thanks to Dr Andre Castro for all the assistance and advice as a co-author, and as a friend.

I want to thank all the colleagues I had during these four years, the guys of the research group in Insigneo and Multisim. It has been a pleasure to be a member of the group since the beginning, and to have seen it grown and evolve over these years.

Also, I want to thank my sponsor, The Higher Committee for Education Development in Iraq (HCED) for supporting me financially and giving me the opportunity to study abroad.

Special thanks to my family, Dad and Mam, without you I would never imagine myself completing the degree, I hope that one day I can give you back at least a little of what you have provided me during my entire life. My brothers and sisters; Haitham, Heba, Muhammed and Reem, thanks for being such a support in my life and for encouraging me to do the best every time.

Finally, thank you to the person who always has been the one I find peace with away from the complexities of life. With whom I can share my problems, my sadness, and my happiness. I know you always will be there for me. The bond we share is very special.

CONTENTS

LIST OF ACRONYMS AND ABBREVIATIONS

aBMD	Areal Bone Mineral Density
AP	Anterior-Posterior
AUC	Area Under the Curve
BC	Boundary Condition
BMC	Bone Mineral Content
BMD	Bone Mineral Density
CT	Computed Tomography
DOF	Degree of Freedom
DXA	X-Ray Absorptiometry
FE	Finite Element
FRAX	Fracture Risk Assessment Tool
HU	Hounsfield Unit
H	Horizontal
IOF	International Osteoporosis Foundation
ITF	Inter-Trochanteric Fractures
LC	Loading Direction
MFS	Minimum Femur Strength
ML	Medial-Lateral
MPC	Multi-Point Constraints
NF	Neck Fracture
PCG	Preconditioned Conjugate Gradient
PTF	Per-Trochanteric
QCT	Quantitative Computed Tomography
ROC	Receiver Operating Characteristic
ROI	Region of Interest
SCF	Sub-Capital Fracture
SIDS	Sudden Infant Death Syndrome
SUDI	Sudden Unexpected Death in Infancy

TCF	Trans-Cervical Fracture
TF	Trochanteric Fracture
V	Vertical
WHO	World Health Organization

LIST OF TABLES

LIST OF FIGURES

1 INTRODUCTION

Bone fracture (or failure of the bone) is a common injury that can occur throughout life. The causes and the risks of fracture are different at different age ranges, however. In general, bone failure occurs when the bone is abnormally weak (e.g. due to pathology) and/or is placed under excessive stress. In this thesis, two important categories of long bone fractures will be investigated: (1) infant femoral fracture and (2) osteoporotic fracture. During childhood, bone fractures commonly occur as a result of accidents. For very young children who have a limited mobility (e.g. infants), however, bone fractures are highly associated with child abuse. In the elderly, on the other hand, osteoporosis is usually the main reason behind the high percentage of bone fractures, with hip fracture being the most common bone injury. It is worth noting that bone fracture can be catastrophic at any age, and is frequently accompanied by limited mobility over the medium term. Some of these impacts with relevance to the two categories of long bone fractures studied in this thesis are detailed in the following section.

In the USA, there are estimated to be more than 3,000 child abuse cases per year (Herman-Giddens et al., 1999). In the UK, an estimated one in every 1000 children experienced inflicted injury in 2007 (Singleton, 2010). Clinically, it is believed that child abuse cases are under-diagnosed (Barber and Sibert, 2000) due to a combination of reliance on the caretaker to describe the cause of the injury and because the detection of child abuse is faced by numerous challenges. One specific challenge is that very little information is known about how paediatric bones fracture under various loads, or their injury tolerance. This makes the process of distinguishing between accidental and inflicted injury very challenging in some cases, where clinicians have to rely mainly on their experience. Knowing the characterization of paediatric bone behaviour at the structural level is essential to understand its response to various loads. This, combined with a database of various fractures that are associated with common abuse incidents, could help to develop a tool that would identify or help to identify the cause of the injury.

There is therefore a big need to investigate the behaviour of paediatric long bones under various external loadings, such as bending and torsional loads. Such information will critically

enhance our knowledge of the injury tolerance of children's long bones. This information can then be used during diagnosis in the future by comparing fracture tolerance with the force predicted to have resulted (derived from a dynamic model for example) from the physical events described by the parents/carer.

Osteoporotic hip fracture, on the other hand, is often associated with a dramatic rise in patient morbidity and mortality. That is mainly because of the surgical operation and the recovery phase needed to treat a patient. According to the International Osteoporosis Foundation (IOF), among people who survive surgical interventions for an osteoporotic hip fracture, only one-third are restored to their former physical status. A recent study showed that, in the UK, hip fractures cost the NHS approximately £1.1 billion per year (Leal et al., 2015). The lifetime risk of osteoporotic fracture is relatively high, at 40–50% for women and 13–22% for men (Johnell and Kanis, 2005). This also shows that women are at much higher risk of hip fracture than men. The risk of fracture increases with age, with a reported high risk starting at around 50 years of age (Melton et al., 1992). This is of particular concern when taking into account the progressive increase of population median age (by 0.3 each year within the European Union, or EU) in the past decade (European Communities, 2018). This data means that the identification of patients under a high risk of fracture is important in order to provide them with the treatment necessary to prevent osteoporotic fractures and reduce subsequent treatment costs.

Currently, osteoporosis is clinically diagnosed by measuring bone mineral density (BMD) using dual energy X-ray absorptiometry (DXA). The measured BMD value is then compared with the average value for healthy young females. According to the World Health Organization (WHO), osteoporosis is defined when the value of BMD is equal or beyond 2.5 standard deviations (SD). After an osteoporosis case is diagnosed, the risk of fracture is estimated according to the measured BMD and other epidemiological parameters using a sophisticated risk assessment instrument (e.g. FRAX[1]). Although this method is commonly used, it has been reported that BMD provides only a moderate fracture risk prediction. BMD alone is able to predict fracture at a rate of 30-50% with a false positive rate of 15% (McCreadie and

[1]. https://patient.info/doctor/frax-fracture-risk-assessment-tool

Goldstein, 2000). This shows that there is a need to develop a more accurate tool to predict the risk of fracture in elderly patients (Geusens et al., 2010).

In the last few decades, computed tomography based finite element models (CT/FE) have been widely used to investigate the biomechanical characteristics of adult human bones, but only rarely in children, mainly due to the difficulties of obtaining paediatric bone samples. In adult bone investigation, it has been reported that CT/FE models can predict bone strength with high accuracy (Pottecher et al., 2016), while in paediatric bone investigations, a recent study showed that a CT/FE model of children's bones has the potential to predict paediatric bone strength using a similar approach as that used to model adult bones (Li et al., 2015). CT/FE models of paediatric bone may therefore be an alternative tool to provide valuable information on paediatric bone biomechanics.

The enormous literature on adult bones indicates that bone strength can be a better predictor of fracture risk than BMD. The hypothesis is that bone strength is a function of geometry, material properties and loading condition, while BMD only represents the mineral content. After several improvements in the FE models, it has been shown that they are capable of a more accurate prediction of bone strength than BMD (Cody et al., 1999). The ability of FE-predicted bone strength to classify facture and non-fracture patients requires further investigation, however. A number of studies have reported that, compared to DXA, CT/FE models provided a comparable classification accuracy of fracture status (Keyak et al., 2013, 2011; Kopperdahl et al., 2014; Nishiyama et al., 2014; Orwoll et al., 2009). Although the evidence is not yet strong enough for FE models to replace DXA in clinical practice (Van Den Munckhof and Zadpoor, 2014), the recent improvements in FE models continue to challenge the current clinical approach (Qasim et al., 2016; Viceconti et al., 2018).

1.1 Aims

The main objective of this thesis is therefore to develop subject-specific CT/FE modelling procedures further in order to predict bone strength or injury tolerance for two different age groups, young children and adults. Each of these two FE models has different purposes. The CT/FE model for paediatric long bones is developed to estimate the fracture tolerance of young children aged from new-born to three years old under various loading conditions, with an attention to provide quantitative data for the identification of inflicted injuries. The CT/FE

model of the adult proximal femur, meanwhile, is developed to more accurately classify fracture and non-fracture cases and predict various hip fracture types as observed in clinical practice.

The specific aims of this thesis are listed below:

1) To improve the preliminary CT/FE model developed in Li et al. (2015) and to develop a simulation of a new loading case (torsion) and conduct simulations on 30 cases of children aged from zero to three years old

2) To use the CT/FE procedure developed in aim 1 to investigate a case of paediatric fracture that was previously reported as a debated accidental injury scenario (humeral fracture of infants while rolling from prone to supine).

3) To improve the classification accuracy of the CT/FE model for adults under side fall configurations in term of fracture status using:

    A. Various boundary conditions (Linear, MPC and Contact Models).

    B. A wide range of loading conditions that cover all possible fall directions (various posterolateral and anterolateral falls).

4) To investigate the ability of the adult FE model to predict various hip fracture types as reported clinically, including per-trochanteric fracture, which had very few reports in previous FE studies.

1.2 Thesis organization

To reach the aims reported above, this thesis was divided into three main studies: Studies I, II, and III, spread across nine chapters including the introduction. Each of these studies are reported in a separate chapter (Chapters 5, 6 and 7, respectively). Below is a description of the content of each chapter in this thesis:

Chapter 2 describes the anatomy and development of the human long bone. The changes that a long bone experiences throughout various stages of life are also discussed.

Chapter 3 reviews the literature on the material and mechanical properties of both paediatric and adult bones. Fracture morphologies and the most common fracture types are described, with relevance to inflicted injuries in children as well as osteoporotic fractures in the elderly. A survey of various paediatric long bone and adult proximal femur FE models is presented.

Chapter 4 details the methodological approach of the modelling technique that was followed to develop all the CT/FE models in this thesis. The details of the cohort used for each study are also described in this chapter.

Chapter 5 presents Study I (***strength of paediatric bone under bending and torsional loads***). A description of the boundary and various loading (bending and torsion) conditions of the model is provided. The morphological parameters and the range of predicted femora strength are reported. The results of this study are also discussed in this chapter.

Chapter 6 presents Study II (***spontaneous humeral fractures in infants***). The boundary and loading conditions of the model are described. The predicted strains are reported and compared to the elastic limit of human bone in order to investigate the likelihood of a fracture occurring. A discussion of the results of this study is also provided at the end of the chapter.

Chapter 7 presents Study III (***strength of proximal femur under side fall loading conditions***). It starts with a description of the various boundary and loading conditions of the model (various side fall directions). The results of these models are presented in terms of bone strength prediction, classification accuracy and fracture type predictions. A discussion of the results is provided at the end of the chapter.

Chapter 8 discusses the limitations of Studies I, II, and III with recommendations for future work.

Chapter 9 is a summary of the work in this thesis and highlights its most important achievements.

2 ANATOMY AND PHYSIOLOGY OF LONG BONE

2.1 Introduction

Long bone is a term used for bones that have greater length than width. The best example of human long bone is the femur, which is the main bone of the thigh. It represents the longest and largest bone of the human skeleton (Tortora and Grabowski, 2003).

In general, at the organ level, any typical long bone consists of three parts: (a) the diaphysis, which is a nearly cylindrical part that represents the shaft of the long bone, (b) the epiphyses, representing the proximal and distal parts of the long bone, and (c) the metaphyses, represented by the regions that connect the diaphysis with the epiphyses; these are the regions responsible for the growth of the long bone longitudinally (as described in detail later in this chapter).

The long bone is not completely solid. At the tissue level, bone has small spaces and gaps that are irregular in both shape and size, and which serve to give the bone a matrix structure. Some spaces are channels that allow the blood vessels to pass through, whereas the bigger spaces are filled with bone marrow. Based on the size and distribution of these spaces, bone tissue can be categorized into two main types: compact (or cortical) bone, and spongy (or trabecular) bone.

Bone is subject to various development stages during the life of the foetus and after birth. It is therefore in a continuous process of modelling (generating new bone) and remodelling (replacing the old bone). One important characteristic of bone is its ability to withstand various load conditions, or load bearing. These loads are limited, however, by the bone's mechanical strength (Bueno and Glowacki, 2011). It is known, however, that bone can alter its strength in order to respond to changes in the external forces.

This chapter will describe the anatomy and physiology of long bones. In particular, the sections below will give a brief overview of bone formation during the life of the foetus, and its growth and remodelling from childhood to old age.

2.2 Structure of bone

Bone is a complex organism with both mechanical and metabolic roles. Its main mechanical role is to bear weight and protect organs. Its metabolic role is to maintain the internal stability of minerals inside the body.

Bone matrix consists of 25% collagen fibres, 25% water, and 50% crystalized inorganic salts. These mineral salts are mainly calcium carbonate and calcium phosphate with additional magnesium hydroxide, fluoride and sulphate. The crystallization of the mineral salts in combination with the collagen fibres give rise to the stiffness of the bone, while the flexibility of the bone is provided by the collagen fibres (Tortora and Grabowski, 2003). Bone could therefore be considered as a composite material consisting of collagen fibres. These fibres are laid down alternately to form the lamellae, which in turn form the basic structure of cortical and trabecular bone (see Figure 2.1).

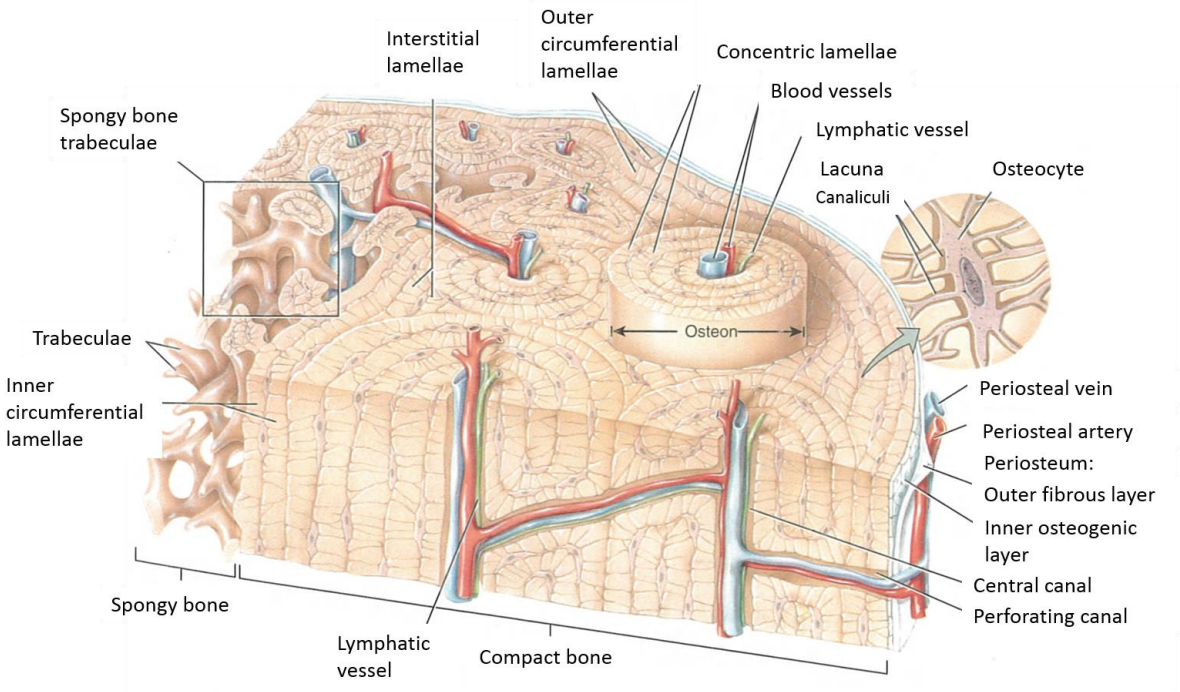

Figure 2.1 Section through the diaphysis of a long bone showing the spongy and compact bone structures (reproduced from Tortora and Grabowski, 2003).

2.2.1 Cortical bone

Cortical bone tissue usually forms the external layer of all bones. In long bones, it is allocated primarily in the diaphysis. Cortical bone accounts for 80% of the total body bone mass (Tortora and Grabowski, 2003), due to its dense structure, with only 5%-10% of porosity (Anderson, 1994). The cortical bone provides support and protection and is the primary structure to withstand body weight and external forces.

Cortical bone is arranged by units known as osteons, as shown in Figure 2.1. These units (osteons) align along the line of action of stresses. For example, in the long bone, they align parallel to the longitudinal direction of the bone. Thus, long bones are able to withstand considerable bending forces applied on both ends of the bone. However, the lines of the stress change with the change of the physical activities, such as from crawling to walking. They can also change as result of fracture or physical defect. The arrangement of the osteons therefore changes over time according to the external cues (Tortora and Grabowski, 2003). In general, cortical bone thickness has been found to increase continuously with age until adulthood (Smith and Walker 1964). In contrast, a decrease in the cortical thickness is usually observed with subsequent aging, especially in women after the menopause.

2.2.2 Trabecular bone

Trabecular bone is mostly located at the ends of the long bones, represented by the metaphysis and the epiphysis, and in the cuboid bones (one of the tarsal bones located at the lateral side of the feet). It forms approximately 20% of the adult human skeleton (Tortora and Grabowski, 2003). Trabecular bone has a high porosity of about 50%-90% (Anderson, 1994), which means it has a large surface area and light weight relative to its volume.

In contrast to cortical bone, trabecular bone does not contain osteons, but is made up of an irregular lattice of thin columns and rods known as trabecula (Figure 2.1). This gives trabecular bone the ability to withstand forces in different directions, as oppose to a preferential direction in the cortical bone. The degree of porosity of trabecular bone is not fixed; and it is directly affected by external loadings, bone diseases and aging. The trabecula starts to noticeably weaken and thin with aging (Boskey and Coleman, 2010), which is a normal process affecting both women and men at different rates (Jee, 2001). Such changes in bone structures and properties at different stages of life will be described in the next few sections.

2.3 Development and ageing of bone

2.3.1 Foetal stage

The actual process of bone formation, which is known as ossification, starts at six or seven weeks of the embryonic development stage (Tortora and Grabowski, 2003). Bone formation consist of two different pathways; intramembranous ossification and endochondral ossification. Both processes form the same structure of bone but through different methods.

Intramembranous ossification is relatively straightforward (out of the two) and consists of four main stages, through which the rudimentary bone tissues are developed. The first stage is the formation of the centre of the ossification through clustering of the mesenchymal cells. In the next stage, the osteoblasts are secreted, and osteocytes are formed. The third stage is marked by the development of the trabecular matrix, while the last stage is the development of a thin layer of cortical bone superficial to the trabecular bone.

The second process, which is known as the endochondral ossification, mainly concerns the formation of long bones (Scheuer et al., 2000), and is marked by the presence of cartilage (Tortora and Grabowski, 2003). This process consists of five stages, by the end of which the regions of the diaphysis and the epiphyses are formed (see Figure 2.2). The first step starts by the formation of the cartilage model. This happens with the gathering of mesenchymal cells at the location of bone formation. The cells then develop to chondroblasts, which in turn form the cartilage model. The next stage mainly involves an increase in the length and thickness of the cartilage model. The third stage marks a critical step where the cartilage is replaced with a primary ossification centre. The primary ossification centre grows to form the diaphysis of the long bone. Afterwards, a secondary ossification centre develops at both ends to from the epiphyses; this process usually occurs at the time of birth. The last stage involves the formation of the articular cartilage and epiphyseal plate. The former forms the outer surface of the epiphyses, while the later connects the epiphyses and the diaphysis. Epiphysial plates are responsible for the lengthening of the long bone after birth.

During the life of the foetus, external force is an important contributing factor to ensure the development of a healthy bone during various stages of formation. One major force involved at this stage is the amount of muscle contraction, which has been reported to affect the size and shape of the bone (Rodríguez et al., 1988).

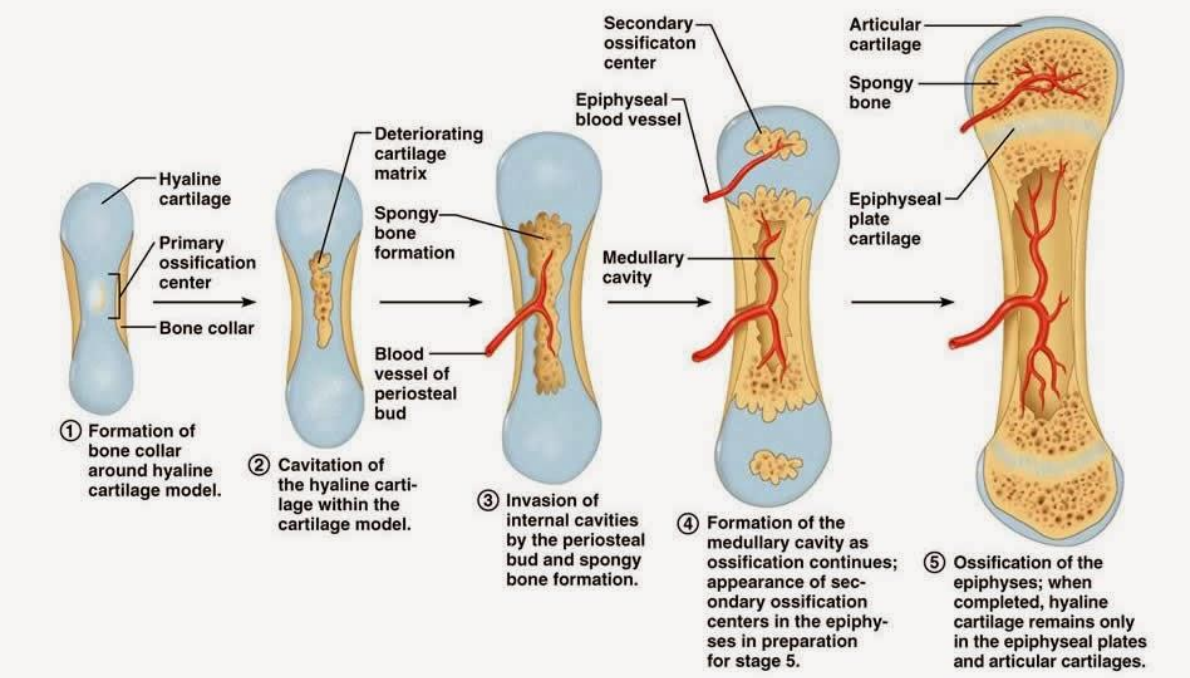

Figure 2.2 Five stages of endochondral ossification (Marieb et al., 2016); the replacement of cartilage by bone

2.3.2 Childhood stage

After birth, in addition to the increase in the length and size of the long bones, the bones change in shape and composition (Scheuer et al., 2000). As mentioned in the previous section, the diaphysis and either one or both proximal and distal ossification centres typically form during pregnancy and are present at birth. This varies among individuals and the type of long bone, however. For example, the proximal ossification centre of the humerus is usually present at birth (Menees and Holly, 1932), while the distal ossification centre may not appear until after birth, usually between six months and two years old. In contrast to the humerus, the distal ossification centre of the femur is usually present at birth while the proximal ossification may not appear until six months later (Scheuer et al., 2000). Other contributing factors include the weight and size of the baby at birth (Kuhns and Finnstorm, 1976).

On average, at birth 79% of the total length of the long bone is mineralized (mainly in the shaft region), while 21% is still in cartilaginous form (located at either end of the long bone) (Gray and Gardner, 1969). From childhood to adolescence, the ossification centres and the cartilaginous regions are in a continual state of growth to form the mineralized proximal and distal ends of the long bone. These changes, and the age at which they occur, are described

in an illustrative diagram of the developing femur shown in Figure 2.3. In summary, the proximal (mainly the proximal head) and the distal epiphysis are formed from the proximal and distal ossification centres, respectively. These are the primary ossification centres. Other secondary ossification centres appear at different ages, which will develop into the greater and lesser trochanter. In parallel to the development of the regions of ossification, the proximal and distal epiphyses fuse to create the neck and the condyles, respectively, of the femur.

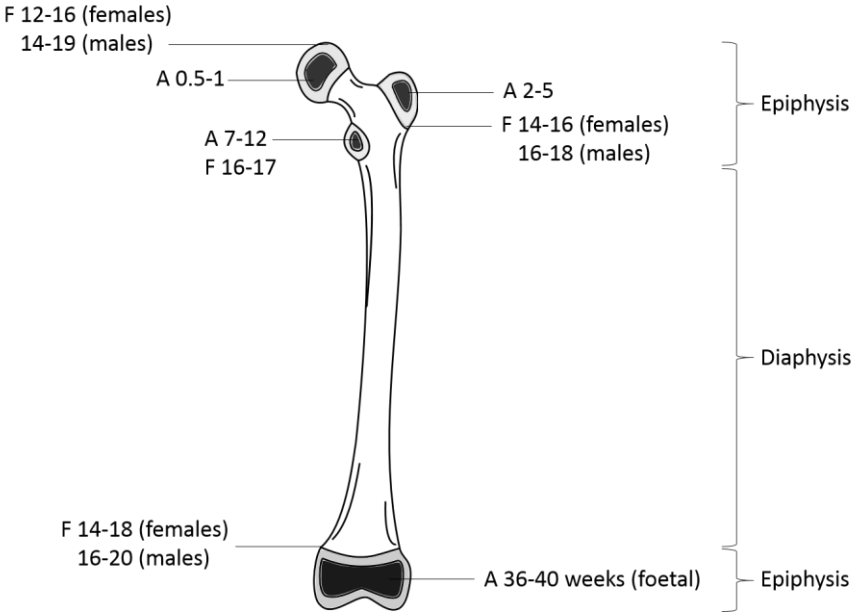

Figure 2.3 Ossification centres and cartilaginous regions of the femur during different stages of life, as reported in (Scheuer et al., 2000). A; appearance, F; fusion of the ossification centres. All numbers are in years. Black areas represent the ossification centres, grey areas are the cartilaginous regions, and white areas are the ossified/mineralized bone.

The growth plates are located between the proximal and distal epiphyses and the diaphysis, and are responsible for facilitating bone growth (elongation). The distal part is largest and fastest in growth compared with the proximal part. It has been reported that the distal epiphysis is responsible for about 70% of the total lengthening of the bone (Ogden, 1984), which mostly occurs between 16 and 19 years of age in males, and 14 and 18 years of age in females (Hansman, 1962).

During growth, long bones not only increase in length, but also in width and cross-sectional area. Figure 2.4 illustrates the shape changes at different cross-sections of the femur during growth. The cross-section of the mid-shaft of the diaphysis develops from a sub-circular shape

in childhood to a more elongated shape in the anterior-posterior direction at adulthood (Cowgill et al., 2010; Gosman et al., 2013; Ryan and Krovitz, 2006). These changes in shape are combined with an increase in size (diameters of the cross-section). The most accelerated changes are found during early childhood and adolescent, and are related to the changes in the type and magnitude of loads applied to the limb. This increase in loads is largely due to the changes in mobility (e.g. from crawling to walking) during the early stages of life. During adolescence, hormonal changes, along with the increase in body mass, are the main reasons behind the changes in the size and shape of the bone (Gosman et al., 2013).

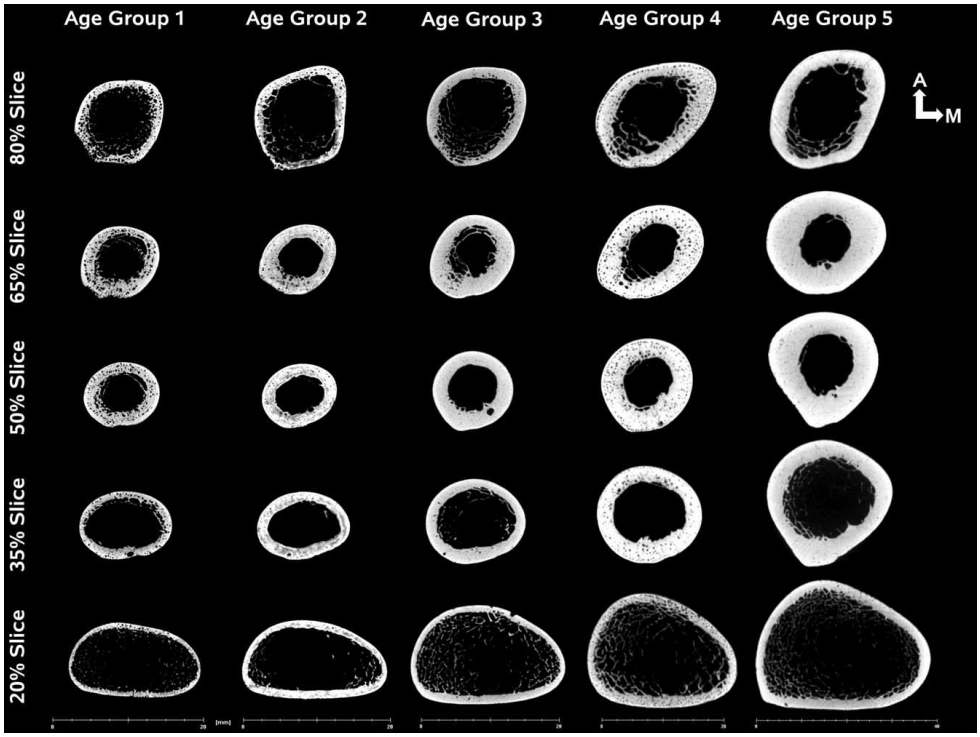

Figure 2.4 Cross-sectional shape changes at different locations of the diaphysis of the femur for five different age (years) groups (reproduced from Gosman et al., 2013). The five groups are: Group 1 (0-1.9), Group 2 (2-4.9), Group 3 (5-8.9), Group 4 (9-13.9), and Group 5 (14-17.9). A is the anterior, and M the medial side of the femur.

2.3.3 Adulthood stage

A fully developed femur consists of three parts: the diaphysis, proximal and distal epiphyses (see Figure 2.5). The proximal epiphysis consists of the femoral head, and the neck that connects the femoral head to the greater and lesser trochanters. The region between the greater trochanter and the neck is called the intertrochanteric region. The diaphysis is represented by the shaft of the femur, and has a tear-drop shaped cross-section (Cowgill et

al., 2010). The distal epiphysis contains the medial and lateral condyles, which are articulated with the condyles of the tibia. In between the two condyles, there is a depressed area called the intercondylar fossa. The femoral head is located at a concave region of the pelvis called the acetabulum.

Even after skeletal maturation, the bone continues to renew itself in a process called remodelling. Remodelling involves the replacement of existing bone with new bone. This is carried out by osteoclasts resorbing the bone and osteoblasts laying down new bone. An estimated 5% of the compact bone and 25% of the trabecular bone are replaced over the course of a lifetime (Martin et al., 2015). This process helps to alter the architecture of the bone to meet the changes in mechanical needs as well as to repair microdamage in the bone matrix (Hadjidakis and Androulakis, 2006). With aging, however, the absorption of bone exceeds the rate of formation, leading to a decrease in bone mass. This bone loss is also known as osteoporosis, which is discussed in the next section.

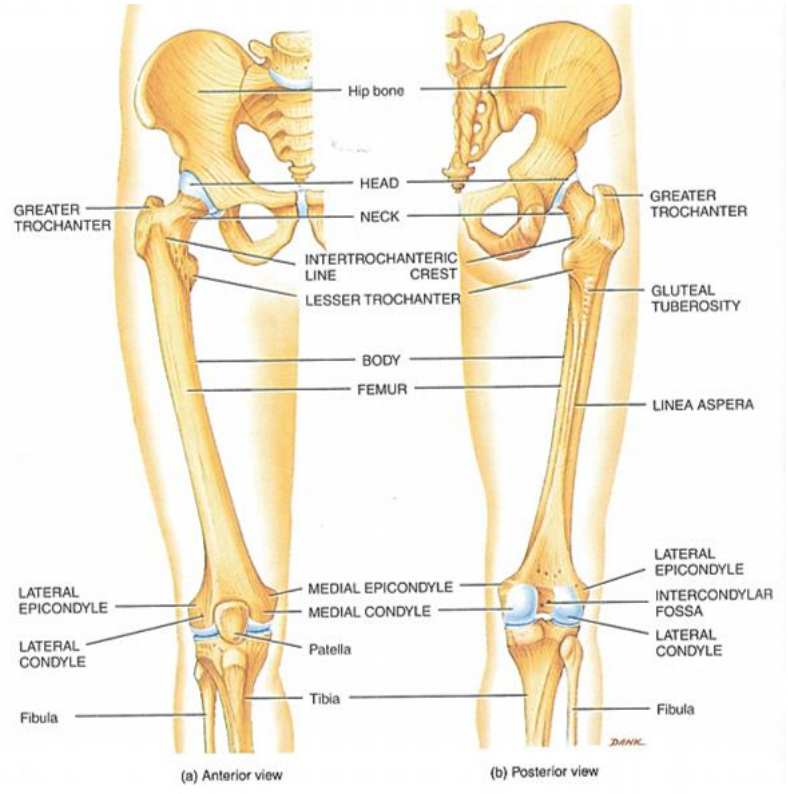

Figure 2.5 Anterior (left) and posterior (right) views of a fully developed femur (Tortora and Grabowski, 2003)

2.3.4 Elderly stage

With aging, bone becomes more fragile and less effective in load bearing. This is primarily due to an imbalance in resorption and formation. Both cortical and trabecular bone become thinner and the local mineral content (bone mineral density, BMD) decreases. The bone as a whole therefore becomes weaker and is known as an osteoporotic bone (see Figure 2.6). This change affects more women than men, especially after the menopause. In women, bone loss starts in their thirties and accelerates after the age of 45, while the same process begins after the age of 60 in men. It has been reported that the average bone loss is about 8% in women and 3% in men for every ten years (Tortora and Grabowski, 2003). Moreover, with aging, bone tends to become more brittle due to the slower synthesis of collagen fibres. All of these factors make the ageing bone more susceptible to fracture, and accordingly the incidence of osteoporotic fractures are reported to increase exponentially with age in both men and women (Nieves et al., 2010).

The World Health Organization (WHO) defines the level of osteoporosis in terms of BMD and previous fracture histories, using what is known as the T-score. This is a measurement of how much the bone density is higher or lower than that of a healthy 30 years old adult (Figure 2.7). An individual with a score higher than -1.0 is normal, whereas a score ranging between -1.0 and -2.5 is diagnosed as osteopenia. A T-score of less than -2.5, on the other hand, is diagnosed as osteoporosis, and the patient is treated. Approximately half of the patients who have a bone mineral density that is higher than the accepted intervention threshold (T-score > -2.5) will experience a hip fracture (World Health Organization, 1994).

Hip fracture is one of the most devastating consequences associated with osteoporosis. It has been estimated that the lifetime risk of any osteoporotic fracture is within the range of 40–50% for women and 13–22% for men (Johnell and Kanis, 2005). A recent study showed that the total yearly hospital costs associated with hip fracture are approximately £1.1 billion in the UK (Leal et al., 2015). Hip fractures are therefore one of the major public health problems that could lead to permanent disability among the elderly (Moyad, 2003).

(A) Normal bone (b) Osteoporotic bone

Figure 2.6 Trabecular bone tissue of: (A) a healthy young adult; and (B) an adult with osteoporosis (Tortora and Grabowski, 2003).

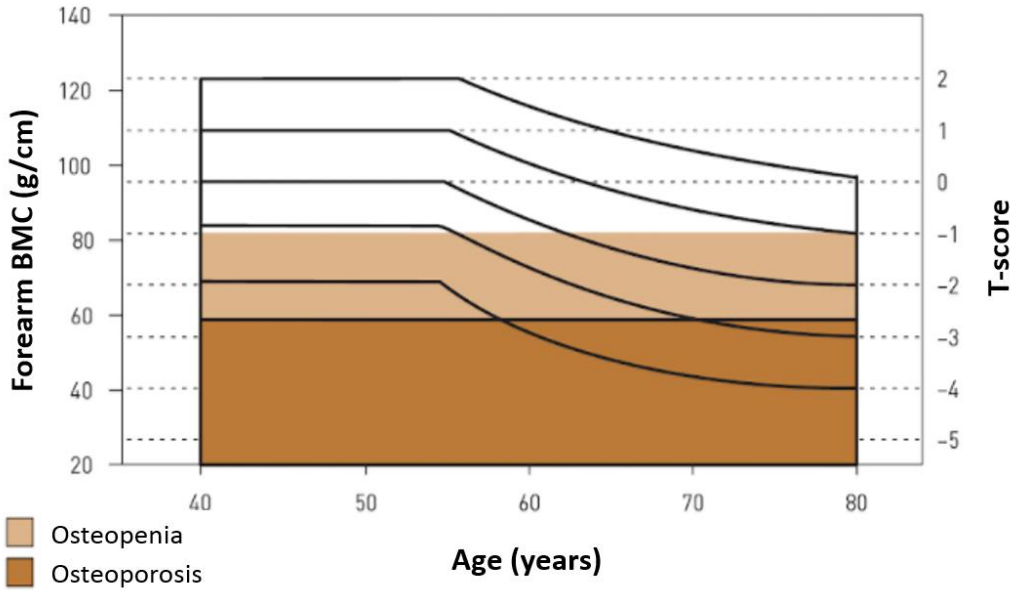

Figure 2.7 The definition of osteoporosis by the World Health Organization (WHO). BMC is the bone mineral content (World Health Organization, 1994).

3 LITERATURE REVIEW

The serious consequences of bone fractures mean that it is important to enhance our understanding of the fracture mechanisms and to develop effective techniques to better predict and prevent these incidents. This chapter provides a detailed review of the literature on previous studies of long bone for both young children and adults; with specific highlights on mechanical properties, the risk of fracture and the types of fractures of the bone.

3.1 Mechanical properties of long bone

The mechanical characteristics of bone are a description of the response of the bone to stress. Generally, this is described in terms of the amount of deformation occurring under an applied load, the mechanism and rate at which damage accumulates in the bone, and the maximum loads that the bone can tolerate before failure. The behaviour of the bone is usually governed by two variables: material (mechanical properties) and structural (geometry).

One of the most important properties of bone is its density, which is related to its material properties. Three types of bone density are usually measured in order to describe the mechanical properties of the bone. These are real density, apparent density and ash density. Real density is the wet weight divided by the real volume (which is the actual volume of bone tissue). Apparent density is the wet weight divided by the total volume of the sample (bone plus the pore spaces). Ash density, meanwhile, is the ash weight divided by the real volume.

Bone is considered to be a brittle material (Wendlova, 2008). This means that the relationship between the deformation of the bone and the applied load is characterized by the elastic constants, which can be determined from the mechanical testing of a bone sample (e.g. under tension or compression). Figure 3.1 represents a typical load-deformation curve for bone. The elastic deformation region is represented by the linear part of the curve. The slope of that region represents the stiffness. The plastic deformation, meanwhile, occurs after the yield point (point a in Figure 3.1); this is when the bone starts to behave nonlinearly until fracture. Fracture occurs when the bone exceeds its ultimate load (point b in Figure 3.1). The area under the curve represents the work needed to cause the failure (Jee, 2001).

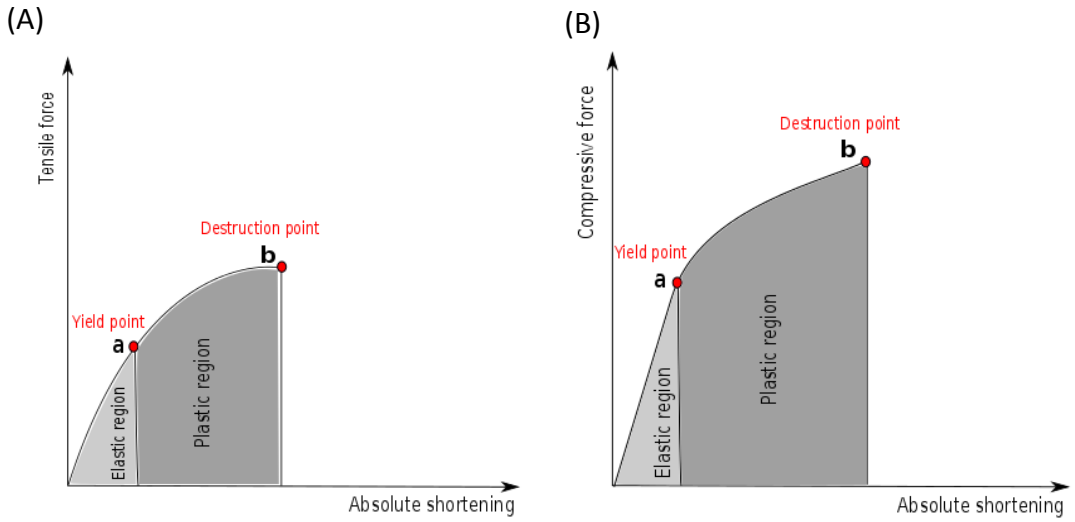

Figure 3.1 Load-displacement curve of (A) tension and (B) compression tests of bone.

The following sections discuss in detail the mechanical properties of the bone at the two different age groups investigated in this thesis: paediatric and adult.

3.1.1 Mechanical properties of paediatric bone

The mechanical properties of paediatric bone have been found to be different from adult bone, and this is noticeable in the mode of fracture of the bone. In contrast to adult bone, paediatric bone behaves like a green stick, tending to absorb more energy before fracture, with a considerable plastic deformation (Currey, 1979; Spencer, 1974). This is primarily due to the difference in mineral content (Scheuer et al., 2000), which has been found to increase with age (Ott, 1990). This leads to a reduction in the energy absorption by about a factor of three from the age of three until the age of ninety (Currey, 1979). Bone with a high mineralization (e.g. adult bone compared to children's) is stiffer and stronger (with a higher modulus of elasticity) with less toughness or ability to absorb energy (with less plastic deformation).

Only a few studies have investigated the mechanical properties of paediatric bone tissues, the majority of which were conducted decades ago. The lack of recent studies in this area is mainly due to the difficulties in obtaining paediatric bone samples (Currey et al., 1996; Currey and Butler, 1975; Mueller et al., 1966; Öhman et al., 2011).

In 1966, Mueller and his colleagues investigated changes in density and mineral composition of bone with age (Mueller et al., 1966). They used specimens of trabecular bone taken from

vertebral bodies, with an age range from new-born to 85 years old. They reported that the water content decreases with increasing age, whereas the ash density increases. Interestingly, the organic fraction remains constant with age. The increased ash density through life was also later confirmed by Currey and Butler (1975). They studied cortical bone samples taken from femora with an age range of two to 84 years old, finding that paediatric samples had a lower modulus of elasticity, bending strength and ash density than adult bone samples. On the other hand, the paediatric bones both deflected and absorbed more energy before failure. In addition, the study found a fair correlation between ash density and both the bending elastic modulus and strength (R^2=0.40 and R^2=0.61, respectively). In 1996, the same authors continued to investigate the correlation between the mechanical properties of bone and both ash density and age (Currey et al., 1996). This later study was conducted on cortical bone samples of femora between the age of four and 82 years old. The study concluded that around 60% of the variance in the mechanical properties (work of fracture and impact energy) could be explained by the age and ash density. Consequently, weak correlations were reported for ash content with work of fracture (R^2=0.53) and impact energy (R^2=0.52). This study was the first to provide initial evidence that the material properties are somehow correlated with the ash density for both paediatric and adult bones.

In 2011, Öhman et al. investigated children's bone tissues with a hypothesis that they can be considered in the same way as adult bone tissue, albeit with a reduced density and material properties. The authors conducted a compressive test on cortical bone samples taken from the tibiae and femora of donors aged between four and 61 years old. The paediatric samples were taken from patients undergoing surgical removal of primary bone tumour. These samples were cut from a distance of at least 10 mm from the lesion. The adult bone samples were taken from healthy donors. The study found a strong correlation between the ash density and the compressive Young's modulus and strength (R^2 ranged between 0.86–0.91), in contrast to the weak correlation reported in previous studies. Öhman et al. (2011) related the improvement in their correlation to two factors: (a) the higher sample size used; only three out of nine subjects were under 20 years old in Currey et al. (1996), compared to 12 out of 24 subjects in Öhman et al. (2011); and (b) the uses of different loading conditions that took into account the orientations of the fibre, which was neglected in Currey's study. The orientation of fibre has been reported to be an important factor while studying the material

properties of the bone during mechanical test (Martin and Ishida, 1989). Öhman et al. (2011) therefore applied different loading conditions in the experimental setups on the tissue (bending and impact tests compared to bending only in Currey's study), they showed that the good correlations reported in adult human bone can be extended to describe children's bone tissues.

These studies indicate that paediatric bone tissue has lower compressive stiffness and strength compared to adult bone. In addition, paediatric bone undergoes larger deformation and absorbs more energy before fracture, thus exhibiting typical green stick fracture behaviour. Although limited, existing evidence therefore shows that the mechanical properties of child bone tissues are indeed correlated with ash density.

3.1.2 Mechanical properties of adult bone

In contrast to paediatric bone tissue, the mechanical properties of adult bone have been widely investigated by many researchers.

Bone is often considered as a composite material. The trabecular bone is anisotropic and nonhomogeneous, while the cortical bone is linear elastic, isotropic in the transverse direction, and relativity homogeneous. Mechanical testing showed that the fracture load of bone in compression is higher than in tension, and that the material properties are generally higher in cortical bone than in trabecular bone (e.g. elastic modulus and yield stress) (Bayraktar et al., 2004; Kaneko et al., 2003; Turner et al., 1999; Zysset et al., 1999). Table 3.1 shows different mechanical properties of cortical and trabecular bones measured experimentally using specimens of femora (note that the femur is the most typical long bone used to investigate the properties of human bone). The cortical bone is stiffer than trabecular bone, but it can sustain less strain and more stress before failing. *In vivo*, trabecular bone is able to sustain 75% strain before failure, while cortical bone fails when the strain exceeds 2%. This is largely due to trabecular bone having a greater porosity than cortical bone, so that it can store more energy (Pal, 2014).

External loads also affect the structure of the bone and vice versa. Bone is subjected to daily loads, and it adapts its mechanical strength accordingly. For example, in the proximal part of the femur, the shape of the cross-section of the femoral neck is more rounded at the femoral

head where high compressive stresses are located, whereas it is more elliptical at the neck-shaft connection where high bending stresses are located (Zebaze et al., 2005).

Table 3.1 Mechanical properties of cortical and trabecular bone (mean ± SD) as measured experimentally in the literature

Reference	Specimen site	Specimen	E (GPa)	σ_{yt} (MPa)	σ_{yc} (MPa)
(Bayraktar et al., 2004)	Diaphysis	Cortical	19.9±1.8 (n=74)	107.9±12.3 (n=6)	N/A
	Neck	Trabecular	18.0±2.8 (n=12)	84.9±11.2 (n=6)	135.3±34.3(n=6)
(Kaneko et al., 2003)	-	Cortical	-	-	-
	Diaphysis	Trabecular	22.7±1.7 (n=16)	83.9±8.8 (n=7)	153.0±16.5 (n=7)
(Turner et al., 1999)	Diaphysis	Cortical	20.0±0.3 (n=60)	N/A	N/A
	Distal end	Trabecular	18.1±1.7 (n=30)	N/A	N/A
(Zysset et al., 1999)	Diaphysis	Cortical	19.1±5.4 (n=8)	N/A	N/A
	Neck	Trabecular	11.4±5.6 (n=8)	N/A	N/A

E young's modulus
σ_{yt} Yield stress in tension
σ_{yc} Yield stress in compression
n number of samples
N/A not applicable

Verhulp et al. (2008) showed that during a fall the highest strain occurs in the cortex of the femoral neck, with the highest compressive strains observed in the superior region and tensile strains observed in the superior region, as shown in Figure 3.2. This is reflected by having thinner cortical bone at the inferior aspect of the femoral neck than in the inferior region. With ageing, however, cortical bone in the superior region of the femoral neck becomes even thinner (Boyce & Bloebaum 1993; Mayhew et al. 2005).

Ageing is the single dominant factor leading to changes in the material and mechanical properties of the bone, as described in Section 2.3.4. It has been reported that the strength, modulus of elasticity and density of bone in younger adults is substantially higher than in older ones (Evans, 1976). Verhulp et al. (2008) reported that when applying loads to osteoporotic bone, a 61% less force was required to reach similar strains compared with healthy bones. Lotz et al. (1995), meanwhile, reported that for osteoporotic femurs, a similar stress distribution to a healthy femur can only be found with a significant change in the magnitude of the stress.

(A) (B)

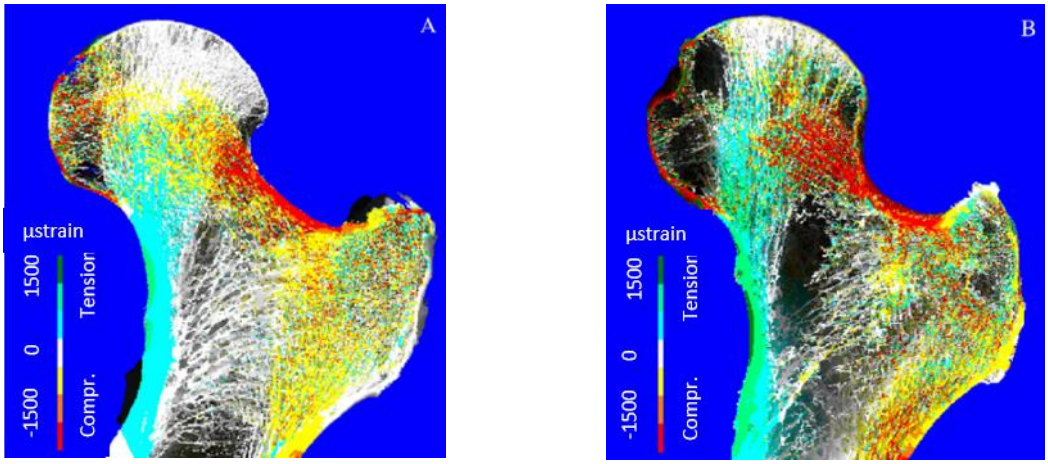

Figure 3.2 Distribution of the principal strains (e1 and e3) in (A) healthy, and (B) osteoporotic adult proximal femur. Reproduced from Verhulp et al. (2008).

3.2 Risk of fracture

3.2.1 Risk in children

The incidence of bone fractures in children increases with age (Rennie et al., 2007), peaking in the toddler age group. Falling is the major cause of injury (Loder et al., 2006; Thomas et al., 1991). It has been estimated that bone fractures account for 25% of all paediatric injuries (Cooper et al. 2004). In infants and toddlers, fractures can occur because of accidental or non-accidental (abusive) trauma. In infants, between 25% and 50% of all bone fractures are caused by inflicted injuries (Pierce et al., 2004). Fractures of the long bones are seen as the most common orthopaedic incidents in infants and very young children.

Among all bone fractures, fractures of the extremities account for 31-76% of all inflicted fractures (Caffey, 1946; King et al., 1988; Loder et al., 2006; Worlock et al., 1986). Femoral shaft fractures alone accounts for 28-45% of all long bone fractures in children (King et al., 1988; Loder and Bookout, 1991). Some studies believe that humeral fractures are highly associated with child abuse at an incidence of 46-78% (Merten et al., 1983; Thomas et al., 1991; Worlock et al., 1986).

Child abuse is a major social issue with serious consequences for the affected children and their families (Jayakumar et al. 2010). Children younger than two years old cannot communicate effectively, which makes them particularly vulnerable to abusive behaviours

(Carty 1997; Loder et al. 2006). The consequence of misdiagnosed child abuse case can be devastating, sometimes leading to subsequent abuse and the death of a child. The long term effects of children living in an abusive environment include inhibited physical growth, and intellectual and emotional development (Jayakumar et al., 2010). On the other hand, a wrongful claim of child abuse made against innocent families may lead to the unjust separation of the child from his/her own family (Kowal-Vern et al., 1992; Pierce and Bertocci, 2008). The diagnosis of inflicted injury is not always straightforward and relies heavily on the clinical experience and judgement. Abusive injuries make up 49% of all injury admissions of children younger than one year old (Leventhal, 1999), yet despite improvements in the clinical identification of inflicted injuries, the identification of such injuries using current technology remains challenging.

3.2.2 Risk in Adult

Hip fractures are one of the most common injuries in elderly people, mostly associated with osteoporosis combined with minor trauma. According to the International Osteoporosis Foundation (IOF), among people who survive surgical interventions for an osteoporotic hip fracture, only one-third are restored to their former physical status Within the UK, around 75,000 people suffer from hip fracture and by 2050 this number is expected to double (Parker and Johansen, 2006).

In the elderly, the lifetime risk of osteoporotic hip fracture is potentially high. IOF suggests that one-third of people over 65 have a fall each year. One of the serious complications of a fall is hip fracture. It has been reported that 90% of hip fractures result from falls (Hayes et al., 1993), and women are at higher risk than men. The risk of hip fracture is reported to be within the range of 40–50% in women, compared to 13–22% for men (Johnell and Kanis, 2005). The majority of hip fractures in elderly patients are associated with low impact energy.

3.3 Classification of bone fractures

In children, fracture of the shaft (of the long bone) is commonly seen in inflicted injuries. In elderly patients, fracture of the proximal part of the femur (hip fracture) is the most common osteoporosis-linked fracture associated with falls. The next two sections will therefore focus on describing the classification of these particular fractures.

3.3.1 Classification of long bone fractures in children

Fractures in children's long bones can be classified in several ways according to the anatomical location of the fracture, the pattern of the fracture, and the complexity of the fracture. Usually, fractures of the shaft are classified according to the patterns of the fracture. The common types of long bone fractures are spiral, oblique, buckle and transverse fractures (see Figure 3.3). Sometimes, a more complex pattern can be present, however, such as a combination of some or all of these fractures. Among these fracture types, spiral fracture is the most common in young children (King et al., 1988; Rex and Kay, 2000), although the rest are also frequently presented in children (King et al., 1988; Loder et al., 2006; Worlock et al., 1986).

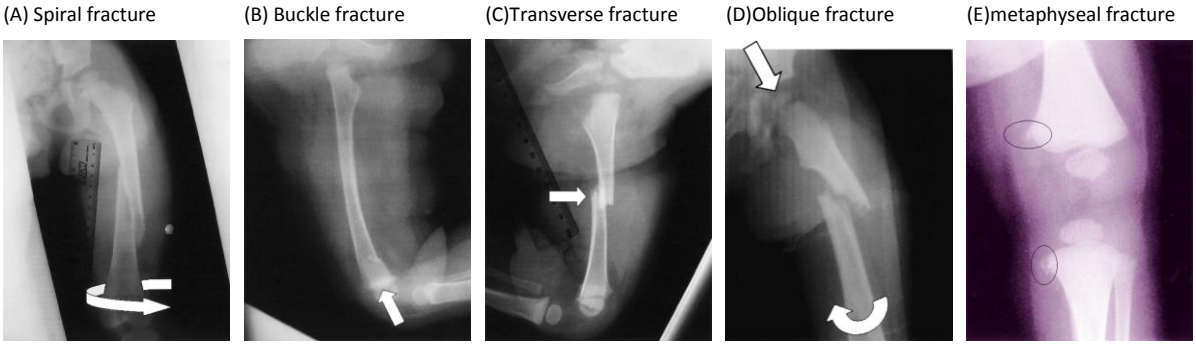

Figure 3.3 Various fracture patterns of long bone in children. Reproduced from Pierce et al. (2004).

The pattern of fracture is highly associated with the applied load. Spiral fracture is typically observed at the mid shaft. This type of fracture usually occurs under a torsional load applied along the longitudinal direction of the long bone, where one side of the bone is subjected to compressive stresses while the other side undergoes tensile stresses (Pierce and Bertocci, 2008; Turner and Burr, 1993). This has been confirmed experimentally using human cadaveric long bones (Kress et al., 1995). A study conducted by Pierce et al. (2000) on femurs of piglets, however, failed to generate consistent spiral fractures under torsion. The authors suggested that the reasons of this might be the absence of the periosteum during the experiment, or the difficulty in generating this type of fracture in a short bone such as that of a piglet femur. However, this brings some doubts to the suggested mechanism for spiral bones.

Buckle fractures occur under a compressive load transmitted axially to the long bone. This type of fracture normally occurs at the proximal or distal third of the bone, and close to or at the metaphyseal regions (Pierce et al., 2004). In transverse fracture, the fracture appears

normal to the longitudinal direction of the long bone. This type of fracture is usually caused by bending or tensile loads (Steven and Eric, 2009). These loads may act directly or indirectly on the bone. Oblique fracture is thought to be caused by a combination of different loads (Pierce et al., 2004), and the morphology of the fracture is determined by the dominant load type. Long oblique is believed to be caused by a pure torsion, and often has a similar appearance as spiral fracture in the X-ray. In contrast, short oblique fracture occurs when bending or compressive loads are dominant (Nahum and Melvin, 2002).

Failure of paediatric bone may differ from adult's bone depending on the ability of the bone to undergo plastic deformation before fracture. For brittle materials, such as the adult bone, bending load causes the crack to propagate in a straight-line casing a transverse fracture. In contrast, for a more ductile material such as the paediatric bone, the crack will propagate at 45^{o}, causing the bone to fail under shear, leading to an oblique or spiral fracture (Cheong et al., 2017). As mentioned in Section 3.1.1, paediatric bone is more ductile than adult bone (absorb more energy before fracture). Therefore, it is more common for paediatric bone to fail under shear stresses with either oblique or spiral fractures. However, the investigation of fracture pattern is not the main purpose of this thesis.

The most common fracture type believed to be associated with abusive injuries is spiral fracture (Pierce et al., 2004). That is due to the twisting mechanism. Some studies, however, have suggested that spiral fracture may not necessarily be a sign of abuse, and other types of fracture (such as transverse fracture) may be more indicative (King et al., 1988; Scherl et al., 2000; Thomas et al., 1991). Buckle fracture can also be caused by abuse injuries. For example, the child may be thrown on a solid surface or their extremity bent intentionally backwards (Pierce et al., 2004). Another type of long bone fracture that is highly associated with child abuse is metaphyseal fracture (Figure 3.3 E). This is a unique failure mode as it requires a specific loading mechanism that almost only occurs through abusive trauma (Kleinman et al., 2011), resulting in a combination of tensile, compressive and bending loads in the metaphyseal region (Tsai et al., 2017).

3.3.2 Classification of hip fractures

The hip joint is a ball and socket joint formed by the proximal femur and the socket of the acetabulum. Hip fractures are clinically divided into intracapsular and extracapsular fractures

according to the location of the fracture (Parker and Johansen, 2006) (see Figure 3.4). These fractures can be further subdivided according to the location, as illustrated in Figure 3.5. There are two main types: (a) neck fractures consisting of sub-capital and trans-cervical fractures, and (b) trochanteric fractures consisting of intertrochanteric and per-trochanteric fractures. It should be noted that more complex fractures are sometimes observed as a combination of the fractures described above.

Femoral neck fracture and trochanteric fracture have been found to account for more than 90% of all hip fractures with an equal percentage (Gallagher et al., 1980). It has been reported that in pre-menopausal women, however, femoral neck factures are more common than trochanteric fractures. A progressive increase in the occurrence of trochanteric fractures has been reported for those aged more than 60 years old (Baudoin et al., 1993).

The occurrence of hip fracture may differ due to varying bone composition at different regions. The proportion of trabecular bone in the trochanteric region is higher than that in the neck region (50% compared with 25%) (Riggs et al., 1982). Some studies have reported that women with trochanteric fracture have a significantly lower BMD than those with femoral neck fracture (Duboeuf et al., 1997; Greenspan et al., 1994; Nakamura et al., 1992; Vega et al., 1991). Overall, the risk of both fracture types has been reported to increase with age, regardless of the gender (Cauley et al., 2009).

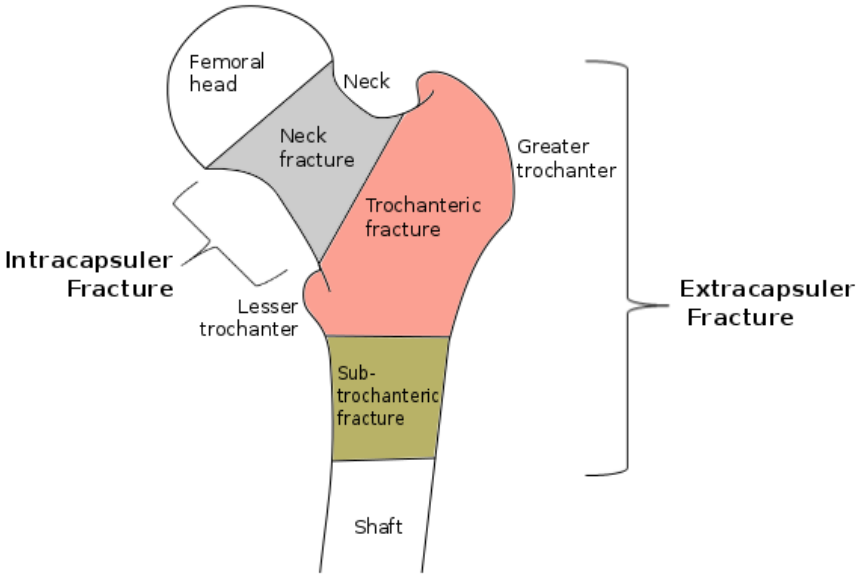

Figure 3.4 Clinical classification of hip fractures. Intracapsular fractures occur in the grey region whereas extracapsular fractures occur in the orange and green regions.

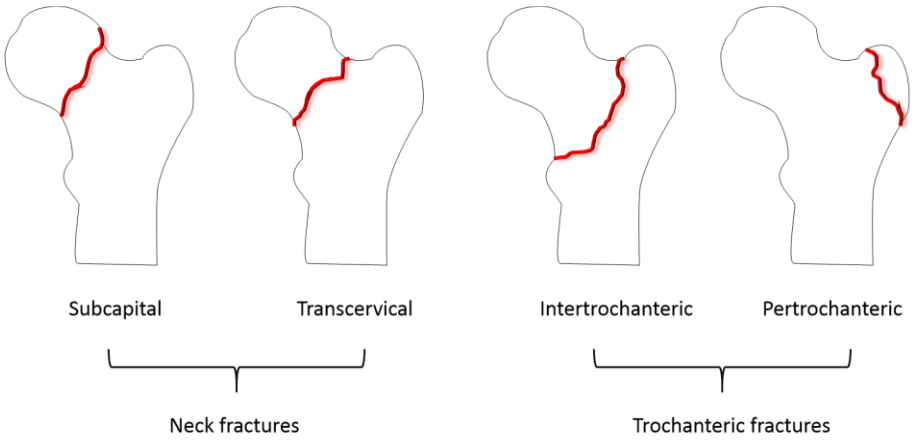

Figure 3.5 Typical femoral neck fractures and trochanteric fractures. These are subdivided into subcapital, transcervical, intertrochanteric, and per-trochanteric fractures

3.4 Estimation of fracture risk

Computed tomography based finite element analysis (CT/FE) has been shown to be one of the most effective non-invasive methods to estimate the strength of bone, which in turn helps to predict the risk of fracture. FE models have been extensively used in adult bone investigations but rarely for young children, meaning that, until now, there has been little information about the fracture tolerance of paediatric bones. There is accordingly a great need for a better and more quantitative understanding of young bones.

In elderly patients, the risk of hip fracture is clinically estimated by measuring the areal bone mineral density (aBMD) at the hip using Duel X-ray Absorptiometry (DXA). The absolute risk of fracture over a few years is assessed by adding other clinical factors, such as sex, age, weight, height, history of previous fractures, etc., to the aBMD information using the clinical standard known by FRAX. This is an online tool that predicts the probability of osteoporotic fracture occurrence in the ten years. FRAX was first released in 2008 by WHO, and is available online[2] (Kanis et al., 2017). FRAX has been reported to perform inconsistently compared to other simpler risk of fracture assessment tools, however (Rubin et al., 2013). Moreover, even following these risk assessments, half of those considered to have a low risk of fracture nonetheless sustain a fall in the future (Wainwright et al., 2005).

An improvement in the accuracy of the prediction of the risk of fracture can be provided by calculating the load that a patient's bone could sustain without fracturing (Viceconti et al., 2015). This also provides information on the stress and strain in the bone, which in turn gives an indication of the weak regions, or potential fracture locations. The distribution of the stress and strain in bones has been previously suggested to play a role in their mechanical response (Brand, 2010). Because bone has a complex geometry, previous studies have shown that personalized FE modelling is an effective method to study the mechanical behaviour of bones for both adults (Taddei et al., 2014) and children (Li et al., 2015).

[2]. www.shef.ac.uk/FRAX/

3.5 Finite element analysis

The FE method appeared in the late 1950s and early 1960s, and was first proposed in the orthopaedic literature in 1972 (as cited in Huiskes and Chao, 1983). Earlier than that, stress and strain state on bones has assumed to play an important role in many orthopaedics and biomechanics problems (Brand, 2010). But the classic mechanics approach was not able to provide satisfactory answers to many of the questions raised. This is mainly due to the complex structure of the bone, which cannot be accurately evaluated using the classic mechanics approach (suitable for a well defined regular shape). Since finite element approach has the ability to evaluate the stress and strain state in a structure with complex geometry, loads, and material properties, it was therefore recognized as a promising tool to answer these questions. In 1985, Basu et al. suggested that FE models can be used *in vivo* as they can show a reliable representation of the internal stress pattern. The first study aimed to investigate the mechanical behaviour of the bone using subject-specific finite element models was carried out in 1991 (Lotz et al., 1991a; Lotz et al., 1991b). The yield and fracture loads of two adult cadaver femurs were accurately predicted in comparison to the *in vitro* tests performed on the same two femurs. However, the predicted surface stresses were poorly correlated with the measured stresses *in vitro*. Since then, numerous studies have employed FE models to predict bone mechanics in adults (Angadi et al., 2015; Bessho et al., 2004; Dall'ara et al., 2012; Keyak et al., 1997; Koivumäki et al., 2012; Lotz and Hayes, 1990; Schileo et al., 2008b; Taddei et al., 2014), and very recently in children (Li et al., 2015; Meng et al., 2017; Tsai et al., 2017). With these continuous improvements in the modelling techniques, the later models were able to predict stress and strain a lot more accurately (R^2 = 0.91 (Schileo et al., 2007)) than their pioneers.

As mentioned in Section 3.1.2, in adult bone literature, cortical bone is often considered as isotropic material. It has been found that the prediction of the finite element models using anisotropic material is not that different when isotropic material is considered instead (Peng et al., 2006). Therefore, for simplicity, the majority of the above studies implemented isotropic material assignment to their models. However, the notion of anisotropy of paediatric bone, whether transverse isotropy or orthotropy, has rarely been investigated in the literature to the reason of the difficulties of getting paediatric bone samples. Lefèvre et

al. (2015) proposed some indication of bone isotropy related with age and they reported that both adult and children's bone show transverse isotropy.

It is clear that most of these studies were conducted on adult human bones, however, with only limited work performed on children. The following sections provide a detailed overview of the literature on the FE analysis of paediatric bone and adult hip fracture.

3.5.1 Finite element analysis of paediatric long bone

There are a few experimental studies that have reported on paediatric long bones (Forman et al., 2012; Miltner and Kallieris, 1989; Ouyang et al., 2003), focusing on studying some of the mechanical characteristics of long bones such as their stiffness and strength and changes with age under bending loads.

Miltner and Kallieris (1989) conducted experimental tests of three-point bending on 28 cadaveric lower limbs of children aged from one day to six years old. Although they reported a fracture moment ranging from 7.05 Nm to 109.5 Nm, their results do not show the fracture tolerance of the bone itself since they used the whole limb, including all bones and the surrounding soft tissues. Ouyang et al. (2003) did three-point bending tests on eleven pairs of isolated cadaveric long bones including femora, with an age range of two to twelve years old. Only three of these cases were between two and three years old (2, 2.5 and 3 years old), however, with fracture moments reported at 29.6, 24.3, and 39.6 Nm, respectively. In a more recent experimental study, Forman et al. (2012) conducted three-point bending on 23 cadaveric femora aged between one and 57 years. Again, only three cases were younger than three years old (1.33 and two cases of two years old), with fracture moments of 61.4, 61.7 and 65.5 Nm, respectively.

Because these three studies were destructive, unfortunately, limited information was extracted from the experiments. Moreover, none of these studies included very young children (younger than one year old). There is therefore a complete lack of information about bone mechanics for infants.

Li et al. (2015) proposed a potential step change in the use of FE approaches to study bones of very young children based on CT scans. The study was conducted on fifteen femora of children aged between zero and three years old. For the first time, they reported an estimated

fracture tolerance for paediatric bones under four-point bending loads. The study observed a steady increase in bone strength with age.

There are few other FE studies on paediatric bones, and only one on infants (Tsai et al., 2017), while the rest where on children at least six years old (Angadi et al., 2015; Meng et al., 2017; Yadav et al., 2017). Tsai et al. (2017) studied metaphyseal lesion, which is highly associated with child abuse, as mentioned in Section 3.3.1. They modelled the distal tibia and fibula of a three month old infant but adopted the material properties from a study conducted decades ago (Hirsch and Evans, 1965). Angadi et al. (2015) performed an experiment and developed FE model to study the paediatric femur under four-point bending and torsional loads, but used paediatric bone models made of simplified composite materials. Meng et al. (2017) investigated the pedestrian injury mechanism of children using an FE child model scaled down from an existing adult model. It should be noted that scaling models from adult bones is not representative of children's bones as they have a very different anatomy. Caution has been suggested when using scaled-down models as the estimation criteria are based on very different assumptions (Ivarsson et al., 2004). Yadav et al. (2017) studied the effect of the activation of muscle groups during gait on the growth of femur and thereby developed MRI-based FE models of femora of three children aged 6, 7 and 11 years.

In parallel, animal bone models have also been used to investigate the mechanics of immature bone fracture (Cheong et al., 2017). The authors showed that this is a valuable alternative given the scarcity of paediatric bone samples, and an effective way to confirm the modelling approach. In future, further studies are required in order to ascertain the relationship between immature animal bone and children's bone (Pearce et al., 2007).

It is obvious from the literature that there is a complete lack of personalized anatomical and material data for infants and very young children, who are at a rapid growth phase with marked changes during skeleton development. This makes it particularly challenging to characterize the mechanical responses of children's bones, as they depend on the developmental stages of each child.

3.5.2 Finite element analysis of adult femur under side fall configuration

FE analysis has been used to investigate adult bone mechanics for decades. Considerable efforts have been put into developing the methodologies in order to improve: (a) the

predictive accuracy of bone strength and (b) the classification accuracy for fracture and non-fracture cases (discrimination power). This section will discuss the evolution of the methodology and the current state-of-the-art in terms of predictive power.

3.5.2.1 Femur strength prediction

Several steps are required in order to develop a CT/FE model; these will be described in detail in Chapter four. One critical step is choosing the appropriate boundary conditions (BCs). These are prescribed in the model to mimic either a real-life scenario or experimental set-up. The set of applied BCs (model constraints and load) have been shown to directly and significantly affect the predictive accuracy of the model (Rossman et al., 2015).

There are an enormous number of FE studies on fall or side fall loading conditions (Dall'ara et al., 2012; Falcinelli et al., 2014; Ford et al., 1996; Keyak et al., 2001, 1997; Koivumäki et al., 2012). In these, BCs are usually applied to three regions of the proximal femur: the femoral head (where the load is applied), the greater trochanter (which must be constrained against the load direction), and the distal end of the femoral shaft (displacement constraint). The exact BC varied between different studies, each with its own advantages and drawbacks.

In the majority of the studies, the distal end of the proximal femur was fully constrained (Bessho et al., 2004; Dall'ara et al., 2012; Falcinelli et al., 2014; Ford et al., 1996; Keyak et al., 1997; Koivumäki et al., 2012; Lotz and Hayes, 1990; Orwoll et al., 2009; Pinilla et al., 1996; Qasim et al., 2016), even though it was free to rotate around the longitudinal axis of the shaft in a typical side fall experiment (Ariza et al., 2015; Dall'ara et al., 2012; de Bakker et al., 2009; Dragomir-Daescu et al., 2011; Grassi et al., 2012; Nishiyama et al., 2013; Pinilla et al., 1996; Zysset et al., 2013). This may be due to the limited degrees of freedom that it is possible to specify in the FE model. Most FE models used a tetrahedral mesh, with either four or ten nodes per element. This element type has three degrees of freedom per node (translations in x, y and z directions), with no explicit rotational degree of freedom.

Other studies allowed the femur to rotate in a direction transverse to the applied load by simulating a pivot point at the distal end of the femur (Ariza et al., 2015; Dragomir-Daescu et al., 2011; Grassi et al., 2012; Nishiyama et al., 2013). The greater trochanter were mostly fixed in the opposite direction of the applied load by directly constraining either one single node (the most lateral node) (Falcinelli et al., 2014; Qasim et al., 2016), or a group of nodes (nodes

at the location of the fixture in the experiment) (Dragomir-Daescu et al., 2011; Keyak et al., 2001). Some studies modelled a contact region between the surface of the greater trochanter and the surface of the fixture cup of the experiment (Ariza et al., 2015; Rossman et al., 2015).

One of the advantages of constraining a single node is that it minimizes the amount of displacement constraint in the model, while using a group of nodes reduces the resulting stress concentration in the trochanteric area. Using these constraints, however, will implicitly eliminate the rotation about the axis transverse to the load (Rossman et al., 2015). Rossman and his colleagues modelled various BCs that represent the side fall loading (most of these BCs were adapted from the literature as described above) and investigated their effects on the prediction of the femur stiffness. They reported that constraining the displacements directly on the model could cause overestimation of the stiffness value. On the other hand, modelling contact at the greater trochanter produced a more relaxed special constraint compared with applying direct constraints at nodes.

Studies have also investigated the orientations of the fall and their effects. Falling backwards is generally recognized as the weakest orientation compared to a fall directly to the side or to the front (Ford et al. 1996; Majumder et al. 2009; Pinilla et al. 1996). Based on these initial findings, the majority of FE and experimental studies have focused on investigating the strength of the femur under a posterolateral fall, assuming this to be the most vulnerable position. This BC usually sees the shaft of the femur being tilted at ten degrees from the horizontal plane, parallel to the longitudinal axis of the shaft, with the femoral head rotated fifteen degrees internally (van den Kroonenberg et al., 1992). Other studies have simulated multiple loading directions to estimate the minimum femur strength, with all of them considering only the lateral and posterolateral falls in different angles (Bessho et al., 2009; Falcinelli et al., 2014; Keyak et al., 2013, 2001; Pinilla et al., 1996; Qasim et al., 2016).

Table 3.2 shows the range of multiple loading directions that was used in these studies.

The influence of muscle forces on the prediction of the FE models in term of strain distributions (Duda et al., 1998), internal forces (Duda et al., 1997), and strength prediction and fracture location (Keyak et al., 2005) has also been previously examined. All these were done using physiological loading conditions, such as walking. Some studies found that the estimated bending moment was higher when muscle activity was not considered (Duda et al.,

1997), while the inclusion of the abductor muscle force had no effect on the predicted fracture location, and only up to 1.3% on the predicted femur strength. However, it should be noted that muscle forces are usually estimated from simplified musculoskeletal models, sometimes not individualised. Therefore, these results should be further examined with more accurate and individual-specific musculoskeletal models.

Taking into account the wide range of methodological approaches in the FE model, the current quantitative CT-FE models (QCT-FE) are able to predict bone strength with excellent accuracy when compared with experiments, indeed, slightly higher than that provided by DXA-aBMD (Cody et al., 1999; Pottecher et al., 2016). This suggests a good level of classification accuracy (fracture and non-fracture cases) using the strength predicted by the FE model.

Table 3.2 Multiple loading directions simulated in the side fall models in the literature. All angles are in degrees.

Reference	**Internal rotation angles**	**External rotation angles**	**Adduction angles**
de Bakker et al. (2009)	15	-	10
Bessho et al. (2009)	0, 15, 45	-	0, 30
Courtney et al. (1994)	15	-	10
Dall'ara et al. (2012)	0	-	30
Falcinelli et al. (2014)	0,15,30	-	0,10,15,30
Ford et al. (1996)	30, 45	-	0, 15
Hambli et al. (2013)	10	-	15
Keyak et al. (2001)	5, 15, 25, 35, 45	-	10,20, 30
Koivumäki et al. (2012)	0,15, 30	-	10
Lotz and Hayes (1990)	30	-	30
Nishiyama et al. (2013)	0,15, 30, 45	15, 30	10
Pinilla et al. (1996)	10	-	0,15, 30
Qasim et al. (2016)	0,15,30	-	0,15,30
Zani et al. (2015)	0, 15, 30	-	0, 10, 20, 30

3.5.2.2 Discrimination power of the CT/FE models

Although previous studies reported that CT/FE models show very good accuracy when predicting femur strength, the accuracy of these models to discriminate patients in terms of their risk of fracture is still a matter of debate. A number of previous studies have reported that no significant improvement was produced by CT/FE models compared to DXA-aBMD (Keyak et al., 2013, 2011; Kopperdahl et al., 2014; Nishiyama et al., 2014; Orwoll et al., 2009), while others reported a noticeable improvement (Falcinelli et al., 2014; Qasim et al., 2016). It

is worth noting that the former have some methodological limitations (e.g. mesh types and loading conditions), and therefore the predictive accuracy may not be optimal. These are discussed below.

Cartesian meshes with hexahedral elements were used in some of these FE models. Each element equals a unit voxel of the 3D QCT image. This kind of mesh is not as accurate in terms of stress and strain predictions as a smooth mesh generated from segmented CT images (Bardyn et al., 2010; Viceconti et al., 1998). This will in turn affect the performance of the mesh depending on the selected failure criteria (Zysset et al., 2015).

In addition, most of these studies simulated only one typical loading direction of side fall (Keyak et al., 2011; Kopperdahl et al., 2014; Orwoll et al., 2009), whereas Keyak et al. (2013) used three different loading directions and Nishiyama et al. (2014) used eight. It has previously been shown that comparing the classification accuracy of DXA-aBMD using the minimum strength predicted under a single loading direction is less accurate than that predicted under multiple loading directions (Falcinelli et al., 2014). A recent study conducted by Qasim et al. (2016) using a large cohort of pair-matched (for age, height and weight) subjects, simulated under multiple fall directions, showed that the discrimination accuracy of the CT/FE model was better than that of DXA-aBMD (79% compared with 75%).

With the currently reported accuracy of classification (between fracture and non-fracture cases) using the latest modelling approach, the CT/FE models cannot yet replace the current clinical technique, since the incremental increase in discrimination accuracy would fail to justify the economic cost of a full implementation in the clinical routine. One of the purposes of this thesis (Chapter 7), therefore, is to investigate if further improvements in BCs could help boost the classification and predictive power of CT/FE in order to make it a feasible tool in clinical practice.

4 MATERIALS AND METHODS

4.1 Materials

Two cohorts were used in this thesis. The cohorts were categorized (according to the age) into paediatric (zero to three years old) and adult (55 to 91 years old).

The right femora of the paediatric cohort were used in the first study (study I, Chapter five), which was conducted to provide information about the strength of paediatric femora under four-point bending and torsion. The second study (study II, Chapter six) was to explore spontaneous humeral fracture of infants while rolling; therefore, only the humeri of those who are within the age range of interest (four to seven months) were selected. The left humerus was selected as the right humerus data was incomplete for one of the children. An adult cohort was used in the third study (study III, Chapter seven) which investigated osteoporotic hip fractures during sideway falls. A detailed description of the two cohorts is provided below.

4.1.1 Paediatric cohort

This retrospective cohort includes anonymized QCT scans of the whole body of 30 children. These scans were performed and obtained as part of an on-going study at the Sheffield Children's Hospital. Research Ethics Committee (IRAS181203, REC15/WM/0242), HRA and local R&D approval (SCH/15/064) were obtained as part of the larger clinical study titled, "Utility of Post-Mortem Computed Tomography and Magnetic Resonance Imaging for Assessing Cause of Death, Developing Finite Element Models and Understanding Bone Pathophysiology in Children". Li et al. (2015) reported 15 cases from this same dataset but this has now been extended to 30 cases. The CT images were obtained using a GE Lightspeed 64-slice CT scanner, with a typical image resolution of 0.625×0.625×0.625 mm^3. All the scans were performed with 100 kVp and two different tube currents (60 and 100 mA). The data was anonymized and the age for each individual was corrected for prematurity at birth (40 weeks as full term). The cohort age ranged from new-born to three years old. Further details of these cases are shown in Table 4.1. The right femur of each child was extracted and used in study I. The humeri of those within the age range to initiate rolling (approximately four to six months)

were used in study II (Cases 23, 24 and 25). These cases are referred to in Chapter 6 as Cases 1, 2, and 3, respectively. Because one of these cases had a damaged right humerus, the left humeri of all three children were extracted and used for this study.

Table 4.1: Descriptive statistics of the paediatric cohorts. The three cases used in study II are highlighted in the box with red text.

Case	Gender	Age (weeks)	Body mass (g)	Height (cm)	Cause of death
1	M	0	3300	51	Pneumonia Pertussis
2	F	0	3075	51	SIDS
3	F	0	2590	54	Decomposed
4	F	1	3265	56	1a Sepsis 1b: necrotising enterocolitis
5	F	1	3585	57	Early sudden neonatal collapse leading to HIE
6	F	2	2248	47	SIDS
7	M	2	4005	59.5	Hypoplastic left heart syndrome
8	M	2	3655	55	Persistent hypertension of the new-born
9	M	3	3240	53	SIDS
10	F	4	2830	53	Superior sagittal sinus haemorrhage due to Aplasia cutis congenita
11	F	4	4185	59	S Aureus sepsis
12	M	7	4400	55	SIDS
13	F	8	3825	51	Cri-du-Chat syndrome and Chromosome 3 duplication
14	F	9	5260	63	SIDS
15	M	10	7565	68	Severe acute bronchopneumonia
16	M	11	5500	58	SIDS
17	F	12	5890	63	SIDS
18	F	12	6375	67	SIDS
19	M	12	6530	66	Subdural haemorrhage and brain oedema
20	F	12	5890	63	SIDS
21	M	14	6505	62	SIDS
22	M	14	4525	60	Cardiomyopathy
23	**M**	**16**	**3850**	**60**	**SIDS**
24	**F**	**16**	**5790**	**65**	**Unascertained**
25	**M**	**24**	**7025**	**69**	**SIDS**
26	M	40	7145	66	SIDS
27	M	1 year	12980	82.6	SIDS
28	F	1 year	10940	79	SIDS
29	F	2 years	13130	92	Inhalation of products of combustion
30	F	3 years	17500	102.5	Non-accidental head injury

M: male; F: female
SIDS: sudden infant death syndrome
The height was measured from the crown of the head to the toe.

4.1.2 Adult cohort

The retrospective adult cohort consisted of 98 postmenopausal women. This cohort was used in study III. The cohort was divided into two groups: a fracture group and a control group. The fracture group consisted of 49 women who had been diagnosed with low energy trauma fractures in the proximal femur. The control group consisted of 49 women who were pair-matched for age, height and weight. Details of the cohort are shown in Table 4.2. All patients received proximal femur CT scans with a slice thickness of 0.625 mm and a pixel size of 0.74 × 0.74 mm^2. All scans were performed with 120 kVp and a tube current of 80-200 mA. The cohort was reported in a previous study conducted by Qasim et al. (2016).

Table 4.2: Descriptive statistics for adult cohorts divided into control and fracture groups.

	Control (N=49)	**Fractures (N=49)**
Age (years)	**7**5±8	75±9
Weight (kg)	64 ±12	62±14
Height (cm)	158±5	158±7

Age, weight and height are given as mean ± SD.
N is the number of cases

4.2 Finite element theory

Bone deforms and become internally stressed due to prescribed loading conditions. It is considered to be a continuum isotropic and non-homogenous body and its deformability is described by the general theory of elasticity. This theory is formulated as a partial differential equation and cannot be solved in a closed form for a general integration domain (for a general geometry). This means that numerical methods need to be used to solve this kind of problem. Although several methods can be used to solve partial differential equations, the one that is most effective for boundary value problems is the finite element method. Finite element analysis has therefore been widely used to investigate the behaviour of bone tissue. A brief description of finite element theory is provided below.

The finite element method belongs to the class of generalized Galerkin methods, which convert a continuous operator problem, such as a partial differential equation, to a discrete problem. The basic concept of finite element theory is dividing the mathematical model (based on physical laws) into components called finite elements (Figure 4.1). The physical laws

and relative equations are then applied to each element. The collection of elements is assembled together to produce the discrete model. Finally, the response of the mathematical model is approximated.

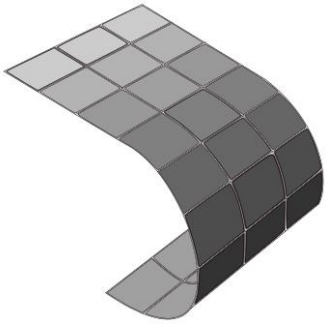

Figure 4.1 Surface discretization of an object using shell elements.

4.2.1 Infinitesimal strain theory

When the deformations of a body, that is under external forces, are much smaller than the dimensions of the body, the presented strains are referred to as small or infinitesimal strains. According to this theory, during the deformation process the geometry and the constitutive material properties must be unchanged (Slaughter and Petrolito, 2002): the whole system has to be under equilibrium condition, which means that the external forces field is equal to the internal forces field.

4.2.2 Equilibrium equations

For a conservative system (a system in which the total energy remains constant with time), the equilibrium condition is achieved by minimizing the total potential of the system. Hence, the equilibrium displacement vector can be found by solving the following partial differential equation (Viceconti, 2012):

$$\boldsymbol{u} \rightarrow \frac{\partial \prod}{\partial \boldsymbol{u}} = 0 \qquad (4.1)$$

Where $\boldsymbol{u}$ is the displacement, and $\prod$ is the potential energy of the body which can be defined as the summation of the integrals of the strain energy density ($\int_V \ W\ dV$), the work of the volumetric forces ($\int_V \ G\ dV$), and the work of the surface forces $\left(\int_S \ g\ dS\right)$:

$$\prod = \int_V \ W\ dV + \int_V \ G\ dV + \int_s \ g\ dS \tag{4.2}$$

Where:

V is the volume, W is the strain energy density function, G is the elastic constant, S is the external surfaces, and g is the gravitational pull. The variational form of equation 4.2 is:

$$\partial\prod = \int_V \ \partial W\ dV + \int_V \ \partial G\ dV + \int_s \ \partial g\ dS \tag{4.3}$$

Equation 4.3 can be minimized by using the displacement vector field to solve the problem. If all the forces acting on the body are conservative, then the volume forces (***F***) and the surface forces (***T***) can be formed as:

$$\boldsymbol{F} = \frac{\partial G}{\partial \boldsymbol{u}} \quad \text{and} \quad \boldsymbol{T} = \frac{\partial g}{\partial \boldsymbol{u}} \tag{4.4}$$

and, the strain energy density can be written in the form:

$$\boldsymbol{\sigma}_{ij} = \frac{\partial W}{\partial e_{ij}} \tag{4.5}$$

where $\boldsymbol{\sigma}_{ij}$ is the stress and e_{ij} is the strain. By substituting equations 4.4 and 4.5 in equation 4.3, the following equation is obtained:

$$\partial\prod = \int_V \ \boldsymbol{\sigma}_{ij}\partial e_{ij}dV - \int_V \ \boldsymbol{F}\partial\boldsymbol{u}dV - \int_s \ \boldsymbol{T}\partial\boldsymbol{u}\ dS = 0 \tag{4.6}$$

Now equation 4.6 can be more easily solved numerically for the displacement vector field, which minimizes the variational form. By transferring the key quantities into vector form, all forces could be written as below:

$$\boldsymbol{f^B} = \begin{bmatrix} f_x^B \\ f_y^B \\ f_z^B \end{bmatrix} \quad \boldsymbol{f}^S = \begin{bmatrix} f_x^S \\ f_y^S \\ f_z^S \end{bmatrix} \quad \boldsymbol{R}_C^i = \begin{bmatrix} R_{cx}^i \\ R_{cy}^i \\ R_{cz}^i \end{bmatrix} \tag{4.7}$$

where $\boldsymbol{f^B}$ is the volume forces vector,$\boldsymbol{f^S}$ is the surface forces vector, and $\boldsymbol{R}_C^i$ is the concentrated forces vector.

The displacement of each point of the body with respect to the undeformed configuration is described by:

$$\boldsymbol{u}(x,y,z) = \begin{bmatrix} u \\ v \\ w \end{bmatrix} \tag{4.8}$$

Assuming a small deformation and displacement, the small strain tensor can be written in the vector form as follows:

$$\boldsymbol{\varepsilon}^T = [\varepsilon_x \quad \varepsilon_y \quad \varepsilon_z \quad \gamma_{xy} \quad \gamma_{yz} \quad \gamma_{zx}], \tag{4.9}$$

where:

$$\varepsilon_x = \frac{\partial u}{\partial x}; \qquad \varepsilon_y = \frac{\partial v}{\partial y}; \qquad \varepsilon_z = \frac{\partial w}{\partial z}$$

$$\gamma_{xy} = \frac{\partial u}{\partial y} + \frac{\partial v}{\partial x}; \quad \gamma_{yz} = \frac{\partial v}{\partial z} + \frac{\partial u}{\partial y}; \quad \gamma_{zx} = \frac{\partial w}{\partial x} + \frac{\partial u}{\partial z} \tag{4.10}$$

Similarly, the small stress tensor can be written in the vector form as follows:

$$\boldsymbol{\sigma}^T = [\sigma_x \quad \sigma_y \quad \sigma_z \quad \tau_{xy} \quad \tau_{yz} \quad \tau_{zx}], \tag{4.11}$$

where σ is the normal stress and τ is the shear stress.

According to Hooke's law:

$$\boldsymbol{\sigma}^T = E \cdot \boldsymbol{\varepsilon} \tag{4.12}$$

where E is the elasticity matrix, which is a 6×6 matrix.

Although bone is widely recognized as orthotropic material rather than isotropic, only few studies have adopted the orthotropic material properties in there models (Taylor et al., 2002; Wirtz et al., 2003). However, the impact of assigning orthotropic materials to the finite element model was not clear in these studies. The effect of assigning orthotropic materials property on the finite element model was later compared against the isotropic materials using the same model (Peng et al., 2006). It has been found that the differences in computational results (von Mises stresses and nodal displacements) between the two material property assignments were small. Therefore, the majority of the finite element studies available in the literature (as mentioned in Section 3.5) used isotropic material properties. Similarly, in this thesis, bone is also considered an isotropic material.

The nine non-null elements of the elasticity matrix can be expressed as a function of the Poisson ratio v and the Young modulus E:

$$E_{11} = E_{22} = E_{33} = (1 - v)c \tag{4.13}$$

$$E_{12} = E_{23} = E_{13} = vc \tag{4.14}$$

$$E_{44} = E_{55} = E_{66} = G \tag{4.15}$$

where c and G are the material dependent quantities and are equal to:

$$c = \frac{E}{(1+v)(1-2v)} \text{ and } G = \frac{E}{2(1+v)} \tag{4.16}$$

Under equilibrium conditions, the work of the external forces must be equal to that of the internal forces and hence:

$$\int_V \mathbf{u}^T \boldsymbol{f}^B dV + \int_S \mathbf{u}^{S^T} \boldsymbol{f}^S dS + \sum_i \mathbf{u}^{i^T} \boldsymbol{R}_C^i = \int_V \boldsymbol{\varepsilon}^T \boldsymbol{\sigma}\, dV \tag{4.17}$$

The first, second and third terms of the left side of equation 4.17 represent the work of the external forces: the volumetric, surface and concentrated forces, respectively. While the right side of the equation is the work of the internal forces, which represent the total deformation stored inside the body.

For a finite element problem, each element of the model consists of a set number of nodes. Consider an element (m) with a local reference system in the undeformed configuration (ξ, Ψ, ζ), then:

- The approximation of the nodal displacement field will be:

$$\widehat{\boldsymbol{u}}^{(m)}(\xi, \Psi, \zeta) = H^{(m)}(\xi, \Psi, \zeta) \cdot \boldsymbol{U} \tag{4.18}$$

where H is the displacement interpolation matrix and $\boldsymbol{U}$ is the displacement vector of a node of element m.

- The approximation of the deformation field will be:

$$\hat{\boldsymbol{\varepsilon}}^{(m)}(\xi, \Psi, \zeta) = B^{(m)}(\xi, \Psi, \zeta) \cdot \boldsymbol{U} \tag{4.19}$$

where B is the displacement-deformation matrix.

- And the approximation of the stress and strain fields could be written as:

$$\widehat{\boldsymbol{\sigma}}^{(m)}(\xi, \Psi, \zeta) = E^{(m)}(\xi, \Psi, \zeta) \cdot \hat{\boldsymbol{\varepsilon}}^{(m)} \tag{4.20}$$

Now for a body decomposed in finite elements, the global solution over the entire model will be the summation of all the local solutions that have been obtained for each element, meaning that the equation of the virtual work can be written as:

$$\sum_{m}\int_{V^{(m)}}\tilde{\boldsymbol{u}}^{(m)^T}\boldsymbol{f}^{B(m)}dV^{(m)}+\sum_{m}\int_{S_1^{(m)},S_2^{(m)},\ldots S_q^{(m)}}\tilde{\boldsymbol{u}}^{S(m)^T}\boldsymbol{f}^{S(m)}dS^{(m)} + \sum_{i}\tilde{\boldsymbol{u}}^{i^T}\boldsymbol{R}_C^i=\sum_{m}\int_{V^{(m)}}\tilde{\boldsymbol{\varepsilon}}^{(m)^T}\boldsymbol{\sigma}^{(m)}dV^{(m)} \tag{4.21}$$

By substituting Equations 4.18, 4.19 and 4.20 in Equation 4.21, the stress, strain and displacements can be expressed as a function of a single nodal displacement:

$$\tilde{\boldsymbol{U}}^T\left[\sum_{m}\int_{V^{(m)}}B^{(m)^T}E^{(m)}B^{(m)}dV^{(m)}\right]\boldsymbol{U} = \tilde{\boldsymbol{U}}^T\left[\sum_{m}\int_{V^{(m)}}H^{(m)^T}\boldsymbol{f}^{B(m)}B^{(m)}dV^{(m)} + \sum_{m}\int_{S_1^{(m)},S_2^{(m)},\ldots S_q^{(m)}}H^{S(m)^T}\boldsymbol{f}^{S(m)}dS^{(m)}+\sum_{i}\boldsymbol{R}_C^i\right] \tag{4.22}$$

Equation 4.22 could be written as follows:

$$\tilde{\boldsymbol{U}}^T\boldsymbol{K}\boldsymbol{U}=\tilde{\boldsymbol{U}}^T(\boldsymbol{R}_B+\boldsymbol{R}_S+\boldsymbol{R}_C) \tag{4.23}$$

Where $\boldsymbol{K}$ is the stiffness matrix, the right side of Equation 4.23 is the resultant of the external forces $\boldsymbol{R}$, which is the summation of the volumetric, surface and concentrated forces. For every virtual nodal displacement, the equation must be true, and this is true if:

$$\boldsymbol{K}\boldsymbol{U}=\boldsymbol{R} \tag{4.24}$$

Equation 4.24 is the fundamental equation of the finite element method. Hence, for static problems solved by finite element methods, a simultaneous set of Equation 4.24 is used where the stiffness matrix $\boldsymbol{K}$ is very large according to the number of nodes in the model.

$$K_{n\times n} = \begin{bmatrix} K_{11}\ K_{12} & \cdots & K_{1n} \\ K_{21}\ K_{22} & \dots & K_{2n} \\ \vdots & & \vdots \\ K_{n1}K_{n2} & \cdots & K_{nn} \end{bmatrix}, \quad \boldsymbol{U}_{n\times l} = \begin{bmatrix} U_1 \\ U_2 \\ \vdots \\ U_n \end{bmatrix}, \qquad \boldsymbol{R}_{n\times l} = \begin{bmatrix} R_1 \\ R_2 \\ \vdots \\ R_n \end{bmatrix} \tag{4.25}$$

The stiffness matrix K and the force are calculated; where displacement $\boldsymbol{U}$ is the unknown to be solved. The behaviour of the model depends on the material, geometry, boundary and loading conditions. These are usually very complicated for biological tissues; therefore, for practicality and versatility reasons these equations are typically solved numerically.

4.2.3 Contact mechanics

A contact system could contain one or more contact bodies. For N bodies that are in contact at time t, for each body L=1, …, N, and the contact area could be represented by ${}^{t}S_c(L)$. In equilibrium conditions, the sum of the external forces, which consist of the volumetric, surface and contact forces, is equal to the internal forces. Thus, the virtual work equations can be modified as (Zhong, 1993):

$$\begin{aligned} \sum_{L=1}^{N} \int_{{}^{t}V^{(L)}} \widetilde{\boldsymbol{u}}^{(L)^T}\ {}^{t}\boldsymbol{f}^{B(L)} d^{t}V^{(L)} + \sum_{L=1}^{N} \int_{{}^{t}S^{(L)}} \widetilde{\boldsymbol{u}}^{S(L)^T}\ {}^{t}\boldsymbol{f}^{S(L)} d^{T}S^{(L)} \\ + \sum_{L=1}^{N} \int_{{}^{t}S_c} \widetilde{\boldsymbol{u}}^{c(L)^T}\ {}^{t}\boldsymbol{f}^{c(L)} d^{T}S^{(L)} \\ = \sum_{L=1}^{N} \int_{{}^{t}V^{(L)}} \tilde{\boldsymbol{\varepsilon}}^{(L)^T}\ {}^{t}\boldsymbol{\sigma}^{(L)} d^{t}V^{(L)} \end{aligned} \tag{4.26}$$

A two-body contact is the most common contact system, involving two surfaces in contact. The type of contact depends on the nature of the contact surfaces. When contact problems are solved by the finite element method, for a rigid-deformable contact, the surface of the deformable object is called the contact surface, while the surface of the rigid object is called the target surface. The two objects are called a contact pair (ANSYS, Inc. Theory Reference). Nodes on the contact surface are defined as the slave nodes, whereas nodes on the target surface are defined as the master nodes. Both master and slave nodes are called the integration points, where all contact equations are solved.

Considering a two-body contact system, the boundaries of the contact surfaces are denoted by Γ^1 (on the contact surface) and Γ^2 (on the target surface). Both surfaces slide over each other and so a penetration might occur. To avoid this penetration, the following condition has to be achieved (Wriggers, 2007):

$$(x^1 - x^2) \cdot \boldsymbol{n}^1 \geq 0 \tag{4.27}$$

Where: x^1 is the location of the slave node on the contact surface, x^2 is the location of the master nodes on the target surface, and $\boldsymbol{n}^1$ is the normal vector of the contact surface pointed towards the target surface.

The distance between the slave and master nodes can be used to define the amount of the gap/penetration between the two surfaces. By assuming a local contact boundary, as shown in Figure 4.2, a point $x^1 = x^1(\bar{\xi})$ on Γ^1 can be related to every point x^2 on Γ^2 via the minimum distance problem, where $\xi = (\xi^1, \xi^2)$ represent the parameterization of the boundary Γ^1 (Wriggers, 2007):

$$\hat{\mathrm{d}}^1(\xi^1, \xi^2) = \|x^2 - x^1\| = \min_{x^1 \subseteq \Gamma^1} \|x^2 - x^1(\xi)\| \tag{4.28}$$

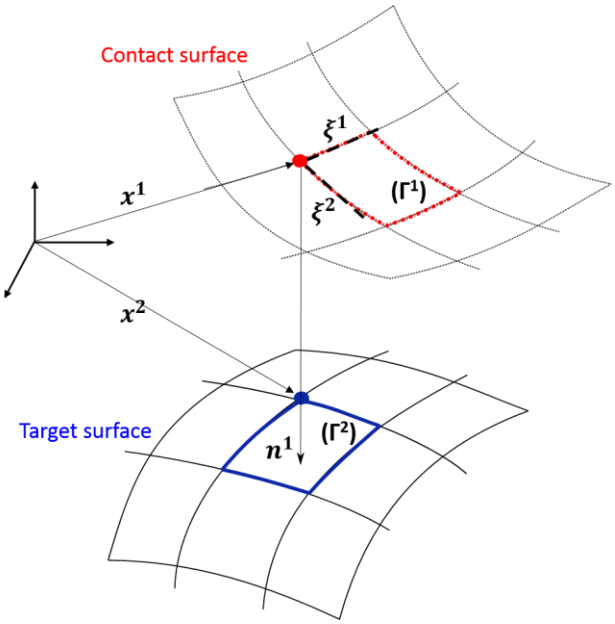

Figure 4.2 Minimum distance between the integration points of the contact and target surfaces.

The state of the contact element is determined by its relative location in relation to the associated element of the target surface. When the integration points of the contact element are within an imaginary region called pinball region, they are considered to be in a near-contact field (Figure 4.3). For 3D contact problems in ANSYS, the pinball region is defined as a sphere centred about the integration point with a radius equivalent to four times the depth of the underlying element.

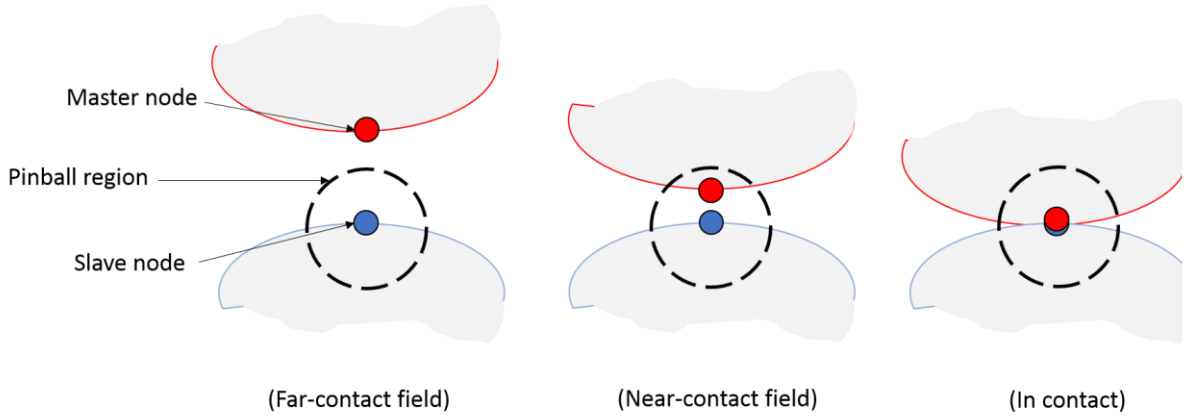

Figure 4.3 Pinball region with three contact states: far contact, near contact and in contact.

Contact is categorized as a non-linear boundary problem. This is because the stiffness matrix is a function of the nodal displacement:

$$K\Delta \boldsymbol{U} = \boldsymbol{R} + \boldsymbol{c} \tag{4.29}$$

where $\boldsymbol{c}$ is the contact forces resultant and $\boldsymbol{R}$ is the residual force. As the stiffness changes, the solution must iterate until the convergence of the solution is achieved by narrowing down the imbalance difference to an acceptable tolerance. There are several algorithms used to solve contact problems, each with its own advantages and disadvantages. The most popular algorithms are Penalty, Lagrange multiplier method, and the Augmented Lagrangian method. The penalty method involves some penetration to generate the contact force, hence producing a push back force. This push-back force is controlled by a factor called the penalty factor. The larger the penalty factor, the smaller the penetration. A large penalty factor may cause the problem to be unstable, however, since the contact force will dominate the other forces in the model. The Lagrange multiplier method requires a constraint condition (stick condition) with zero penetration. The main disadvantage of this method is the substantial number of iterations required to achieve convergence, so the computational cost is high. In

contrast, the augmented Lagrangian algorithm is an iterative series of penalty methods to find the exact solution of Lagrange multiplier. This makes the solution less sensitive to the stiffness matrix (Wriggers, 2007).

As mentioned earlier, for nonlinear contact problems, the approximate solution is found by an iterative process based on specific convergence criteria. In general, the solution converges when the input energy of the model (through the loads) roughly equals the output energy of the model (through reactions). The convergence criterion defines how close to this exact balance is acceptable. ANSYS uses the Newton Raphson Method to solve these kinds of problems. This is an iterative method used to find an approximation value of the root of a nonlinear equation by using a linear approximation with corrections. There are a number of solvers used to solve the iterative solution, however, the most common for finite element problems are the Sparse and the Preconditioned Conjugate Gradient (PCG) solvers. The difference between these solvers is that the Sparse solver is a direct solver with an exact solution, while the PCG is an iterative solver which requires a tolerance factor and hence the solution is easily achieved. The PCG solver is more efficient for large problems such as contact with a non-linearity boundary as it is much faster than the Sparse solver (Saint-Georges et al., 1996).

4.3 General finite element analysis workflow

CT-based finite element analysis has been frequently used to model long bones and the approach has been extensively validated (Dall'ara et al., 2012; Taddei et al., 2006). This method was selected to examine the behaviour of long bones in both paediatric and adult applications in this thesis. In order to generate computer models from CT scans, several pre-processing operations must be performed. These operations include: extracting the 3D geometry from the scans, generation of the finite element mesh, mapping of the material properties from the CT scans, and the definition of the coordinate system (model alignment). These steps will be described in the next few sections.

4.3.1 Segmentation

The segmentation process involves extracting the 3D geometry of the bone from a set of CT scans. There are a range of programs that can be used for this purpose (e.g. AMIRA, ScanIP,

etc). Here ITK-Snap[3] was used to perform semi-automatic segmentation (see Figure 4.4). To start with, a region of interest was selected before a threshold value (defined by Hounsfield unit) was applied to isolate the bone from surrounding soft tissues. The bone was then segmented using the automatic segmentation tool in the software. The segmentation results were checked by the operator in order to guarantee that the isolated geometry is representative of the bone. In the case of the paediatric study, the segmentation results were checked by an experienced paediatric radiologist in order to ensure an accurate representation of the children's bones. For very young children (a few months old), because the proximal and distal ends of the femur were yet to appear, segmentation in these regions was focused only on the ossification centres. Figure 4.5 shows a few illustrative segmentation results for the right femora for children, and for the proximal femur of an elderly woman.

(A)

(B)

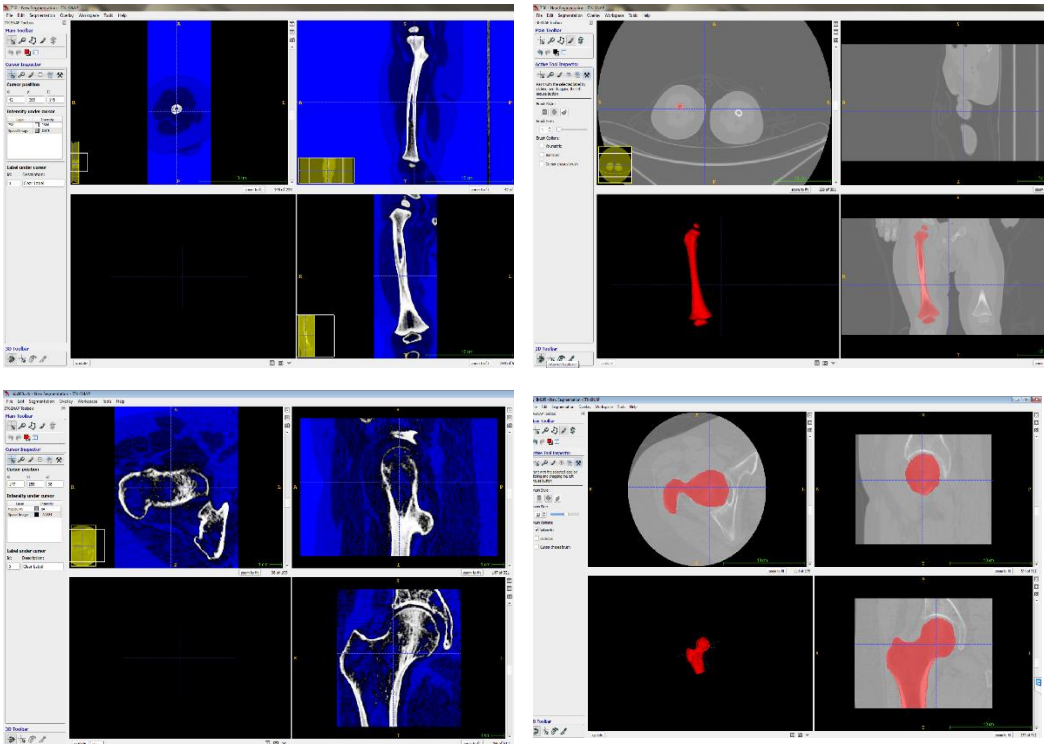

Figure 4.4 Screenshots of the segmentation process for paediatric and adult bone using ITK-Snap: (A) The right femur of a 1 year old child; (B) The right proximal femur of an 84 year old woman.

[3]. http://www.itksnap.org

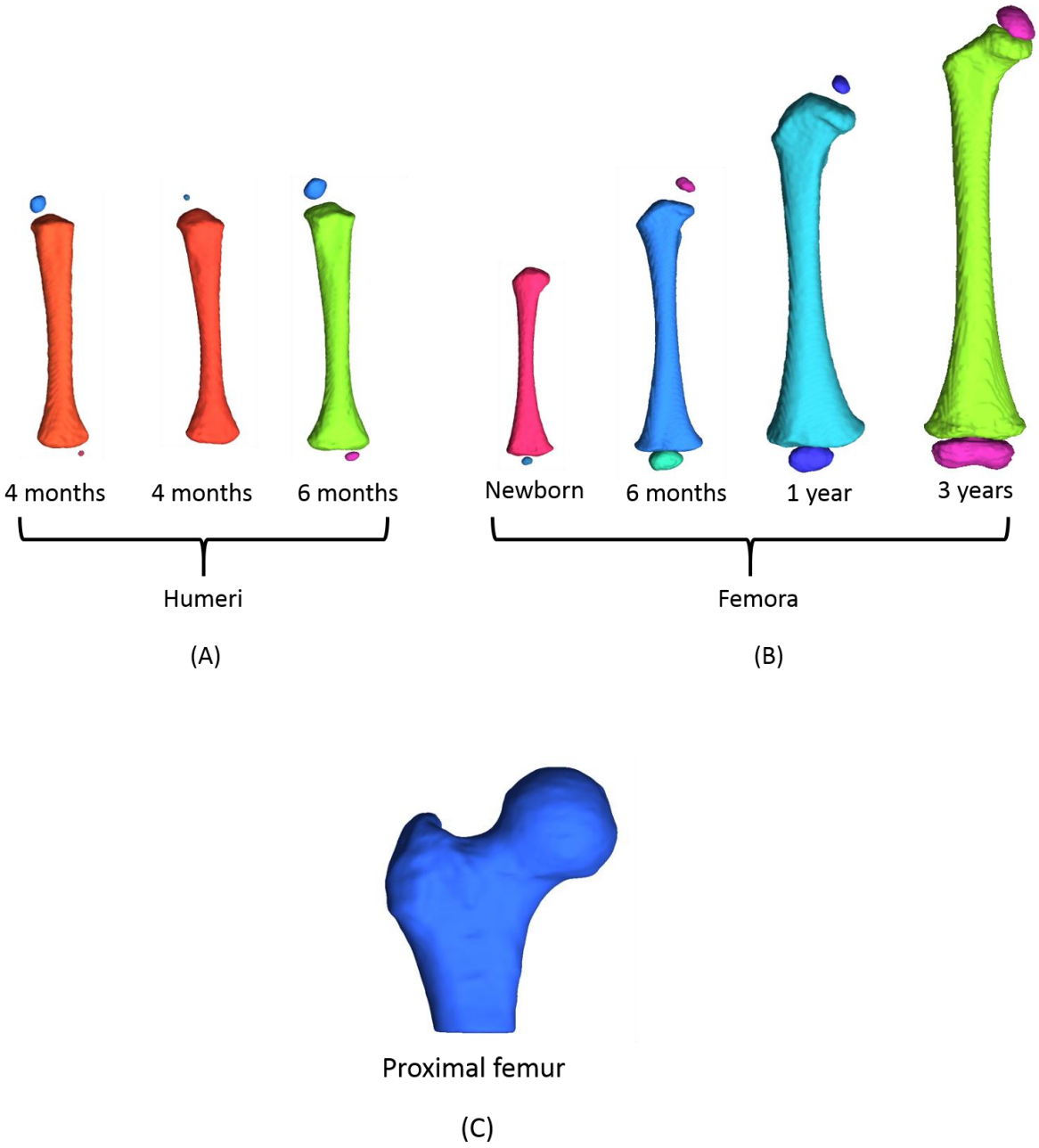

Figure 4.5 Anterior view for the segmented geometries: (A) Left humeri with the proximal and distal ossification centres. An absence of the ossification centre means it is not visible in the scan. (B) Right femora with the proximal and distal ossification centres. (C) The right proximal femur of an 84 year old woman. Note that the figures are not to scale, the size of the bone shown above is for illustrative purposes only.

4.3.2 Meshing

Meshing is an essential step when developing a FE model. The meshing process involves discretization of the whole geometry into a number of elements, as described in Section 4.2

The meshing protocols used here employed a ten-node tetrahedral mesh with three degrees of freedoms per node: the translations in the x, y and z directions. The segmented bone surface was automatically meshed in ICEM CFD 15.0 (Ansys INC., PA, USA). Figure 4.6 shows the meshed model of a paediatric femur used in study I, a paediatric humerus used in study II, and an adult proximal femur used in study III. The element size of the model in each study was decided after the mesh convergence study, which is detailed in each relevant chapter later on in the thesis.

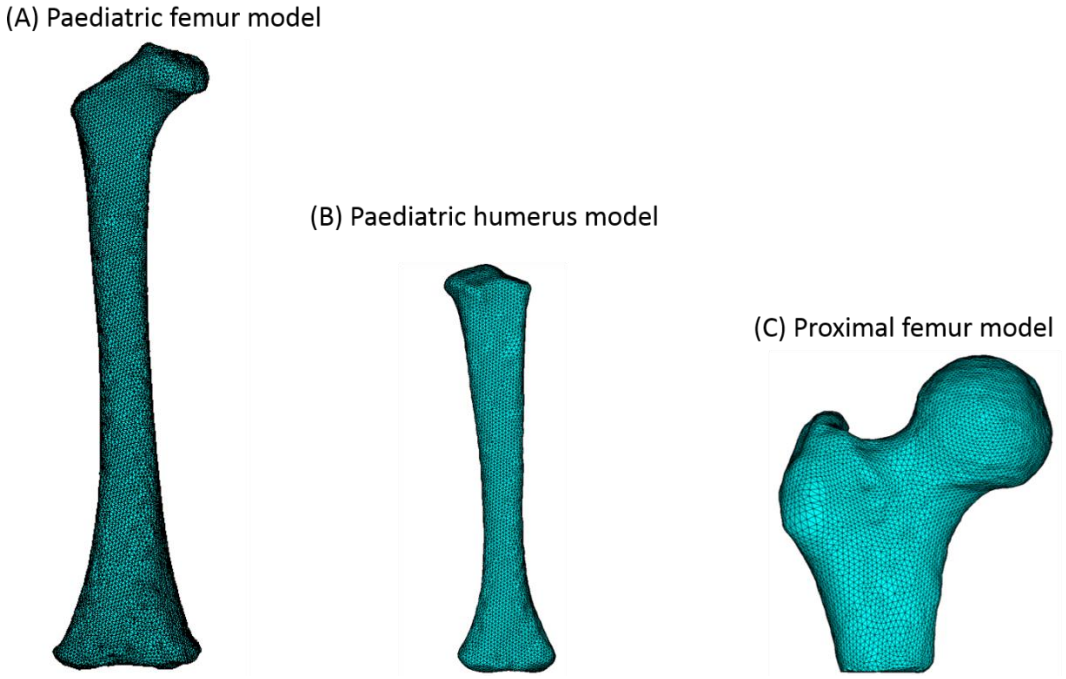

Figure 4.6 Finite element mesh for the three different models used in this thesis: (A) A paediatric femur model of a three year old, (B) A paediatric humerus model of a six month old, and (C) An adult proximal femur of an elderly woman.

4.3.3 Material properties mapping

The density of the tissue scanned by QCT can be measured from the attenuation coefficient, or the Hounsfield unit (HU). The HU is a linear transformation of the attenuation coefficient. The standard HU for water, air and compact bone are defined as 0, -1000, and 1000, respectively (Norton and Gamble, 2001). Based on the CT attenuation in the scan, the elastic modulus or Young's modulus of the bone tissue can be calculated. A well-validated material-mapping procedure (Bonemat v3, Rizzoli Institute) (Schileo et al., 2008a, 2008b; Taddei et al., 2004; Zannoni et al., 1998) has been used here to estimate the material properties of bone in the finite element models. Details of the material mapping procedures are described below:

The CT density (ρ_{CT}) was estimated from the grey scale value (grey) for each individual:

Study I & II (paediatric):

$$\text{For } 60\text{mA}: \quad \rho_{CT} = 0.0007035\ \text{grey} - 0.01185$$
$$\text{For } 100\text{mA}: \quad \rho_{CT} = 0.0007079\ \text{grey} - 0.01222 \tag{4.30}$$

Study III (adult):

$$\rho_{CT} = 0.0008264\ \text{grey} - 0.00919 \tag{4.31}$$

For Study I, since two different tube currents were used (60 & 100 mA), two different sets of parameters have been derived, as shown in equation 4.30. These parameters were derived through retrospective calibrations performed on the relevant CT scanners using a European Spine Phantom[4].

The ash density (ρ_{ash}) and apparent density (ρ_{app}) were estimated following the relationship proposed by Schileo et al. (2008a):

$$\rho_{ash} = 0.8772\ \rho_{CT} + 0.07895 \tag{4.32}$$

$$\frac{\rho_{ash}}{\rho_{app}} = 0.6 \tag{4.33}$$

There are a number of density-elasticity relationships available in the literature which are derived from mechanical tests on human bone (Carter and Hayes, 1977; Keller, 1994; Morgan et al., 2003). Schileo et al. (2007) investigated the three derived relationships to map the mechanical material properties onto the FE model. The study was validated against experiment, and the authors selected Morgan's relationship as it was obtained from robust

[4]. http://www.qrm.de/content/pdf/QRM-ESP.pdf

experimental protocols that minimised random errors. Using this equation, Schileo et al. (2007) found an accurate strain predictions of the FE models, and reported this as an applicable relation to a wide range of bone density. Furthermore, Morgan's relationship has been used to map the material properties on both the adults' FE models (aimed to classify the fracture status of retrospective cohort) (Falcinelli et al., 2014; Qasim et al., 2016) and children FE models (aimed to study the mechanical response of paediatric long bone to external loads) (Li et al., 2015). Therefore in thesis, the modulus of elasticity was calculated using the relationship proposed by Morgan et al. (2003):

$$E = 6850\ \rho_{\text{app}}^{1.49} = 14664\ \rho_{\text{ash}}^{1.49} \tag{4.34}$$

4.3.4 Reference systems

The well-known method used to define the coordinate system for adult bone (Wu et al., 2002) is not valid for paediatric long bone, due to the geometrical differences between paediatric and adult long bones. Paediatric long bones are not fully-grown, therefore key anatomical features such as the greater and lesser trochanters, condyles and a distinct femoral head are missing from the geometry. As has been previously described in Section 2.3.2, paediatric long bone consists of three parts: the diaphysis, the proximal and distal ossifications. The first method of defining a coordinate system for paediatric long bone was developed by Li et al. (2015). After conducting a repeatability test on the available landmarks on very young children's long bones, the most reliable landmarks were identified as the proximal and distal ossification centres.

For both long bones, femur (right) and humerus (left), two landmarks were assigned at the proximal and distal ossification centres (Figure 4.7). For the very young cases, where the proximal ossification of the femur or the distal ossification of the humerus was not yet visible on the CT scan, the landmark location was estimated at the approximated centre of the bony boundaries of the femur and the acetabulum, or the humerus and the radius and ulna, as shown in Figure 4.8. Once these landmarks were identified, the definition of the coordinate system followed the same approach for both femur and humerus. The coordinate system of the femur is described here, however. The origin of the coordinate system was assigned at the mid-way distance between the proximal and distal landmarks. Thus, the positive direction

of the x-axis points distally towards the distal ossification centre, while the y-axis points medially towards the proximal ossification centre. The z-axis is perpendicular to the x-y plane and points to the anterior of the long bone (see Figure 4.9). A similar coordinate system was defined for the humerus.

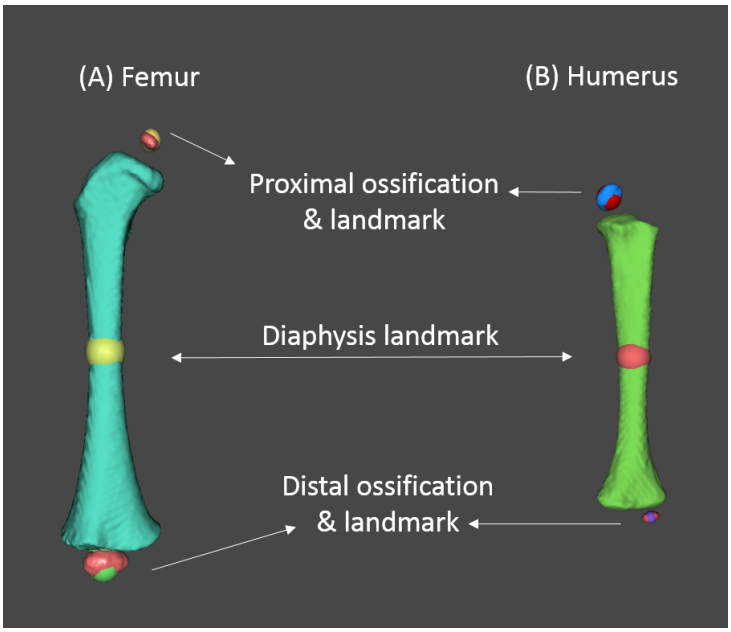

Figure 4.7 Anterior view of: (A) right paediatric femur (1 year old) and (B) left humerus (6 month old), illustrating the landmarks used to define the coordinate system. The landmarks are located at the centre of the proximal and distal ossifications and at the middle-distance between the two points, approximately in the mid-shaft of the long bone (at which the origin of the coordinate system is defined).

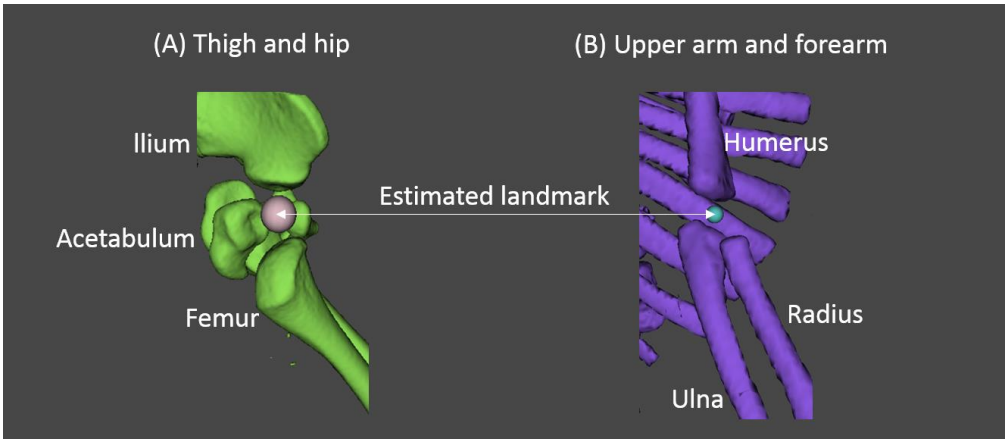

Figure 4.8 Sagittal view of: (A) thigh and hip showing the proximal epiphysis of the femur, and (B) upper arm and forearm, showing the distal epiphysis of the humerus. The locations of these landmarks were estimated at the centre of the bony boundaries.

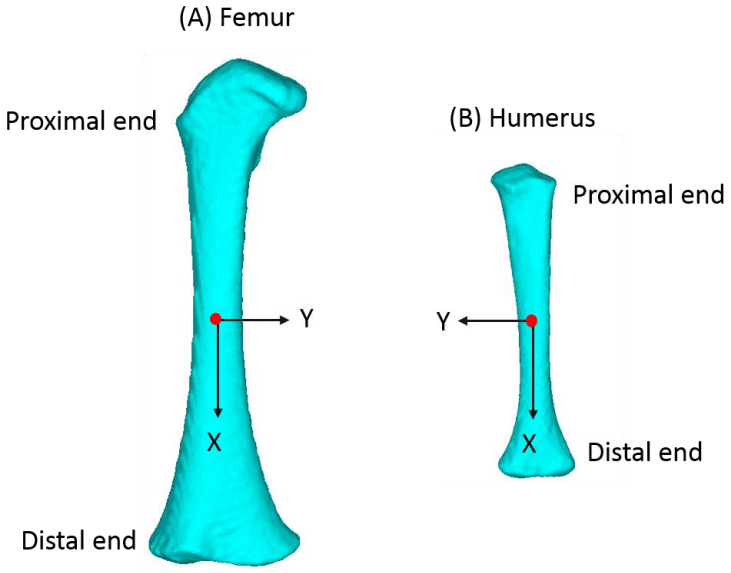

Figure 4.9 Illustration of the reference system defined for paediatric right femur and left humerus following the procedure established in Li et al. (2015). The positive z-axis pointed anteriorly (coming out of the page) for the right femur in (A), while the positive z-axis pointed posteriorly (into the page) for the left humerus in (B).

It should be noted that due to asymmetry a perfect alignment of the reference system with the long axis of the long bone shaft is difficult to achieve. The previous reference system developed by Li et al. (2015) provided a good alignment in the distal part of the femoral shaft with more deviation towards the proximal end (Figure 4.10 A). It is important to minimize the out-of-plane loading, however, by improving the alignment of the reference system for the

investigation of torsional loading. An improved coordinate system is therefore suggested here and described below.

After an investigation of using various cross-sections of the femur shaft to achieve the best alignment of the bone, not much difference was found among the various cross-sections tested. The best two cross-sections of the femoral shaft were identified at 25% and 75% of the distance between the proximal and distal ossification centre. The centroid of each of the identified cross-sections was estimated. The line passing through both centroids was defined as the X-axis (long axis). As previously described, the positive direction of y-axis pointed medially towards the proximal ossification centre, and the positive z-axis pointed towards the anterior side and perpendicular to the x-y plane (Figure 4.10 B). The improved coordinate system produced a better alignment of the x-axis with the long axis of the shaft, which in turn would help to minimize the implicit bending effect because of the geometrical asymmetry. All the paediatric FE models in study I were consistently aligned following the new procedure.

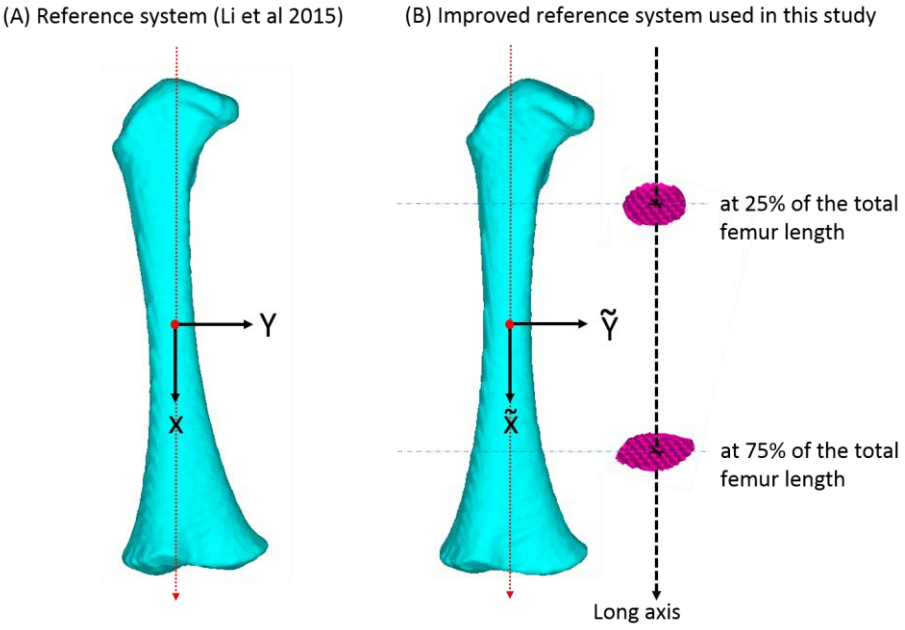

Figure 4.10 The previous reference system and improved reference system used for the finite element model of the paediatric femora (anterior view). (A) The reference system developed by Li et al. (2015), where the proximal part of the femur was not accurately aligned with the long axis of the femur. (B) The improved reference system which ensured a better alignment of both proximal and distal ends of the femur with the long axis. The improved reference system was used in this thesis to align all the femoral models in bending and torsion simulations.

For study III, all the femora were aligned using the same coordinate system based on anatomical landmarks to ensure consistency when boundary conditions were applied to the model. The femoral reference system for adults was adopted from (Qasim et al., 2016). The coordinate system is illustrated in Figure 4.11. The origin is located at the centre of the proximal femoral head. The positive y-axis points laterally towards the greater trochanter, the positive x-axis points superiorly along the longitudinal direction of the femoral shaft while the positive z-axis is perpendicular to the x-y plane and points to the anterior of the proximal femur.

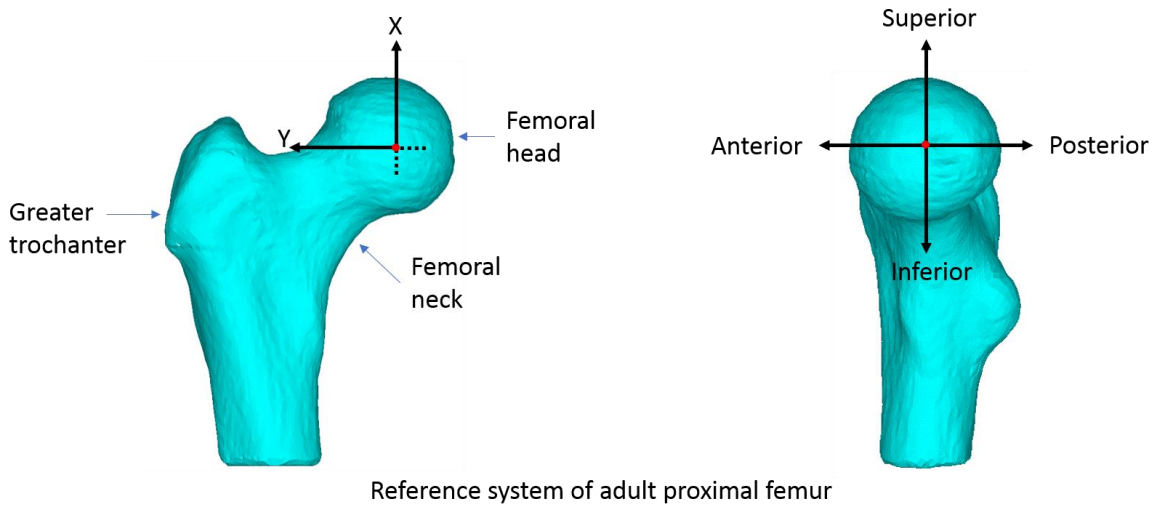

Figure 4.11 Reference system defined for the adult proximal (right) femur adopted from Qasim et al. (2016).

5 PAEDIATRIC FEMUR UNDER BENDING AND TORSIONAL LOADS (STUDY I)

5.1 Introduction

Long bone fractures are common childhood injuries. For very young children (those who are under three years old), these fractures could be the result of child abuse. This is because children aged three years and younger have limited ability to protect themselves or communicate effectively. Unfortunately, there has been little quantitative data on bone strength in this age range. The previous studies (conducted decades ago) were limited by the techniques available to investigate the mechanical response of paediatric bone when faced with limited sample sizes and age ranges (Forman et al. 2012; Miltner and Kallieris 1989; Ouyang et al. 2003). Details of these studies have been discussed in the literature review in Section 3.5.1, however, a brief recap of the reported ranges of the fracture tolerance under three-point bending tests is mentioned below.

A fracture moment ranged from 7.05 Nm to 109.5 Nm was reported by Miltner and Kallieris (1989) in respect to the intact lower limbs (including soft tissues) of a cohort aged from one day to six years old. Ouyang et al. (2003), meanwhile, reported fracture moments of 29.6, 24.3 and 39.6 Nm of three cases aged 2, 2.5 and 3 years old, respectively. The third study, by Forman et al. (2012), reported three cases (1.33 years old for one case and two cases of two years old) with fracture moments of 61.4, 61.7 and 65.5 Nm, respectively.

It is therefore clear that there is a complete lack of information on infants' bone strength between new-born and one year old. This age group is particularly challenging to characterize due to the rapid growth phase, accompanied by marked changes in anatomy and function. Obtaining paediatric long bone samples of very young children is difficult due to ethics (very few parents/carers are willing to consent). Any type of research on bone strength for very young children (zero to three years old) is quite challenging to the scientific community. Non-invasive techniques such as FE analysis based on CT have been widely applied to study the strength of bone in adults (Grassi et al. 2012; Lotz et al. 1991; Lotz and Hayes 1990). Based on a similar approach (Taddei et al. 2004; Schileo et al. 2008), a recent study by Li et al. (2015)

developed a framework to model paediatric long bones using post-mortem CT scans collected from the Sheffield Children's Hospital. The paper reported an initial four-point bending analysis of 15 paediatric femora (zero to three years old), which is the first comprehensive study of infant bone strength utilising modern medical imaging techniques.

In this chapter, the response of paediatric femora under two types of loading conditions (four-point bending and torsion) will be investigated, improving on Li et al. (2015). The cohort is expanded to include a total of 30 cases (zero to three years old). The description of the boundary conditions used to model both loading types, the analysis of the FE model, and the results will be detailed in the following sections. The relationships between bone strength and the age/body mass of the child will be reported and compared against previous studies.

5.2 Modelling approach for paediatric femur strength prediction

The right femur of each of the 30 cases of the paediatric cohort was used in the FE analysis. All FE models were tested under four-point bending and pure torsion to investigate the strength of the paediatric long bone under various loading conditions. The boundary conditions were defined in order to provide the best representation of the loading conditions. The next two sections will describe two different boundary conditions for the paediatric femur model.

5.2.1 Four-point bending model

Only the mineralized portion of the femur was used to simulate four-point bending. The mineralized portion of the femur is approximately 50% of the total length of the femur (Li et al. 2015), consisting mainly of the shaft region. The proximal and the distal ends of the paediatric femur are mainly composed of materials transitioning into mineralized bone. The contribution made by these non-mineralized tissues to bending strength would therefore be much lower than the mineralized portion. Moreover, under the current boundary condition, the non-mineralized regions would appear redundant in the simulation and hence were removed from the analysis. In order to simulate four-point bending, two nodes, one at each end of the segment, in the minimal y direction (medial) were fixed to represent the support points. Another two nodes at the two ends of the shaft, in the minimal z direction (anterior), were constrained in order to allow a partial translation in x, y and z directions. These are

shown in Figure 5.1. Two equal forces were applied in the y direction where the span of the loading is equal to half the span of the supports. Thirty-five different orientations were simulated by rotating the shaft at 10 degrees increments around the longitudinal axis. These boundary conditions were adopted from Li et al. (2015).

5.2.2 Torsion model

For the torsion model, the total length of the femur was used in order to set up an adequate boundary condition. Two additional nodes were added to the finite element model at the proximal and distal ends along the long axis (x-axis), referred to as pilot nodes. These pilot nodes where used to define the axis of rotation along the femoral shaft (see Figure 5.2). The pilot nodes were created at a distance equal to 25% of the total length of the femur. The nodes at the distal and proximal ends of the femur model were connected to the pilot nodes using the multi-point constraints (MPC) method.

The following boundary conditions were used for the torsion simulation. Distally, the translation of the distal pilot node along the longitudinal axis (x-axis) was prevented, while all the other degrees of freedom were left free. Proximally, the translations of the proximal pilot node in y and z directions were constrained and prevented from rotation in the direction of the applied moment. A torsional moment (indicated by M_X in Figure 5.2) was applied through the distal pilot node. The moment was applied in two different rotational directions to represent internal and external rotations of the leg.

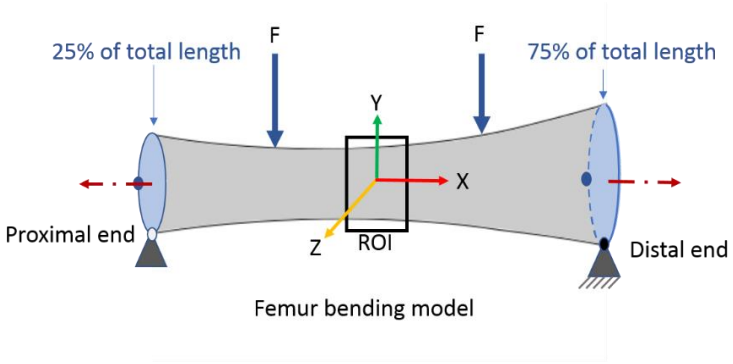

Figure 5.1 The boundary conditions applied to the model of paediatric femora used to represent four-point bending. ROI is the region of interest, indicated by the black rectangular. The black node was fixed in all directions. The white node was fixed in the y direction while the blue nodes were fixed in z directions.

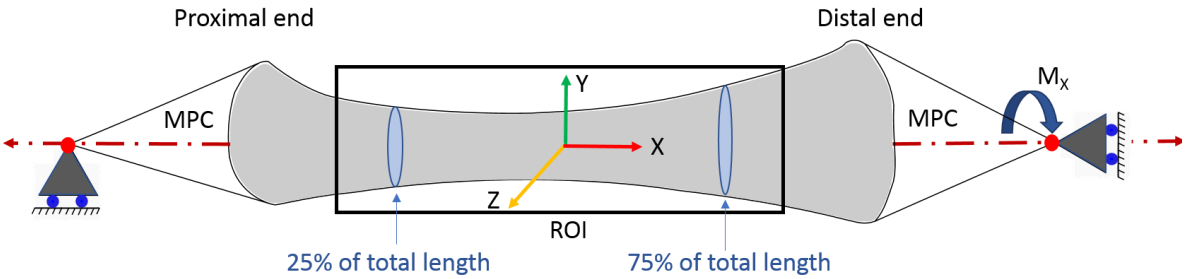

Figure 5.2 The boundary conditions applied to the model of paediatric femora used to represent pure torsion. ROI is the region of interest, indicated by the black rectangle. Red nodes are the pilot nodes, which were added to provide the model with rotational degrees of freedoms.

5.2.3 Sensitivity analyses of the mesh

The size of the element was chosen to be proportional to the length of the femur. The convergence study of the mesh was performed on three femora of a two weeks, one year, and three years old children under both bending and torsional loads. The maximum and minimum principal strains were analysed with respect to the element size. Figure 5.3 and Figure 5.4 show the convergence of the mesh for the two week old child. For this case, convergence was achieved with an element size of 0.6 mm (800,559 DOFs). The differences in the predicted e1 and e3 values between the adopted and the finest mesh were found to be less than 7% (Helgason et al., 2008). The computational time, for a single loading orientation, reduced from around 25 minutes for the finest mesh (0.4 mm) to 3 minutes for the selected mesh (0.6 mm). Similar results were obtained from the other two subjects and are omitted here for clarity.

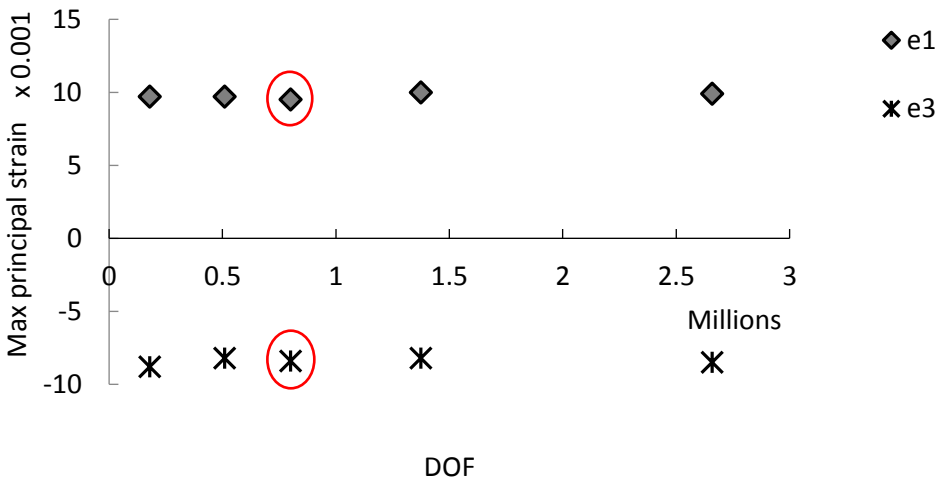

Figure 5.3 First and third principal strains (e1 and e3, respectively) plotted against the number of degrees of freedom of the femur model under bending. Five different element sizes were used to evaluate the required level of mesh refinement (0.4, 0.5, 0.6, 0.7, 1 mm). The results were obtained from a two week old child, with similar trends and converged mesh results were observed for the other two test cases.

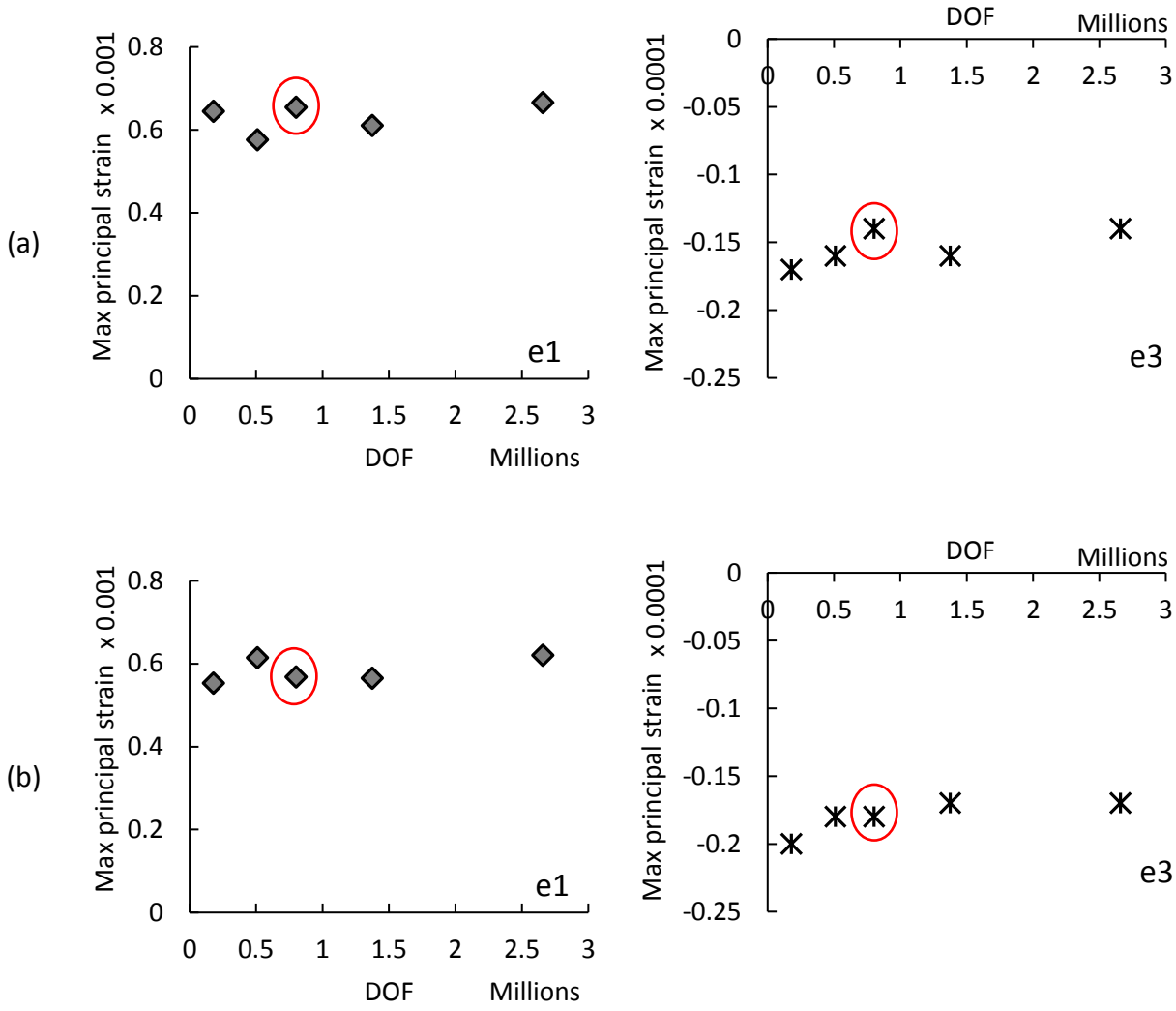

Figure 5.4 First and third principal strains (e1 and e3 respectively) plotted against the number of degrees of freedom of the femur model under (a) external rotation and (b) internal rotation. Five element sizes were used to evaluate the required level of mesh refinement (0.4, 0.5, 0.6, 0.7, 1 mm). The results were obtained from the two week old child. Similar trends and converged mesh results were observed for the other two test cases.

5.2.4 Failure criteria

The maximum principal strain criterion was used to find the failure forces. This was selected over shear strain criterion for ductile materials because fracture type is not of primary interest in the current study of paediatric bones. Instead, it is the quantification of bone strength (or failure load) that is of primary concern in this thesis. Therefore, following similar previous studies, the maximum principle strain criterion has been used here (Li et al., 2015; Tsai et al., 2017). Failure of the bone occurs when the maximum strain (within the region of interest)

reaches the threshold of the elastic strain limit (Schileo et al., 2007). For human bones, these limits are 0.73% in tension and 1.04% in compression (Bayraktar et al. 2004).

For bending, the failure force of each femur was estimated based on the maximum strain found among all the simulated orientations (35 in total). For the purposes of comparison with the previous literature, the equivalent failure moment for bending was also calculated. For torsion, the moment to fail was estimated for both internal and external torsion.

5.3 Morphological parameters of paediatric femur

5.3.1 Femoral length

The length of the femur was estimated from the CT scans as the distance between the proximal and distal ossification centres. The femoral lengths ranged from 7.74 cm to 22.41 cm, while the body height and body mass (collected during post mortem analysis) ranged from 47 cm to 102.5 cm, and from 2.25 kg to 17.50 kg, respectively. Femoral length, body height and mass all correlated with age. Four cases (cases 6, 22, 23 and 26) were noticeably lower than others at a similar age, however (≤ 2nd or ≤ 9th percentile for both body height and mass), indicating these were relatively small babies. This is shown in Table 5.1.

5.3.2 Cross-sectional changes of the femur shaft

Figure 5.5 shows a representative plot of the cross-sectional area for all subjects, illustrating the shape changes with age. Each subplot consisted of nodes on the finite element mesh at the mid-shaft cross-section. It can be seen that the majority of cases (those less than one year old) had a nearly circular cross-sectional area, with a roughly equal distance between the anterior-posterior (AP) and medial-lateral (ML) directions. For those who were older than one year, the AP diameter was generally longer than the ML diameter, giving the cross-sectional area a more elliptical shape. The cross-sectional area of each femur was therefore estimated by an ellipse. The major axis was estimated first, to be the longest distance between any two nodes in the cross section. The minor axis was then estimated as the bisector of the major axis (perpendicular to the major axis). The estimated cross-sectional area (based on an ellipsoidal shape) was ranged between 23.27 cm^2 and 209.23 cm^2. While this increased substantially with both age and body mass, it was better correlated with body mass (R^2=0.94) than age (R^2=0.89), as shown in Figure 5.6 a & b.

Table 5.1 Demographics for the cohort of study I. the last column is the peak modulus of elasticity found within the mesh, estimated from the CT attenuation.

Case no.	Gender	Age (weeks)	Body mass (kg)/ Percentile	Height (cm)/ Percentile	Femoral length (cm)	Area of X-section (cm^2)	Peak modulus of elasticity (Gpa)
1	M	0	3/25th	51/98th	7.96	0.33	15.67
2	F	0	3/25th	51/98th	7.49	0.46	17.98
3	F	0	3/25th	54/90th	8.33	0.32	18.78
4	F	1	3/25th	56/98th	8.67	0.58	19.05
5	F	1	4/50th	57/99th	8.50	0.36	18.88
6	F	2	2/2nd	47/48th	7.74	0.23	18.58
7	F	2	4/75th	60/99th	8.46	0.41	18.60
8	M	2	4/75th	55/90th	8.05	0.39	18.88
9	M	3	3/2-10th	53/50-75th	8.53	0.40	19.91
10	F	4	3/2nd	53/9th	8.44	0.26	20.42
11	F	4	4/50th	59/98th	8.75	0.34	22.57
12	M	7	4/9th	55/50-75th	9.05	0.51	16.21
13	F	8	4/9th	51/2nd	8.67	0.37	14.09
14	M	9	5/50th	63/91st	10.10	0.48	21.58
15	M	10	8/99th	68/99th	10.50	0.76	16.60
16	M	11	6/10th	58/25th	9.64	0.49	17.84
17	F	12	6/50th	63/75th	10.81	0.64	15.43
18	F	12	6/75th	67/>90th	11.14	0.61	16.44
19	M	12	7/75th	66/98th	9.99	0.62	16.14
20	F	12	6/50th	63/75th	10.79	0.77	20.31
21	M	14	7/75th	62/50th	10.62	0.64	17.39
22	M	14	5/2nd	60/9th	9.60	0.39	18.64
23	M	16	4/< 2nd	60/9th	9.63	0.42	16.91
24	F	16	6/<9th	65/91st	10.93	0.66	17.63
25	M	24	7/25th	69/50th	11.85	0.72	17.29
26	M	40	7/<9th	66/<2nd	11.00	0.76	13.10
27	M	48 (1 year)	13/91-99th	83/>99th	15.26	1.26	17.25
28	M	48 (1 year)	11/90th	79/98th	15.17	1.03	16.91
29	F	96 (2 years)	13/75th	92/98th	18.45	1.39	18.48
30	F	144 (3 years)	18/91st	103/98th	22.41	2.09	19.09

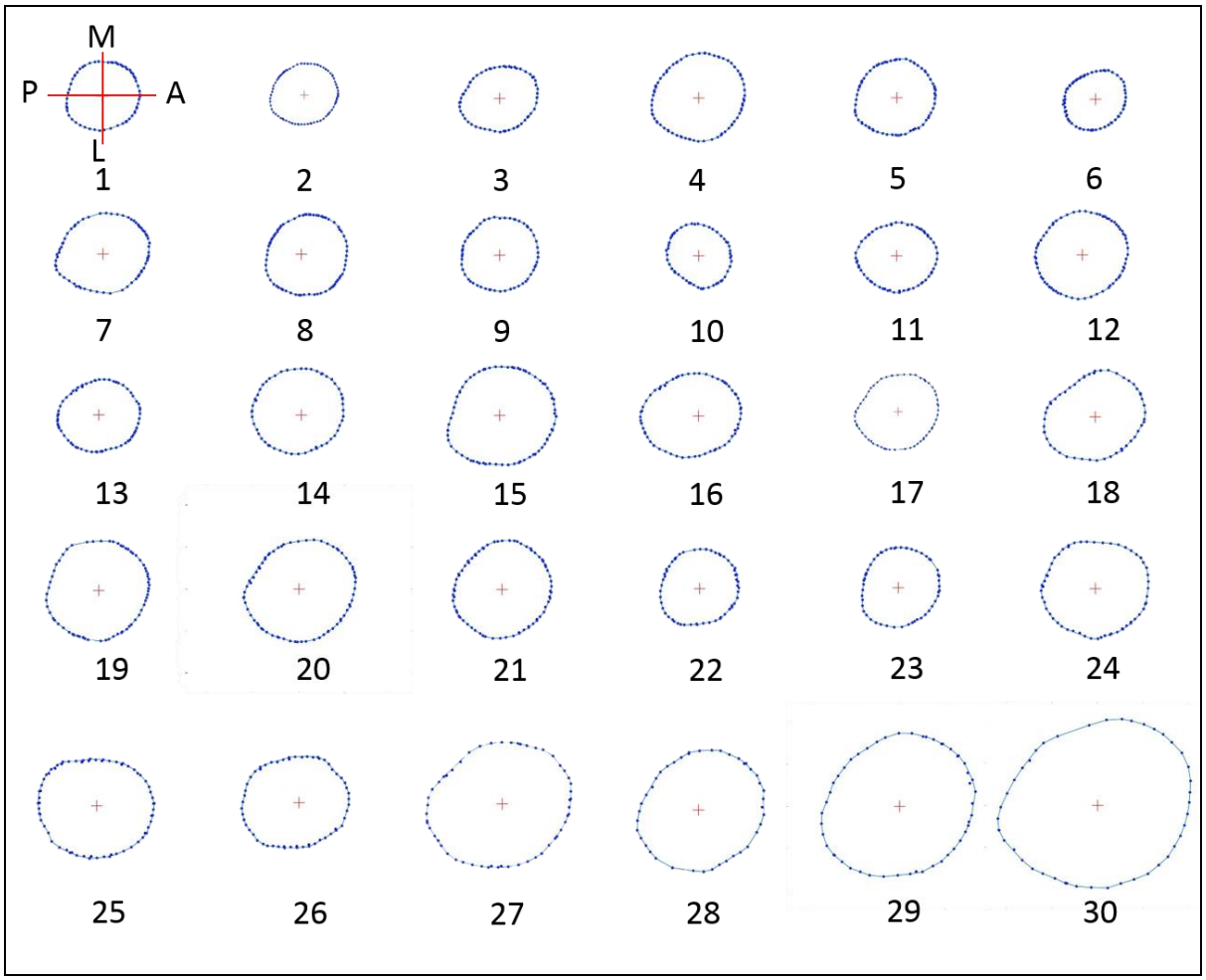

Figure 5.5 Plots of the cross-sectional area of the femur at the mid shaft for each individual in the cohort. Case number is indicated below each subplot. Readers are referred to Table 5.1 for demographic information in respect to these 30 cases. A: anterior, P: posterior, M: medial, and L: lateral.

(a)

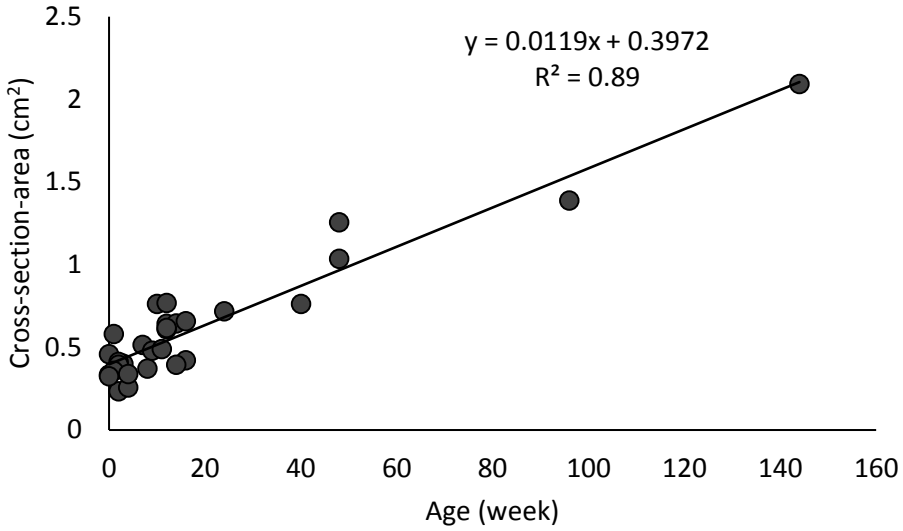

(b)

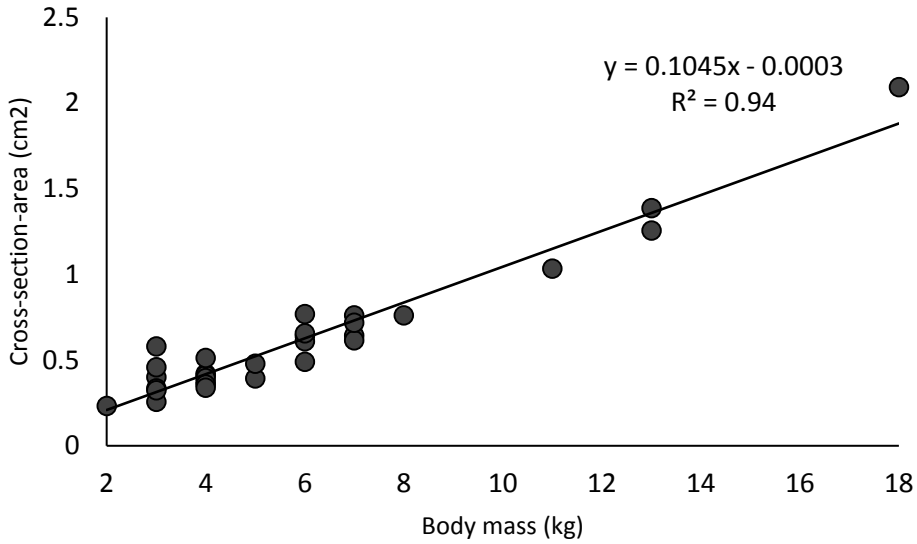

Figure 5.6 Area of the cross-section of the mid-shaft plotted against (a) age and (b) body mass.

5.3.3 Modulus of elasticity

The peak modulus of elasticity ranged from 13.10 Gpa to 22.57 Gpa (see Table 5.1). Figure 5.7 illustrates the distribution of the modulus of elasticity of four different femora at ages zero, six months, one year, and three years, in both sagittal and transverse planes. As the length and cross-sectional area increased during growth, the modulus of elasticity also increased and became more differentiated within the diaphysis of the femur.

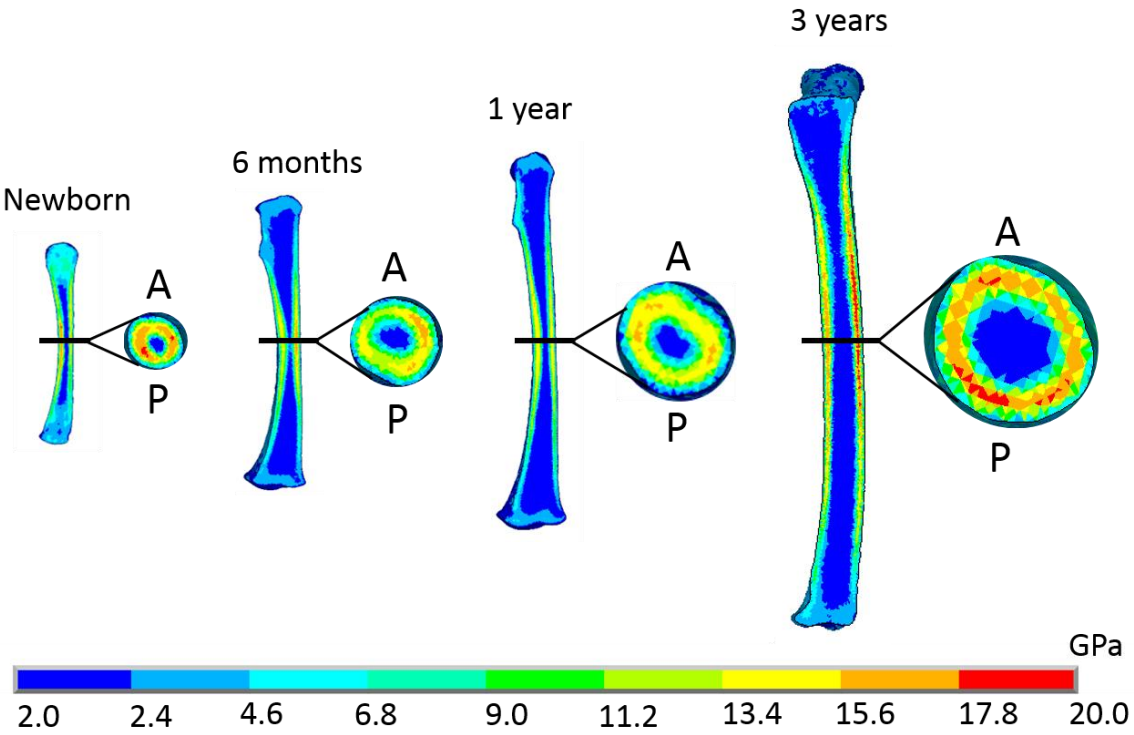

Figure 5.7 Distribution of the modulus of elasticity across the femur shown in sagittal and transverse planes at various ages. A, anterior; P, posterior.

5.4 Results

5.4.1 Failure loads and strain distribution under bending

Under four-point bending, the minimum failure moment predicted among the 35 simulated orientations ranged between 0.85 and 27.9 Nm, with an equivalent failure load of 97 N to 1022 N. In general, the predicted failure load and moment increased consistently with age. Within the current cohort, however, one child (case 26) had a lower failure load/moment in comparison to others within the similar age range. This case has been shown as an outlier (highlighted by a cross) when plotted against the age in Figure 5.8 a. This case was a 40-week-old child with a noticeably lower body mass (<9th percentile) and height (<2nd percentile), as well as peak modulus of elasticity (as shown in Table 5.1). These data suggested that this child

could have experienced some growth delay. Based on this information, the predicted failure moment was plotted against the body mass, cross-sectional area of the mid-shaft, and the femoral length in Figure 5.8 b-d. In contrast to age, these three parameters were more reflective of the musculoskeletal development. In fact, case 26 did not show up as an immediate outlier in these three plots, confirming the observation that age is not the best indicator of developmental stages.

It was difficult to derive a clear correlation between the failure moment and the demographic parameters because of the limited number of cases and the non-uniform distribution of age within the cohort (with the majority of cases being younger than one year old). Two possible regressions were therefore fitted: one linear and one quadratic, as shown in Figure 5.8. In order further to investigate the trend at this extremely young age range (between zero and six months old), the same plots were reproduced using only data between zero and six months old, as shown in Figure 5.9. Considering the whole cohort, as shown in Figure 5.8, a very good correlation was found between the failure moment and age, body mass, cross sectional area of the mid-shaft, and the length of the femur. For the extremely young age group, however, the best correlation was found with the cross-sectional area (R^2=0.86), followed by femoral length (R^2=0.74), body mass (R^2=0.71), and lastly the age (R^2=0.43).

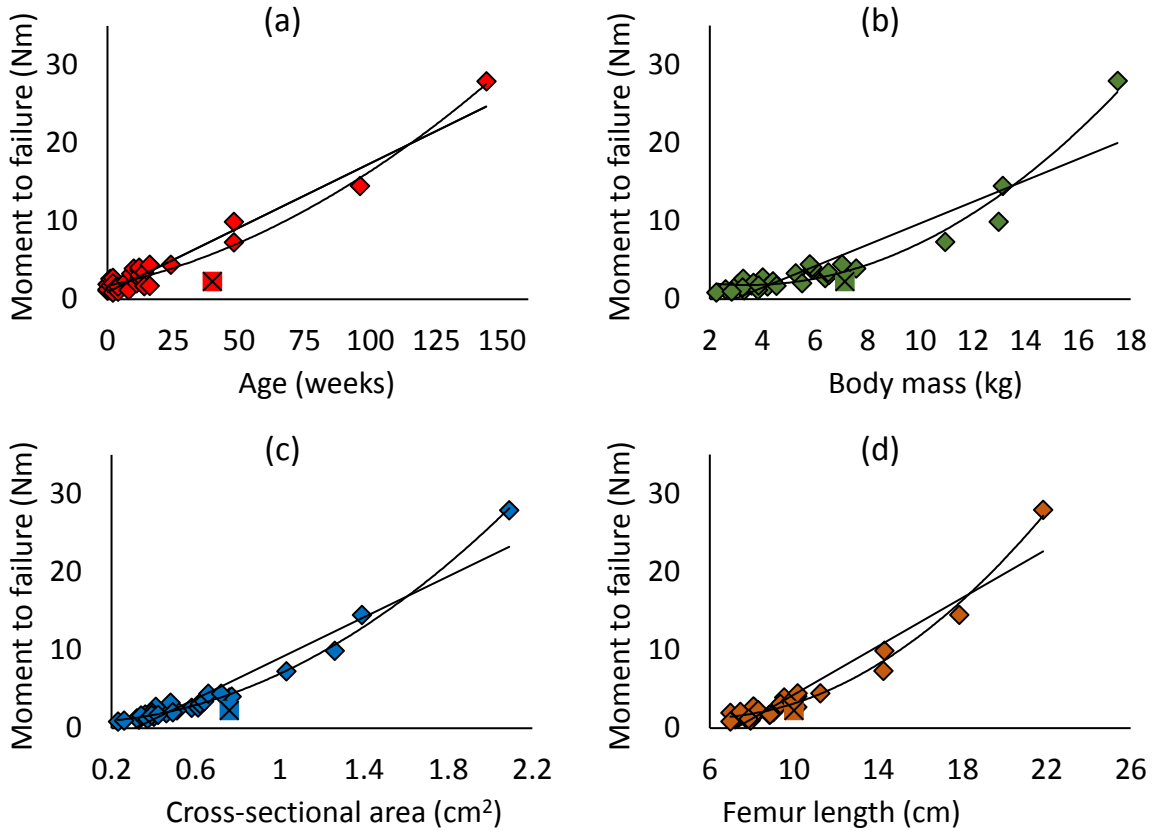

Regression equations:

$M = a \times w + b$

$M = A \times w^2 + B \times w + C$

where M is the moment to failure, w is the body mass or age, parameters a, b, A, B, C are shown below

	Linear regression	R^2	Quadratic regression	R^2
(a) Age	a= 0.165 b= 0.920	0.92	A=0.001 B=0.073 C=1.721	0.95
(b) Body mass	a= 1.370 b=- 3. 999	0.82	A=0.125 B=- 0.857 C=3.279	0.96
(c) Cross-sectional area	a= 13.064 b=- 4.075	0.91	A=6.316 B=- 0.078 C=0.738	0.98
(d) Femur length	a= 1.547 b=- -11.182	0.91	A=0.0987 B=- 1.116 C=4.443	0.98

Figure 5.8 Predicted moment to failure (Nm) when subjected to four-point bending plotted against age (a), body mass (b), cross-sectional area (c), and femoral length (d). Two possible regressions were estimated: linear and quadratic. The outlier (case 26) is indicated with a cross in each graph.

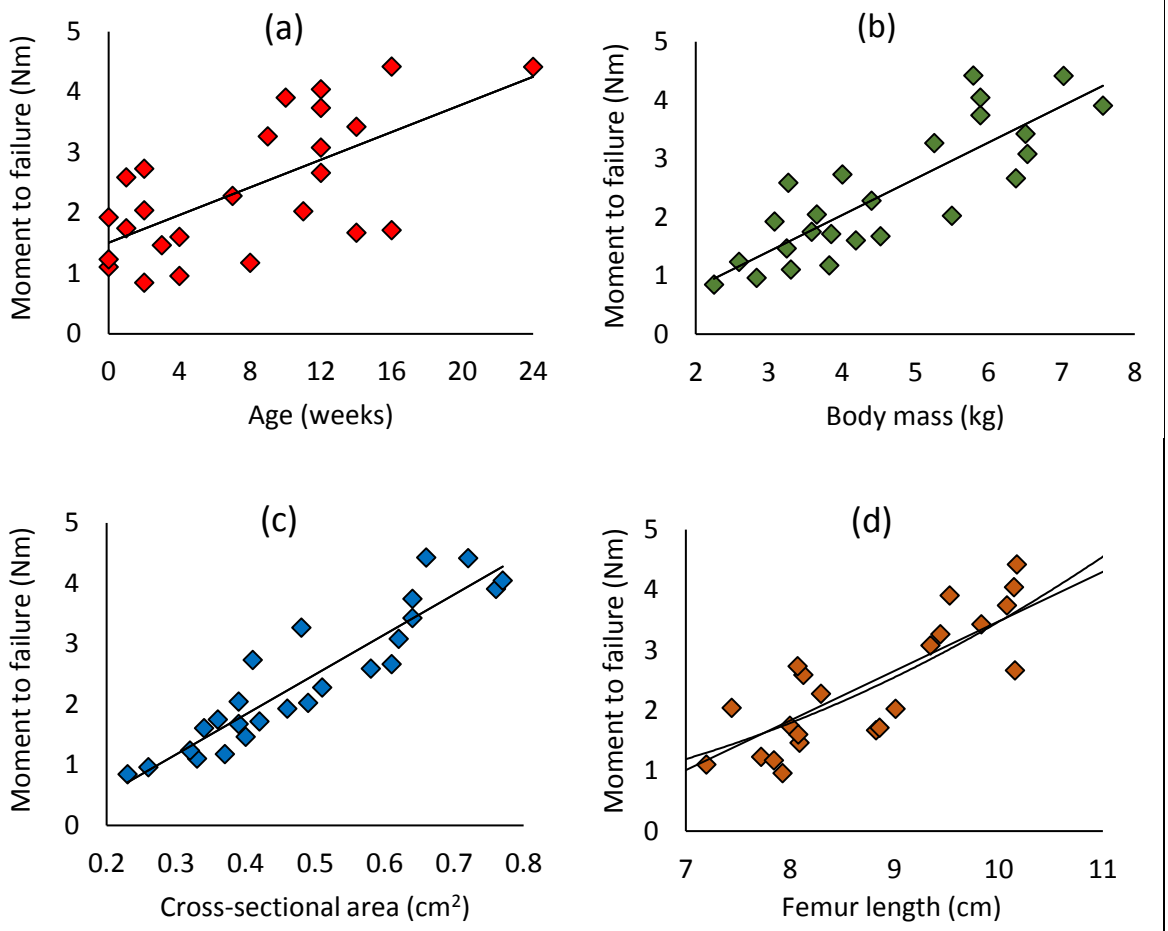

Regression equations:

$M = a \times w + b$

$M = A \times w^2 + B \times w + C$

where M is the moment to failure, w is the body mass or age, parameters a, b, A, B, C are shown below

	Linear regression	R^2	Quadratic regression	R^2
(a) Age	a= 0.114 b= 1.508	0.43	A=0.0004 B=0.107 C=1.526	0.43
(b) Body mass	a= 0.621 b=- 0.447	0.71	A=-0.015 B= 0.762 C=-0.758	0.71
(c) Cross-sectional area	a= 6.607 b=-0.808	0.86	A=0.639 B=5.956 C=0.658	0.86
(d) Femur length	a= 0.822 b=-4.743	0.73	A=0.081 B=- 0.616 C=1.547	0.74

Figure 5.9 Moment to failure (Nm) under four-point bending plotted against (a) age, (b) body mass, (c) cross-sectional area, and (d) femur length. The plotted data is for ages between zero and six months old to illustrate the trend in the very young age range.

Figure 5.10 shows the moment to failure versus age predicted by the current CT/FE study in comparison to the results of the experimental data of paediatric bone samples. In term of trend (strength increases with age), a good agreement was found between the predicted failure moment (under four-point bending) and those reported in the literature (Forman et al., 2012; Ouyang et al., 2003). However, only a small number of cases between one and three years old can be found in the literature to compare against the current study. As illustrated previously, age is not a good indicator of development, so the experimental results may not reflect the true skeletal age of the child. In terms of the moment to failure values, the current results showed a better agreement with Ouyang's study than with Forman's study. This might be because the direction of the applied load used in Ouyang's study was similar to the current study. Ouyang's study used anterior-posterior load, at which the lowest strength was predicted for most cases in the current study. In contrast, Forman's used medial-lateral load, at which the highest strength was predicted for most cases in the current study. This may explain why Forman's failure moments were higher than the other two studies in Figure 5.10.

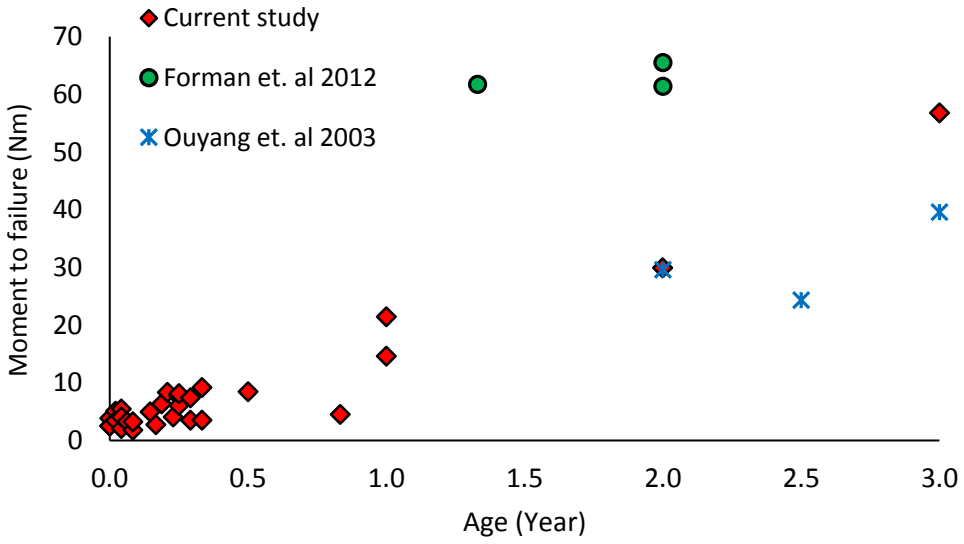

Figure 5.10 Moment to failure for four-point bending as a function of age predicted by the finite element model of study I, plotted together with the moment to failure measured in previous experimental studies.

The maximum first principal strain was usually found within the region of the narrowest cross-sectional area (mid-shaft) of the femur. The distribution of the first and third principal strains

is illustrated in Figure 5.11 for two cases. Most of the cases had higher peak first principal strains when loaded in the AP direction, rather than the ML direction, with the differences lying in the range of approximately 1% to 22%. Only three cases (cases 12, 14 and 29) had higher peak first principal strains when loaded in the ML direction than the AP direction; the absolute differences for those cases were 1%, 5% and 30%, respectively.

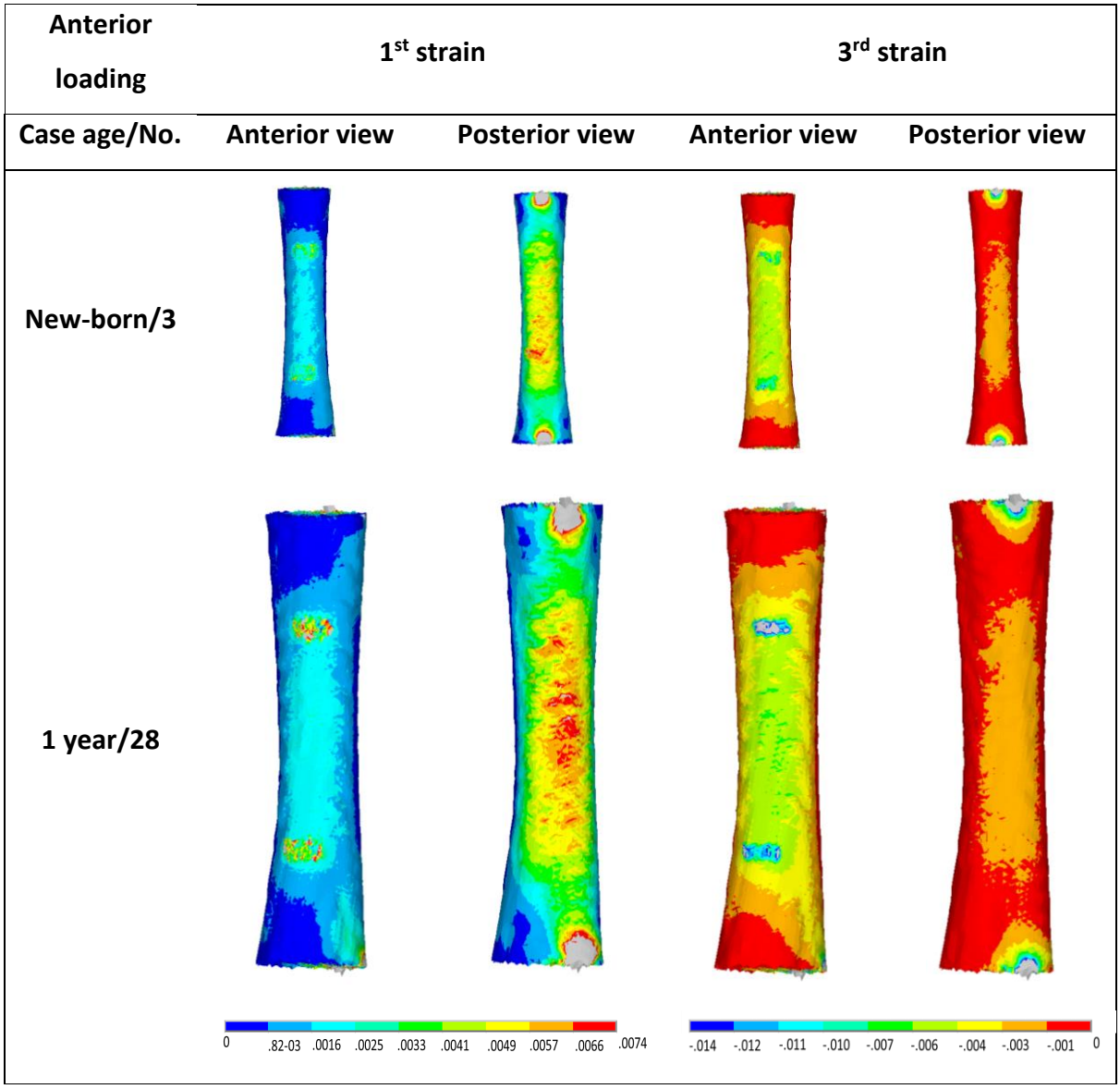

Figure 5.11 Distribution of the first principal strain at the femoral shaft under four-point bending for two different cases. The figure shows the anterior loading direction. When the loads were applied anteriorly, high tensile strains were produced on the posterior side of the femoral shaft. When the load was applied medially, high tensile strains were produced on the lateral side of the femoral shaft.

5.4.2 Failure loads and strain distribution under torsion

The range of the predicted failure moments under external and internal rotations was very similar, at 1-31.4 Nm and 1-30.7 Nm, respectively.

The predicted failure moment increased consistently with age, body mass, cross sectional area and the length of the femur, as shown in Figure 5.12 for external rotation. Since quite similar trends was found for both orientations, only external rotation results are presented in this chapter. All internal rotation figures can be found in Appendix A. The same outlier found in the bending simulation (when the failure moment was plotted in Figure 5.8) was again predicted here. Similar to the bending results, two possible regression relationships, linear and quadratic, were fitted between failure moment and age, body mass, cross-sectional area of the mid-shaft, and the femoral length of each individual in the cohort. As shown in Figure 5.13, for the very young age range (between zero and six months old) a similar trend to that seen in the bending results was observed, where the cross-sectional area correlated best with the failure moment. Age was again not reflected as the best indicator for developmental stages.

The highest strains were observed at either the posterior or lateral side of the femur under internal rotation, while the highest strains were observed at either the anterior or medial side of the femur under external rotation. The distribution of the first principal strain is illustrated in Figure 5.14 for two different cases. Out of the 30 cases, 19 cases had an equal or higher failure moment under external rotation (0% to 21%), while the remain had a higher failure moment under internal rotation (1% to 12 %). The difference is most likely due to geometrical asymmetry (the variance in the shape of the cross-section may cause an additional bending stresses along with torsional stresses).

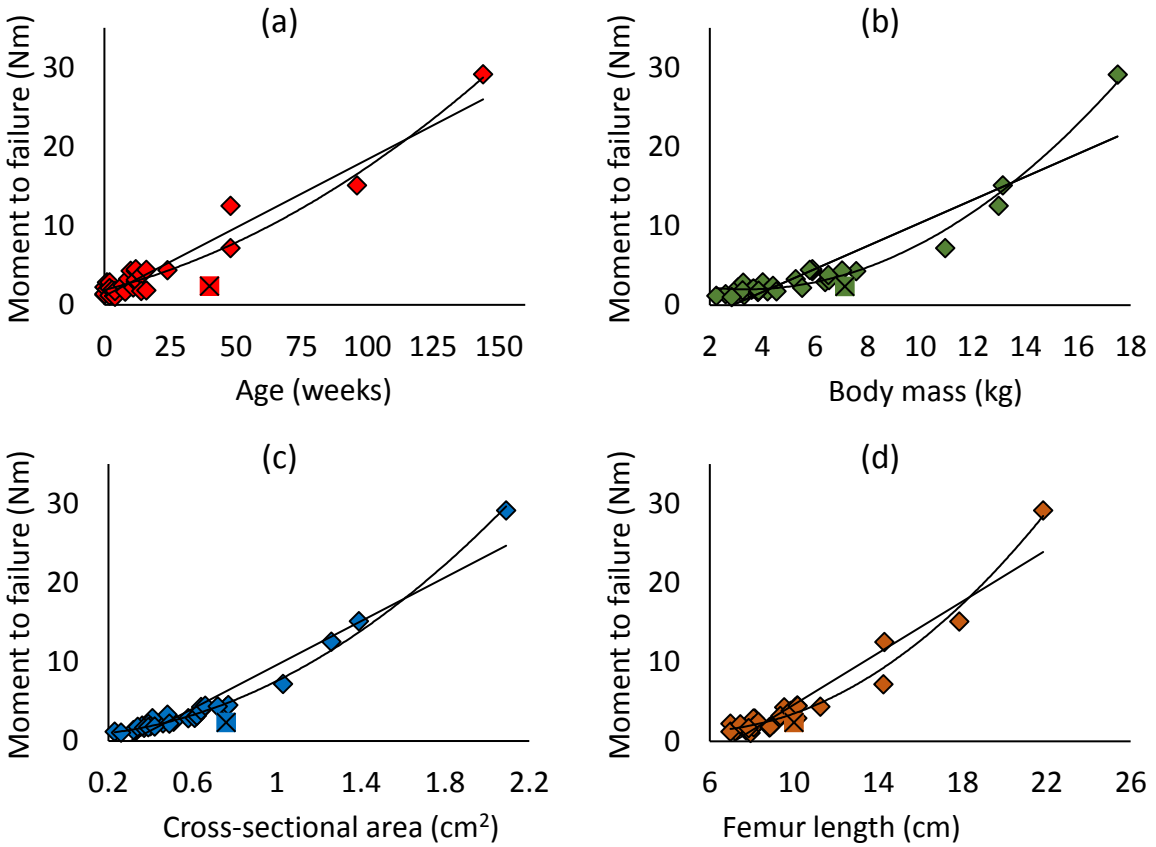

Regression equations:

$M = a \times w + b$

$M = A \times w^2 + B \times w + C$

where M is the moment to failure, w is the body mass or age, parameters a, b, A, B, C are shown below

	Linear regression	R^2	Quadratic regression	R^2
(a) Age	a= 0.173 b= 1.109	0.93	A=0.001 B=0.085 C=1.875	0.90
(b) Body mass	a= 1.454 b=- 4.160	0.84	A=0.131 B=-0.889 C=3.498	0.97
(c) Cross-sectional area	a= 13.822 b=-4.211	0.92	A=6.359 B=0.592 C=0.635	0.99
(d) Femur length	a= 1.626 b=-11.625	0.90	A=0.0985 B=-1.031 C=3.969	0.97

Figure 5.12 Predicted moment to failure under external rotation (Nm) plotted against (a) age, (b) body mass, (c) cross-sectional area and (d) femur length. Two possible regressions were used: linear and quadratic. The outlier (case 26) is indicated with a cross in each graph.

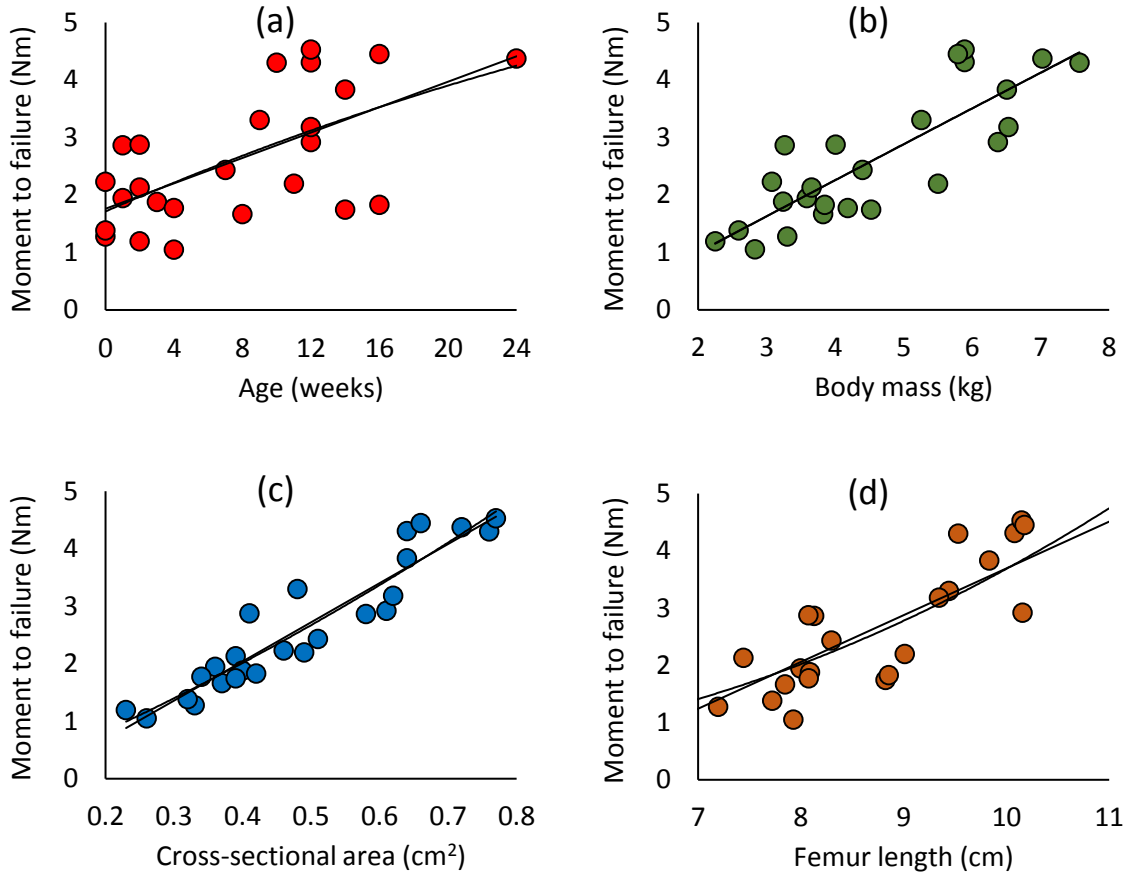

Regression equations:

$M = a \times w + b$

$M = A \times w^2 + B \times w + C$

where M is the moment to failure, w is the body mass or age, parameters a, b, A, B, C are shown below

	Linear regression	R^2	Quadratic regression	R^2
(a) Age	a= 0.111 b= 1.761	0.40	A=0.001 B=0.129 C=1.715	0.40
(b) Body mass	a= 0.625 b=- 0.245	0.70	A=-0.002 B= 0.645 C=-0.289	0.70
(c) Cross-sectional area	a= 6.808 b=-0.684	0.89	A=2.077 B=4.693 C=-0.196	0.89
(d) Femur length	a= 0.817 b=-4.477	0.70	A=0.075 B=- 0.514 C=1.342	0.71

Figure 5.13 Moment to failure (Nm) under external rotation plotted against (a) age, (b) body mass, (c) cross-sectional area and (d) femur length. The plotted data is for ages ranging between zero and six months old to illustrate the trend among very young infants.

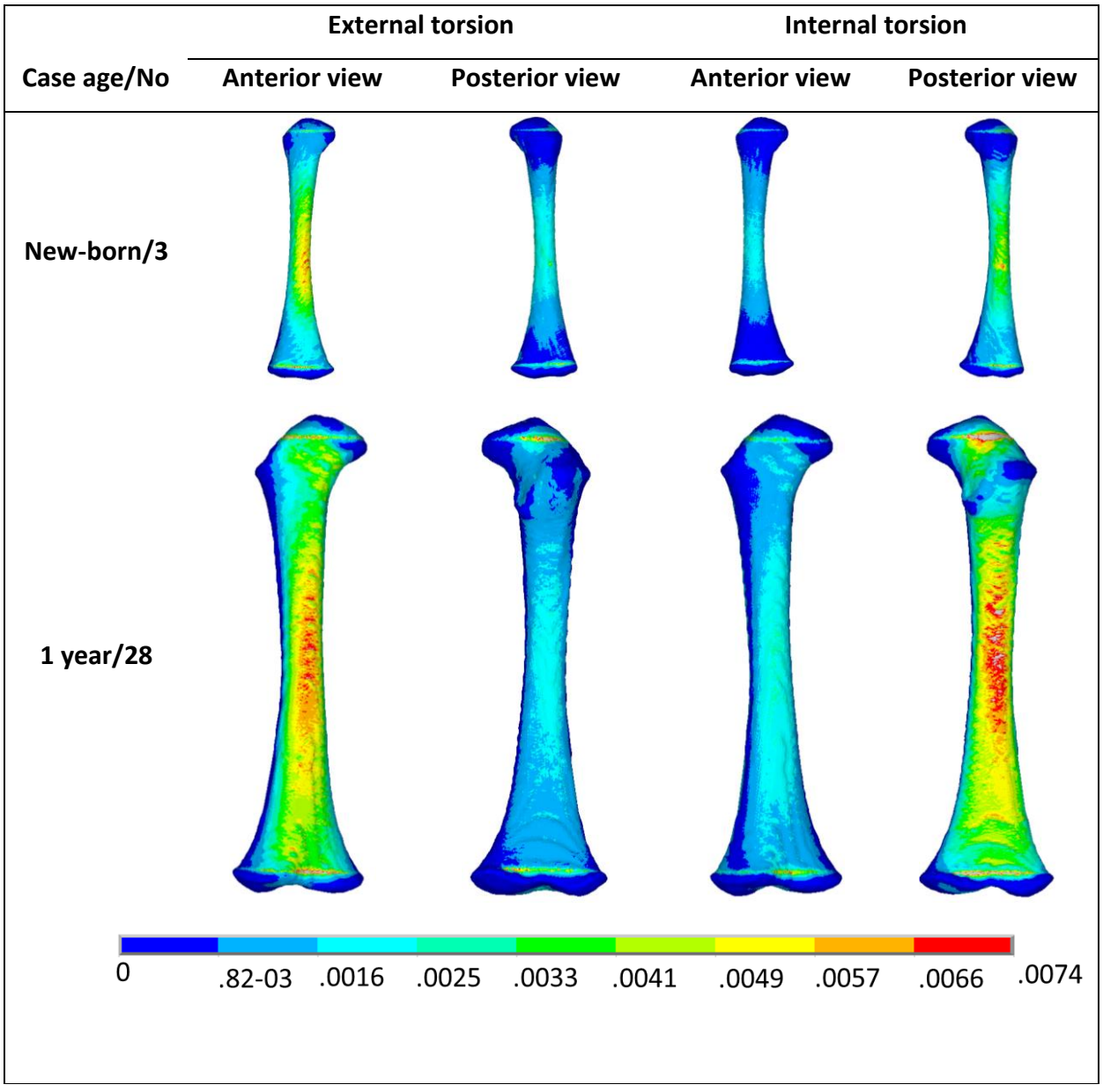

Figure 5.14 Distribution of the first principal strain at the femur shaft under external and internal rotations for two different cases of a new-born and a one year old child.

5.5 Discussion

In this study, CT-based FE analysis has been shown to be a potential tool to study the behaviour of paediatric bones non-invasively. Failure loads of 30 paediatric femora aged from new-born to three years old were estimated under bending and torsional loads. A good agreement was found between the current results and the previous experimental data reported in the literature (Forman et al. 2012; Miltner and Kallieris 1989; Ouyang et al. 2003). The findings added invaluable quantitative data of femora strength to the scarce literature to date.

Femur size with respect to both length and cross-sectional area increased with age/mass (as shown in Table 5.1). This increase in size is expected to result in an increase in the bending and torsional strengths, as indicated by the results. The correlations between the estimated strength and each of the age, body mass and cross-sectional area parameters were investigated, with the best correlation being found to be the body mass. The results also suggested that age is not a good indicator of bone development, and hence the previous experimental results in the literature (reported against age) may not reflect the true skeletal age of the child.

Moment to failure was best correlated with cross-sectional area than the other tested parameters (age, body mass, and femur length), especially for the very young age group range (younger than six months old). This is expected since the shape of the cross-section of the femur mid shaft of very young children is very rounded (close to a perfect circle), making it almost a perfect cylinder. According to the theory of mechanics for a perfect cylinder, there should be a consistent correlation between the bending moment and the cross-sectional area (R^2=1), which is confirmed by the good correlation found in the current study. This can be further investigated in the future by comparing the FE results with the theoretical results using a simple beam theory.

Although the current results showed a faster increase in bone strength after one year old, the small number of cases available beyond one year mean that more cases are needed to confirm this finding. It is well known that bone adapts its mechanical properties according to the external loads. One could postulate that a sudden increase in mobility between one and

two years old (cruising, toddling, walking) may have a strong influence on bone growth and adaptation.

One of the limitations in the paediatric FE models of this thesis is the density-elasticity relationships used (Morgan et al., 2003; Schileo et al., 2008a), which have been derived from experiments conducted on various adults' bone (vertebra, humerus, tibia, and femur), but not paediatric. Since some of the bone material properties change with age, the expected behaviour of children's bone may be different from adults' bone. Consequently, the parameters of the derived density-elasticity relationships could be different. For example, children's bones are on average softer than adults' bones; hence Morgan's parameters (modulus of elasticity-density relationship) may need to be reduced. One would also need to re-evaluate if the exponential trend still fits children's data. However, Öhman et al. (2011) did find a high coefficients of determination for the regression between modulus of elasticity and density ($R^2 = 0.86$, $p<0.001$) of bone samples between 4 and 61 years, indicating the modulus of elasticity-density relationship defined in adults is likely to stay valid for children. This however, cannot be confirmed for very young children (0 to 3 years old) studied here due to the lack of data. It clearly indicates that experiments on paediatric bone sample are needed in the future to more accurately define the density-elasticity relationships for this age group.

The predicted failure moment under bending increased steadily with the increase in age and body mass. The predicted trend was in a good agreement with the previous experimental results found in the literature, as shown in Figure 5.10 (Forman et al. 2012; Ouyang et al. 2003). Furthermore, the range of the fracture moment (0.85-27.9 Nm) predicted by the current FE model was comparable to those reported by Ouyang et al. (2003) and Forman et al. (2012). It is important to mention, however, that the bending moments stated in these two studies were measured under a three-point bending test, which is more likely to produce higher strength than four-point bending. As has been discussed earlier, only three cases in Ouyang et al. (2003) cohort fell within the age range of the current cohort, at 2, 2.5 and 3 years, respectively. Those cases were reported with fracture moments of 29.6, 24.3 and 39.6 Nm, respectively. Similarly, three cases of Forman et al. (2012) were within the age range of the current cohort, one case at 1.33 years old and two cases at 2 years old, with fracture moments of 61.4, 61.7 and 65.5 Nm, respectively. It is clear that the fracture moments reported by Forman's study are noticeably higher than Ouyang's study; possibly because they

used a much faster loading rate (1.5 m/s compared with 0.008 m/s in Ouyang's study). Another reason could be the ethnicity difference. Ouyang's study was conducted on a Chinese population, compared to the Spanish population used in Forman's study.

Due to the complete lack of studies on children younger than one year old, it is difficult to provide a direct comparison for this age range. The only study including this age range was by Miltner and Kallieris (1989), who reported three-point bending tests on 28 children from one day to six years old. Eighteen specimens were tested under quasi-static loadings, while dynamic loadings were used for the remaining cases. They reported a range of fracture moment from 7.05 Nm (six days child) to 109.5 Nm (six years). The study was performed on the entire lower limb, however, including all bones and surrounding soft tissues. It has been suggested previously that soft tissue may absorb some of the energy during loading (Kerrigan et al. 2003); therefore, these results need to be interpreted with caution.

For torsional loads, there is no previous paediatric study reported in the literature. Consistent failure moment estimations were found by comparing the results of the torsional and bending scenarios in this study, however. Both results showed a comparable trend in respect to age/mass and the range of predicted moments to failure. Furthermore, in agreement with the previous experimental studies of long bones under pure torsional loads (Kress et al. 1995; Theobald et al. 2012), this study also predicted the maximum principal strain to lie at the narrowest cross-sectional area of the diaphysis.

The findings of the current study suggest that the CT/FE analysis that has hitherto been extensively and effectively used in adults can be adapted and applied to children. Since obtaining paediatric bone samples is difficult, using non-invasive techniques such as CT/FE models offers valuable information on paediatric bone biomechanics.

6 SPONTANEOUS HUMERAL FRACTURES IN INFANTS (STUDY II)

6.1 Introduction

Humeral fractures under the influence of external forces in infants at the age of rolling have been previously reported as a possible accidental mechanism by Hymel and Jenny (1996). They proposed that a humeral fracture might occur when an infant rolled from prone to supine aided by another person. Hymel and Jenny (1996) reported two cases of humeral fractures. Case 1 was a five month old boy, and case 2 was a three month old girl. The injury event was videotaped in case 1. The video showed the child lying prone, with an arm extended away from the body. A fracture sound was heard when the child was rolled by his two year old sister to the supine position. According to the medical record, the child was documented with an oblique spiral fracture of the humeral diaphysis. After a review of the videotape and family evaluation by a multidisciplinary team, the injury was considered to be unintentional. In case 2, the injury was described by the father using a doll in a videotape, when the father was helping his daughter to roll to her back (supine position), her arm trapped under her back and then the fracture occurred. An oblique spiral fracture of the humerus diaphysis was also reported in this case. By reviewing the videotape of the father demonstrating the event, multidisciplinary reviewers concluded that the father did not intentionally cause the injury.

In a recent study in 2014, a study reported seven cases of humeral fracture, described as “non-accidental injuries”, based on the Hymel mechanism (Somers et al., 2014). These cases were aged between four and seven months old. According to the description of the caretakers, all cases were reported as spontaneous humerus fractures where the babies were rolling over on their own. Unlike the Hymel report, however, there was no external force acting on the body during the roll. Furthermore, there was no video evidence or witness available to ascertain the injury mechanism. It should also be noted that their study included cases of children rolling in both directions (prone to supine and supine to prone), whereas neither of the Hymel cases was rolling from supine to prone position. The study of Somers and his colleagues has therefore fuelled debate in the clinical community. It has been urged that the belief that non-ambulant children are able spontaneously to fracture a long bone

without the intervention of an external party could be inappropriate (Jenny, 2014; Rosado, 2014).

The aim of study II is therefore to investigate the possibility of a spontaneous humeral fracture of infants while rolling from prone to supine using a CT-based FE modelling approach. This chapter will present the modelling procedure used to develop the CT/FE model. These include the applied boundary conditions, the method used to calculate the loads acting on the humerus during the rolling manoeuvre, and the simulation of various possible positions of the arm with respect to the body. The results of this study in terms of the predicted strain values and locations are reported and discussed towards the end of the chapter.

6.2 Modelling approach for the paediatric humerus

6.2.1 Boundary conditions of the FE humerus model

According to the hypothesis described by Hymel (Hymel and Jenny, 1996), the hand of the infant could be trapped underneath the trunk. Figure 6.1 shows a schematic drawing of three stages during the manoeuvre from prone to supine. In position (a), the infant is lying on the abdomen (or prone position). The infant then uses one arm to push against his/her body weight and start to roll. At the intermediate position (b), the infant's trunk is perpendicular to the floor, where the hand could be trapped between the body and the floor. Because of the minimal strength of the abdominal muscles of very young infants, flipping back to the starting position may be difficult. The infant will therefore continue to roll to position (c) at this point, and because of the limited movement of the shoulder-scapula joint, the hand will be fixed behind the body, leading to a spontaneous fracture.

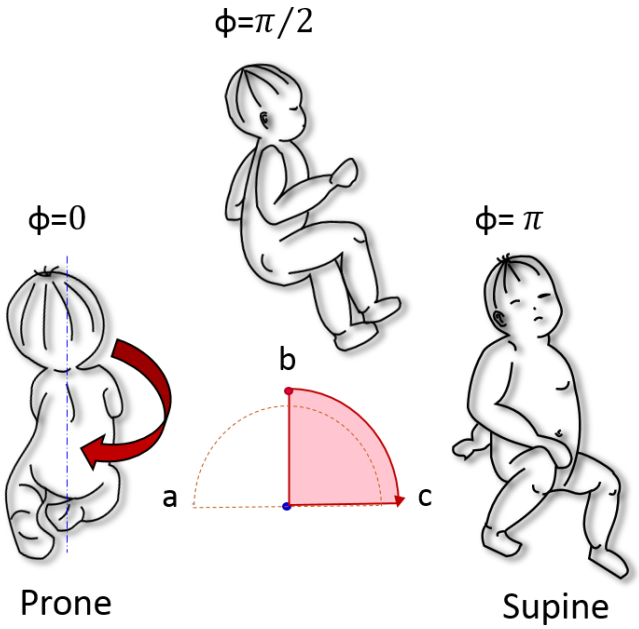

Figure 6.1 Three stages of an infant (approximately 4-7 months) rolling from prone to supine. Position (a) is the starting position (prone) when the infant is lying on his abdomen. Position (b) is when the trunk is perpendicular to the floor. And position (c) is the final potion when the infant is lying on his back (supine).

In this thesis, humerus FE models were created to investigate the validity of this theory. The boundary conditions have been chosen to simulate the case when an infant is rolling from prone to supine with one of his hands trapped behind the body (between the intermediate stage and the final stage shown in Figure 6.1 b & c. Figure 6.2 shows the representative FE model in which the proximal and distal ends of each humerus were connected to pilot nodes using MPC elements. The MPC elements related all the degrees of freedom of nodes at proximal and distal ends to the pilot nodes. Each pilot node was created at the centre of the proximal and distal ossifications. The displacements of the distal pilot node were fixed in the y and z directions and free in the x direction. As the hand was fixed while the body of the child was rotating around the shoulder joint, rotation of the distal pilot node was not allowed around the long axis of the humerus (or x-axis). The other two directions of rotation, around y and z, were not constrained. The displacement of the proximal pilot node was fixed in the x direction to mimic the effect of the shoulder joint (all other degrees of freedom were unconstrained). This boundary condition was chosen in order to minimize the constrained degrees of freedom while avoiding rigid body motion of the model.

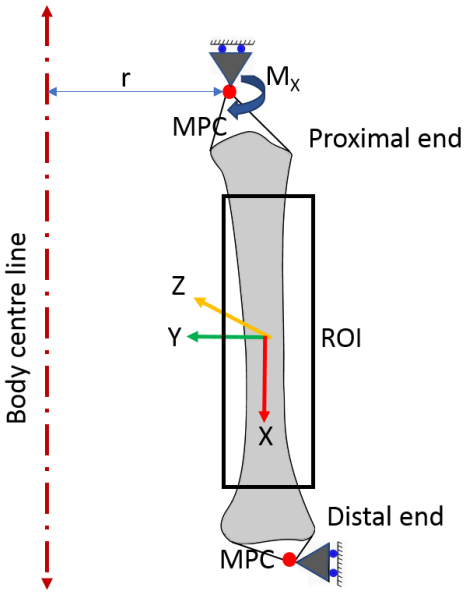

Figure 6.2 Finite element model of the humerus. Proximal and distal ends were connected to the pilot nodes (red nodes) by MPC elements. The pilot nodes were located at the centre of the proximal and distal ossifications. A rotational moment (M_X) was applied at the proximal end representing the rotation around the centre of the shoulder joint. The distance between the body centre line and the proximal ossification centre is the moment arm indicated by r. ROI is the region of interest, highlighted inside the black box.

6.2.2 Loading conditions

The rotational moment was applied at the proximal pilot node around the long axis of the humerus. The value of the applied moment was calculated according to the following equation:

$$M_X = m\, a_t\, r \tag{6.1}$$

Where: M_X is the applied moment at the centre of the proximal ossification. m is the total body mass. r is the moment arm, which is the distance between the proximal ossification centre and the body centre line of the infant. a_t is the tangential acceleration of the body needed to rotate from position b (at which the angular displacement ϕ is equal to $\pi/2$) to position c (ϕ is equal to π).

The tangential acceleration was calculated as shown below:

$$\omega = \frac{\Delta\phi}{\Delta t} \tag{6.2}$$

$$\alpha = \frac{\Delta\omega}{\Delta t} \tag{6.3}$$

$$a_t = r\alpha \tag{6.4}$$

Where: ϕ is the angular displacement, ω is the angular velocity, α is the angular acceleration, and t is the time needed for a child to rotate from position b to position c (Figure 6.3).

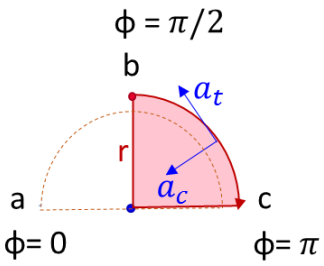

Figure 6.3 Schematic showing angular displacements (ϕ) at position a, b, and c of the rolling manoeuvre, and the direction of the tangential acceleration.

While it would be reasonable to assume that the entire body mass will not necessarily contribute to the rotation, using the total body mass will provide us with an upper bound value that represents the "worst-case scenario". A more accurate estimation of the effective mass during this manoeuvre could be found in the future by developing a total body dynamic model.

By reviewing a number of representative videos[5,6] of infants rolling from prone to supine, the range of time needed for an infant to roll from position b to c was estimated to be between 0.3 and 0.7 seconds. To account for the worst-case scenario, the lower bound value of 0.3 s was used.

For all three cases, r values have been estimated using two different methods in order to check for repeatability. Three landmarks were created: the left and right proximal ossification centres, and the centre of the manubrium of the sternum, as shown in Figure 6.4. In the first method, r was calculated as half the distance between the left and right proximal ossification landmarks. In the second method, r was calculated as the distance between the left proximal ossification landmarks and the manubrium landmarks. Both methods produced very similar results with a difference of less than 0.7%. The *r* values estimated from the first method are

[5]. https://www.youtube.com/watch?v=bbBH5o3Lni8
[6]. https://www.youtube.com/watch?v=ObHsHlBLP20

therefore used here. All parameters used to find the applied moment for each case are listed in Table 6.1.

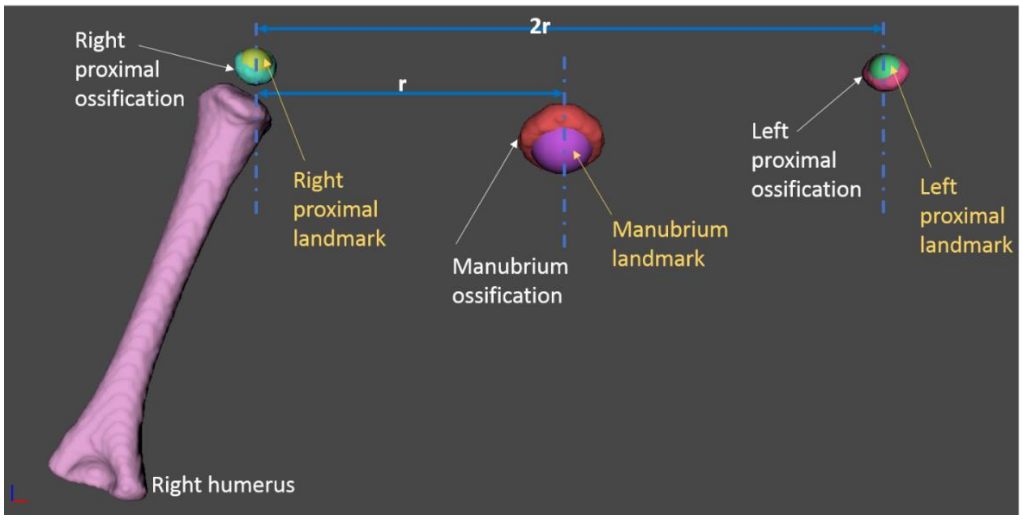

Figure 6.4 Illustration of the landmarks for the two methods used to estimate the moment arm r. White text highlights areas segmented from the CT scans. Yellow text highlights the landmarks determined via virtual palpation. The first method estimated r as half the distance between the right and left proximal ossification landmarks. The second method estimated r by finding the distance between the right proximal landmark and the manubrium landmark.

Table 6.1 Variables used in the finite element model of the humerus for the three cases.

Case No.	Body mass (kg)	Angular displacement (rad)	Time (sec)	Moment arm (r) (mm)	Tangential acceleration (a_t) (m/s^2)	Applied moment (M_x) (Nm)
1	3.85	$\pi/2$	0.3	47.49	0.83	0.15
2	5.79	$\pi/2$	0.3	66.22	1.15	0.44
3	7.03	$\pi/2$	0.3	67.20	1.17	0.55

During the rolling manoeuvre, and when the body is directly on top of the hand, the hand position could be at different angles with respect to the trunk. Because of the complexity of the shoulder-scapula joint, however, the motion of the hand is limited in this position. The maximum angle through which the hand could move towards the back of the body is 45 degrees in horizontal extension and 60 degrees in vertical extension for adults (Resnick, 2004). Assuming a similar range for very young children, these values were assigned in the simulation as the maximum angles by which the hand could reach behind the body. Sixteen

orientations were therefore simulated by incrementing the angle by 15 degrees and 20 degrees in horizontal and vertical extensions, respectively, as shown in Figure 6.5.

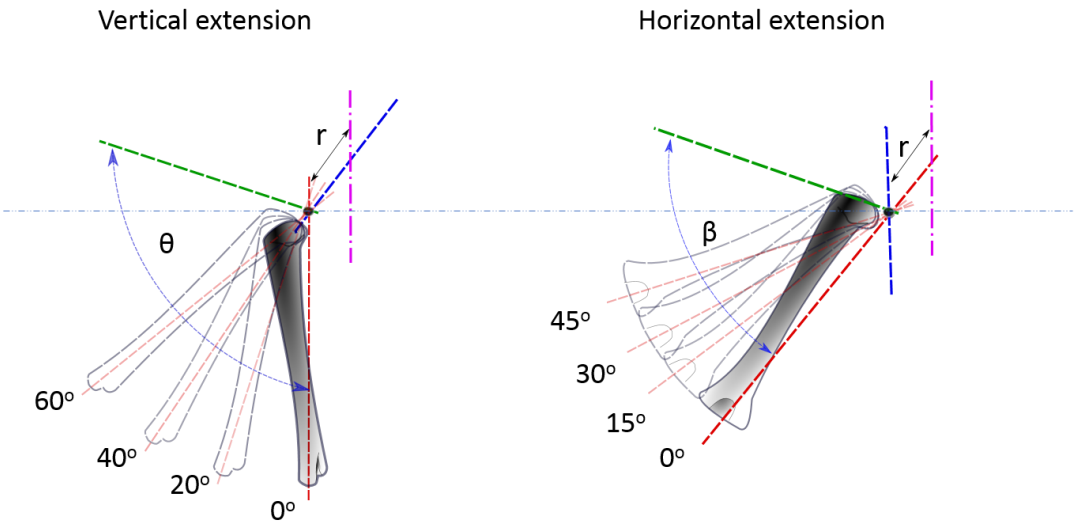

Figure 6.5 Sixteen simulated orientations of the humerus finite element model. The horizontal angle was incremented by 15 degrees while the vertical angle was incremented by 20 degrees.

6.2.3 Sensitivity analyses of the mesh

The mesh convergence analysis was performed using six different element sizes: 0.5, 0.6, 0.7, 1, 1.2, and 1.5 mm. The peak first and third principal strains, e1 and e3, were analysed with respect to the element size. Figure 6.6 shows the convergence of one of the three cases (case 3). Convergence was achieved when the differences in peak e1 and e3, between the converged mesh (508,626 DOFs for 1 mm element size) and the finest mesh (3,924,369 DOFs for 0.5 mm element size), were below 6%. These differences were found to be the same for the other two cases.

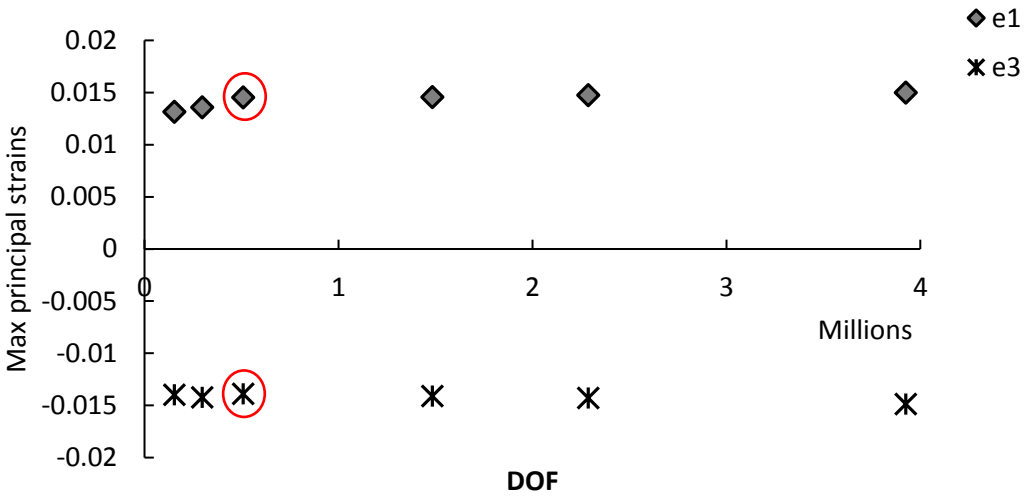

Figure 6.6 Convergence analysis of the mesh Ffor case 3 (six month old). The peak first and third principal strains (maximum e1 and minimum e3, respectively) were plotted against the number of degrees of freedom of the mesh. Six different element sizes were used to evaluate the required level of mesh refinement. The converged mesh is highlighted in the red circle.

6.2.4 Post-processing of the principal strains

Both the first and third principal strains were evaluated for all the nodes within the region of interest (ROI), which is highlighted by the black rectangle in Figure 6.2. The peak principal strains were extracted from the FE models under each of the 16 simulated orientations. Among these, the maximum and minimum predicted stains were found and compared with the tensile and compressive elastic limits of human bone, as mentioned in Chapter 5 (Section 5.2.4).

6.3 Results

6.3.1 Morphological parameters of the paediatric humerus

The length of the humerus and the maximum modulus of elasticity for each case are listed in Table 6.2. The length of the humerus was measured as the distance between the proximal and distal ossification centres. The length of the humerus of case 2, who was a four month old child, was quite similar to case 3, who was a seven month old child, while case 1 was the shortest among the three cases. This indicated that there are some variation in humerus development within a certain age range.

The listed modulus of elasticity represents the peak value estimated from the measured Hounsfield Units of the CT scans. The distribution of the modulus of elasticity of the three cases is shown in Figure 6.7. Case 2 generally had a higher modulus of elastisity across the humerus in comparison with the other two cases. As shown in table Table 5.1 (numbered as case 24), this case has a comparably lower percentile in body mass but a higher percentile in height, indicating this could be a relatively tall and slim child. However, there is no direct evidence to indicate the reason behind the higher modulus of elasticity.

Table 6.2 Demographics for the cohort of the current study (a subset of the cohort used in study I). Humerus length was estimated from the CT scans, calculated as the distance between the proximal and the distal ossification centres. The peak modulus of elasticity was estimated from the measured Hounsfield Units of the CT scans.

Case No.	Gender	Age (Weeks)	L (cm)	E_X (GPa)
1	M	16	8.45	10.66
2	F	16	9.32	15.15
3	M	24	9.96	13.26

M: male; F: female
L: Humerus length
r: Moment arm
t: Duration of rolling
E_x: Peak modulus of elasticity

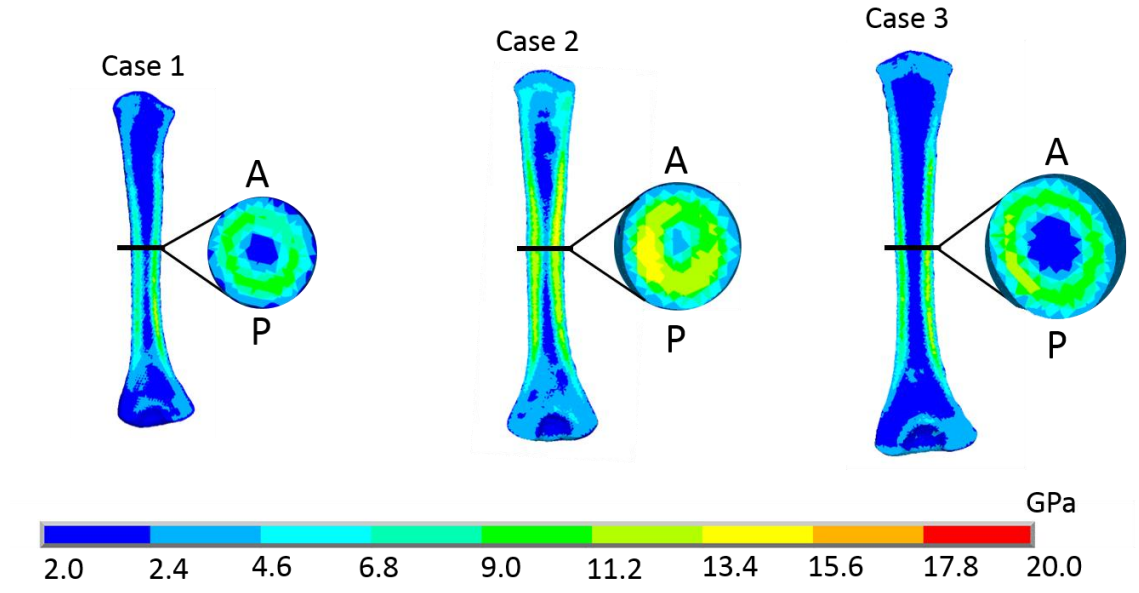

Figure 6.7 Distribution of the modulus of elasticity over the humerus shown in the frontal and transverse planes for the three selected cases. A, anterior; P, posterior.

Although two of the three cases were at the same age (four months old), the moment needed for the rolling manoeuvre in case 2 was much higher (66%) than in case 1. This could be due

to the fact that case 2 was a much bigger and taller child than case 1, with a 33% higher body mass and a 28% higher moment arm.

6.3.2 Maximum strains predicted under various orientations of the humerus

The highest predicted first and third principal strains among all simulated orientations was consistently less than the elastic tensile and compressive strain limits of adult human bone (Bayraktar et al., 2004). The difference between the highest first principle strain and the tensile strain limit was 85% for cases 1 and 2, and 81% for case 3, while the differences between the lowest third principal strain and compressive elastic limit was 88%, 90% and 86% for cases 1, 2 and 3, respectively.

Figure 6.8, Figure 6.9, and Figure 6.10 show the predicted maximum first principal strains of the humerus for the three cases under each orientation (refer to Figure 6.5 in Section 6.2.2 for the simulated orientations). The differences between the predicted peak first principal strain among all 16 orientations (or positions of the humerus with respect to the trunk) were 27%, 28% and 19% for cases 1, 2, and 3, respectively. The highest first principal strain values were found when the humerus was located at the extreme angles relative to the body for all three cases. For cases 2 and 3, the highest first principal strains were predicted at an angle of 60^{o} vertical extension and 0^{o} horizontal extension of the arm behind the body. For case 1, the highest first principal strain was predicted at an angle of 45^{o} horizontal extension and 0^{o} vertical extension of the arm behind the body.

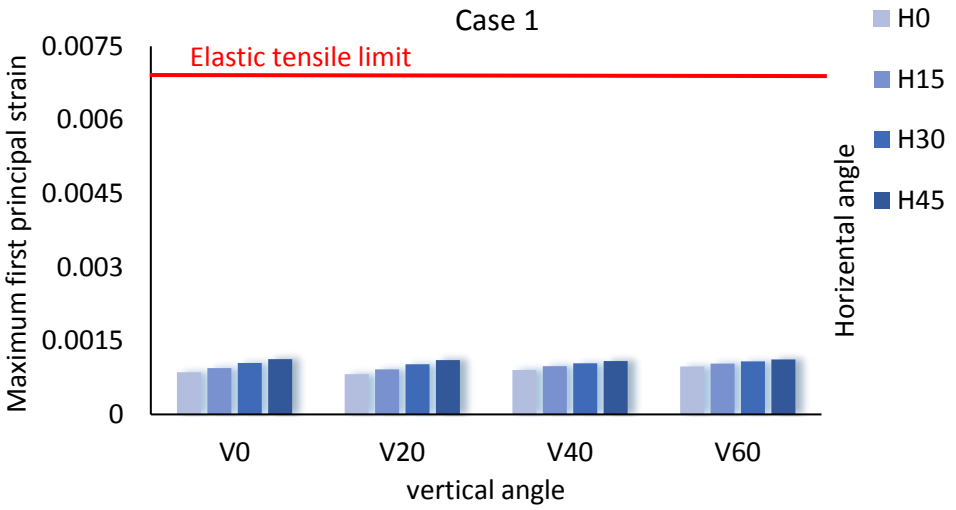

Figure 6.8 Maximum first principal strains under various orientations of the humerus for case 1 (four months old). Sixteen different positions of the humerus (with respect to the body) were simulated. Vertical extension angles ranged from 0^{o} to 60^{o}, with a 20^{o} increment, while horizontal extension angles ranged from 0^{o} to 45^{0}, with a 15^{o} increment. V represents the vertical extension angle, and H represents the horizontal extension angle.

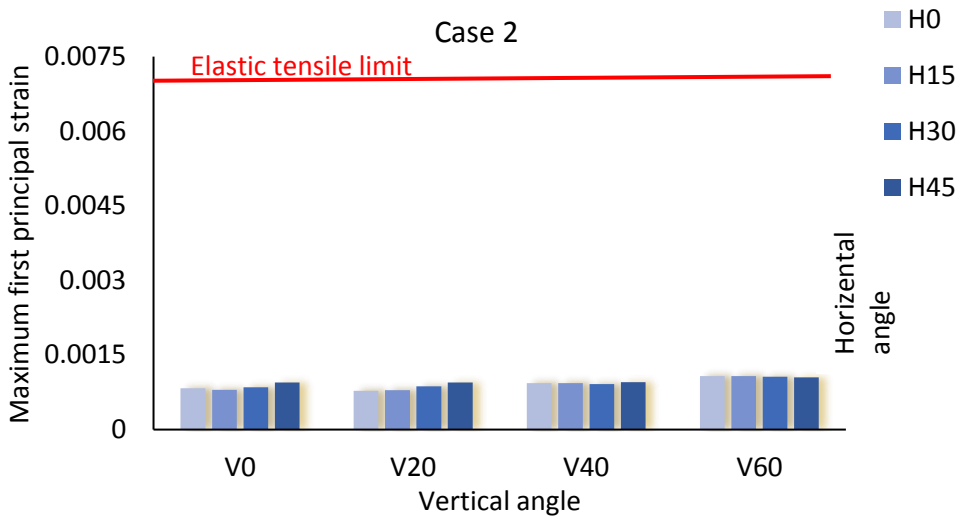

Figure 6.9 Maximum first principle strains under various orientations of the humerus for case 2 (four months old). Sixteen different positions of the humerus in respect to the body were simulated. Vertical extension angles ranged from 0^{o} to 60^{o}, with a 20^{o} increment, while horizontal extension angles ranged from 0^{o} to 45^{0}, with a 15^{o} increment. V represents the vertical extension angle, and H represents the horizontal extension angle.

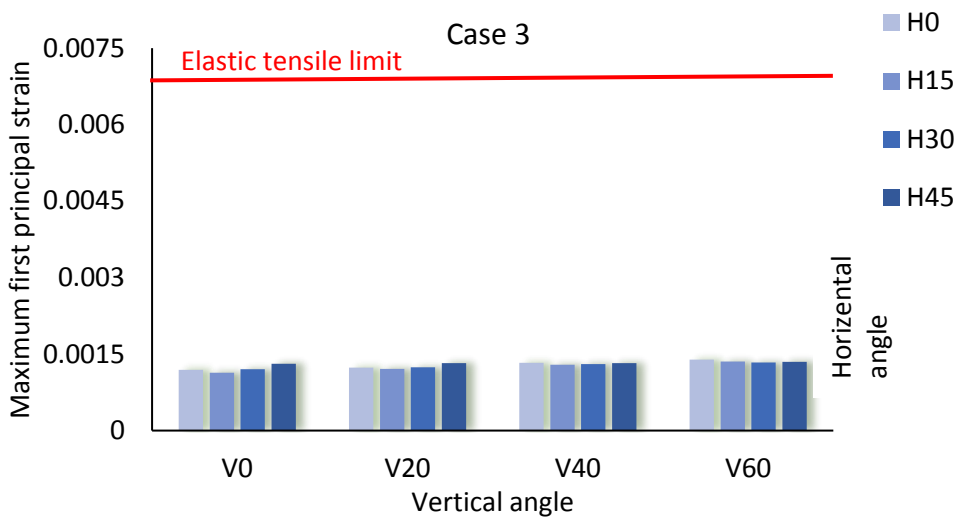

Figure 6.10 Maximum first principle strains under various orientations of the humerus for case 3 (six months old). Sixteen different positions of the humerus in respect to the body were simulated. Vertical extension angles ranged from 0° to 60°, with a 20° increment, while horizontal extension angles ranged from 0° to 45°, with a 15° increment. V represents the vertical extension angle, and H represents the horizontal extension angle.

Figure 6.11, Figure 6.12, and Figure 6.13 show the predicted maximum third principal strains of the humerus for the three cases under each orientation (refer to Figure 6.5 in Section 6.2.2 for the orientations simulated). The differences between the predicted peak third principal strain among the 16 orientations were 30%, 29% and 23% for cases 1, 2 and 3, respectively. Similarly, the highest third principal strain values were also found when the humerus was located at the extreme angles relative to the body for all three cases. For cases 1 and 2, the lowest third principal strains were predicted at an angle of 60° vertical extension and 30° horizontal extension of the arm behind the body. For case 3, the lowest first principal strain was predicted at an angle of 45° horizontal extension and 0° vertical extension of the arm behind the body.

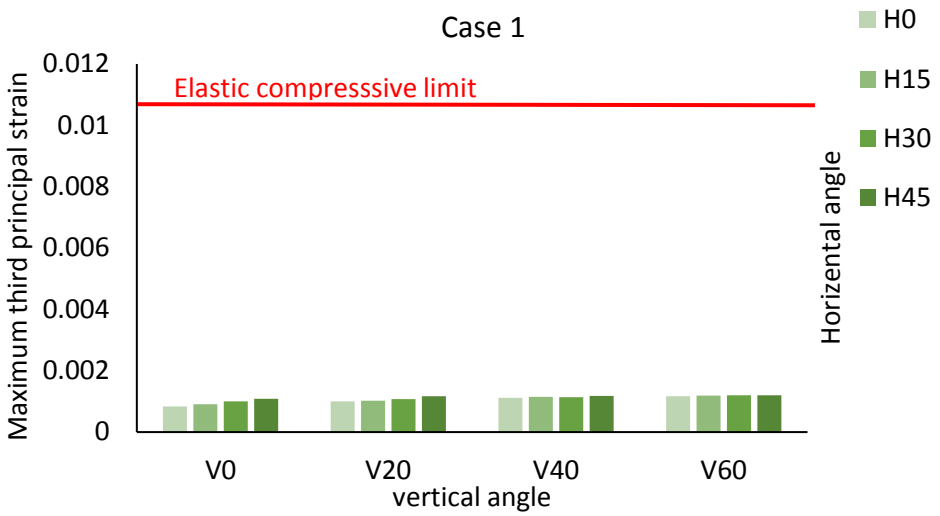

Figure 6.11 Maximum third principle strains under various orientations of the humerus for case 1 (four months old). Sixteen different positions of the humerus in respect to the body were simulated. Vertical extension angles ranged from 0^o to 60^o, with a 20^o increment, while horizontal extension angles ranged from 0^o to 45^0, with a 15^o increment. V represents the vertical extension angle, and H represents the horizontal extension angle.

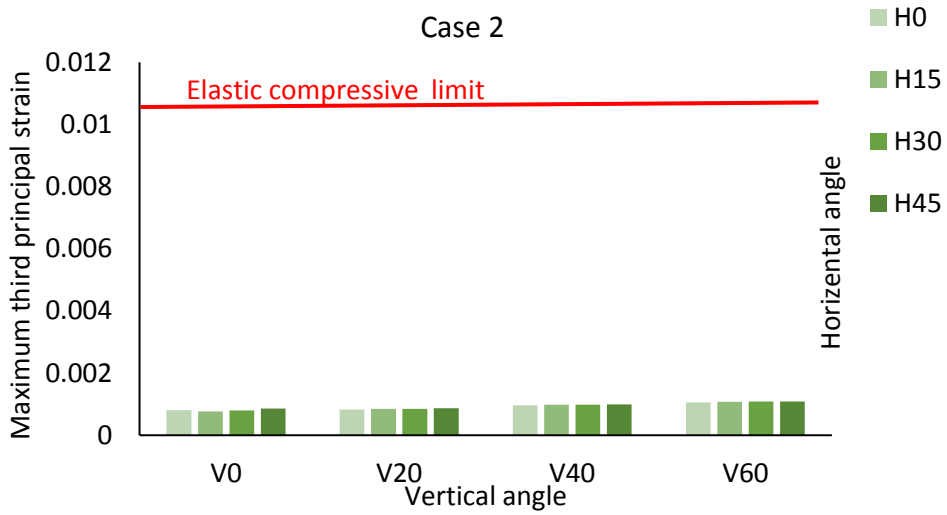

Figure 6.12 Maximum third principle strains under various orientations of the humerus for case 2 (four months old). Sixteen different positions of the humerus in respect to the body were simulated. Vertical extension angles ranged from 0^o to 60^o, with a 20^o increment, while horizontal extension angles ranged from 0^o to 45^0, with a 15^o increment. V represents the vertical extension angle, and H represents the horizontal extension angle.

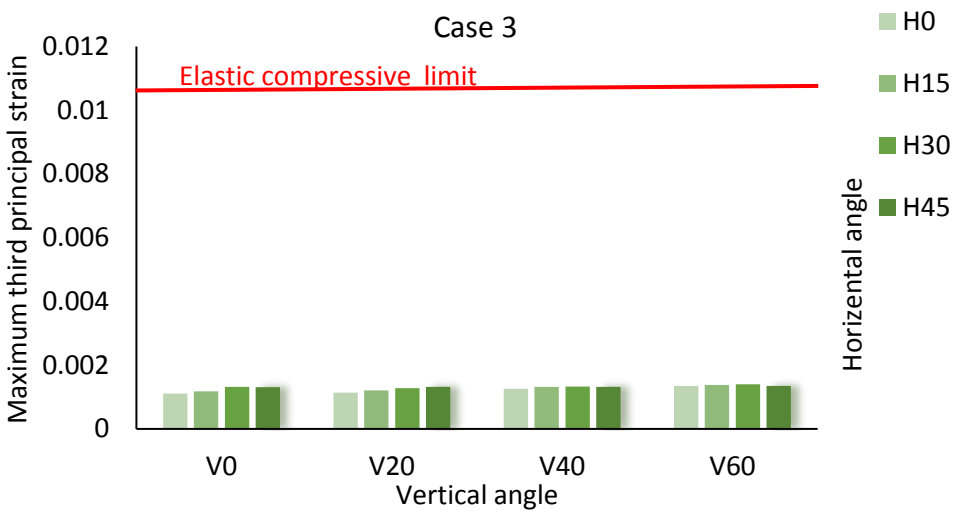

Figure 6.13 Maximum third principle strains under various orientations of the humerus for case 3 (six months old). Sixteen different positions of the humerus in respect to the body were simulated. Vertical extension angles ranged from 0° to 60°, with a 20° increment, while horizontal extension angles ranged from 0° to 45°, with a 15° increment. V represents the vertical extension angle, and H represents the horizontal extension angle.

6.3.3 Strain distribution

Table 6.2 shows the distribution of the first principal strains of the three cases under four selected angles for the 16 simulated humerus positions. These are: (a) neutral position, (b) extreme angle of the horizontal extension at 45° (with 0° in vertical extension), (c) extreme angle of the vertical extension at 60° (with 0° in horizontal extension), and (d) a combination of both extreme angles. The highest strains were located at the medial side of the humerus shaft when the arm was in the neutral position (case a, e.g. the body is directly on top of the left arm). This moved to the lateral side of the shaft when the arm was extended horizontally in case b. In both cases c and d, the highest strains were found at the anterior side of the humerus.

Table 6.2 Distribution of the first principal strains over the humerus for cases 1, 2 and 3. Four selected orientations are illustrated: (a) neutral position, (b) 45° horizontal extension with 0° vertical extension, (c) 60° vertical extension with 0° horizontal extension, and (d) a combination of both extreme angles. H: Horizontal angle; V: Vertical angle.

		Medial view	Lateral view	Anterior view	Posterior view
Case 1	**a**	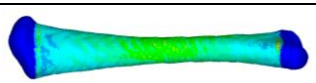	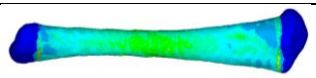	**c**		
	b		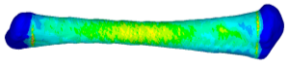	**d**	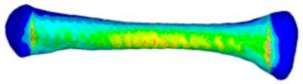	
Case 2	**a**	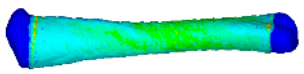		**c**	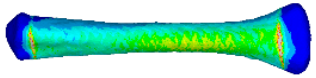	
	b	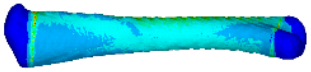	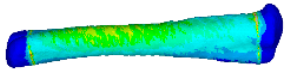	**d**	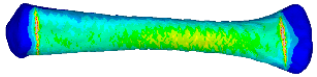	
Case 3	**a**	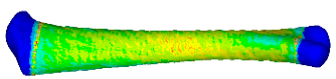		**c**		
	b		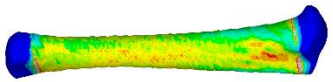	**d**	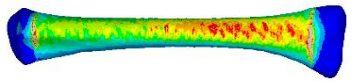	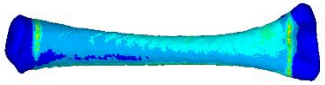
		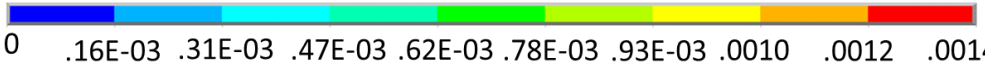			

6.4 Discussion

The aim of this study was to investigate the likelihood of an infant spontaneously fracturing the humerus while rolling from prone to supine using a CT/FE modelling approach.

The results of the of the three simulated cases showed that the highest predicted strains were substantially lower (with a difference of more than 80%) than the elastic limit of human bone. This suggests that it is highly unlikely for an infant to break their humerus while rolling over to the back without an external force. The results therefore support the arguments of Jenny (2014) and Rosado (2014). Rosado pointed that it is very doubtful that an infant who can hardly carry his/her own body weight against gravity, can have sufficient strength to overcome failure limit of the humerus. Jenny, however, claimed that it is difficult to draw a clear conclusion on the likelihood of spontaneous humeral fracture during rolling because the range of bone strength of healthy infants is as yet unknown, as there is not sufficient data on the injury tolerance of infants.

The highest strains were predicted at either the middle or towards the distal end of the humeral diaphysis. This means a fracture could initiate at these locations if the bone was to fail under the predicted loads in this study. The cases reported in Hymel and Jenny (1996) both had oblique spiral humeral fractures of the diaphysis, which is similar to the location of the highest strains predicted by the current models.

Unsurprisingly, the lowest strains were predicted under the neutral orientation of the humerus for all three cases, whereas the highest strains were all predicted under the extreme angles (either vertical or horizontal extensions or a combination of the two angles). This suggested that bending or extending the arm towards the physical limit would put substantial strains on the body. Although the current model suggested that the value was not high enough to fracture the bone spontaneously, it would be possible for fracture to occur with a sufficiently high external force (as reported by Hymel and Jenny). Furthermore, these high strains may damage the surrounding soft tissues and joints. This evidence suggests that parents or caretakers should be made aware of the potential consequence of extreme manoeuvring of infants' limbs during a wide range of daily activities, from changing nappies to exercising with young children, so that caution can be taken to avoid injuries.

In the current study, the maximum angle through which the child's hand can move towards the back of the body was assumed to be in a similar range as adults: 45 degrees in horizontal extension and 60 degrees in vertical extension (Resnick, 2004). This may not be appropriate since children are usually more flexible than adults. The current results showed that the predicted strain values increase by 30% when the angle reaches the extreme limit with no more than a 10% increase with each increment. Even if we considered an extension angle of 90 degrees (which is highly unlikely as a distortion of the shoulder joint might occur), the predicted strains would still be far from reaching the elastic limit.

The results of this study showed that it is highly unlikely for the bone to fracture spontaneously, given the current underlying modelling assumptions. In order to confirm this finding, further investigations are required, in order to include more cases with more accurate boundary conditions established for the rolling manoeuvre. These will be further discussed in Chapter 8.

7 STRENGTH OF THE PROXIMAL FEMUR UNDER SIDE FALL LOADING CONDITIONS (STUDY III)

7.1 Introduction

Osteoporotic hip fractures in elderly people are a major public health burden and commonly occur as a result of fall. In the last few years, the estimation of femoral bone strength by finite element (FE) models has been recognized as a feasible alternative tool to areal bone mineral density (aBMD). The accuracy of the FE model as a strength predictor is yet to be confirmed when compared against the current clinical standard. Previous studies have showed that FE models can predict the strength of a cadaver femur, as measured experimentally, with excellent accuracy (Pottecher et al., 2016), but this level of high accuracy was only reported for models that strictly replicate the experiments. When the predicted FE strength was used to classify patients according to their risk of fracture, however, the accuracy is more questionable (Keyak et al., 2011; Kopperdahl et al., 2014; Nishiyama et al., 2014; Orwoll et al., 2009). It is not clear how much effect the displacement boundary conditions used in the FE models and/or the range of the simulated loading conditions have on the classification power of the FE (separate fracture and non-fracture cases). Although the effect of the variance in the boundary conditions on the prediction of the femur strength has been investigated before (Rossman et al., 2015), their effects on the classification accuracy have not been reported.

In addition, in term of fracture type prediction, the majority of FE models simulating sideways falls have predicted only neck fractures (NF) (Bessho et al. 2009; de Bakker et al. 2009; Haider et al. 2013) and inter-trochanteric fractures (ITF) (Bessho et al., 2009; de Bakker et al., 2009; Ford et al., 1996), whereas the per-trochanteric fracture pattern has rarely been modelled, despite being observed in clinical practice (AO Fundation, 2018). This suggests that the boundary constraints employed in past studies may not be completely representative of the actual physical event.

Under a side fall configuration, it has been shown that posterolateral falls are associated with the weakest structural orientation of the femur (an orientation at which the strength of the proximal femur is at minimum) compared to anterolateral falls (Ford et al. 1996; Majumder

et al. 2009; Pinilla et al. 1996). Based on this, previous studies have investigated the ability of the FE model to associate bone strength with fracture risk under posterolateral fall conditions (Falcinelli et al., 2014; Qasim et al., 2016). This is despite the fact that it is impossible to predict the exact fall configuration in which an individual may fall. Falcinelli et al. (2014) reported an AUC (area under the receiver operating characteristic curve) equal to 0.88, for a cohort of European women (22 fracture and 33 control cases). On the other hand, Qasim et al. (2016) reported an AUC= 0.79 for a cohort of 98 Caucasian women with 49 control and 49 fracture cases. Both studies considered multiple loading directions that represent a posterolateral fall only. There is only one study in the literature that has considered posterolateral and anterolateral falls while investigating the ability of FE to classify patients according to the risk of fracture (Nishiyama et al., 2014). The study was conducted on a cohort of Japanese women (35 fracture and 35 control cases). Nishiyama et al. (2014) reported a higher accuracy (AUC=0.94) than that reported by either Falcinelli or Qasim. Each of these three studies was conducted on a different sample size and a different population, however. Ethnicity might also play a role in the results, since the fracture rate of Asian populations has been found to be half of that of Caucasian populations (Ross et al., 1991). Hence it is important to understand whether considering both anterolateral and posterolateral falls can improve the ability of the FE model to stratify patient according to their risk of fracture.

The aim of this study is therefore twofold:

1. To investigate the effect of variation in the displacement boundary condition on the predictions returned by the FE model in terms of: (a) the stratification power of the FE model for patients according to their risk of fracture; and (b) the prediction of fracture type, in particular, per-trochanteric fracture. These results have not been reported in previous FE studies, according to author's knowledge.
2. To explore the ability of the FE model to more accurately stratify patients according to their risk of fracture by considering (a) posterolateral falls alone; and (b) both anterolateral and posterolateral falls.

This chapter will present the modelling approach of side fall configurations modelled with various boundary conditions, and present the results of the study in order to answer the questions raised above.

7.2 Modelling approach for sideways fall in adults

As discussed in Section 3.5.2.1, a literature review was carried out in order to identify the most common boundary conditions (BCs) used to represent the side fall configuration in the finite element models. Most of these models applied a range of different linear BCs via direct constraints. We categorized the BCs into three types as listed in Table 7.1 and shown in Figure 7.1. In order to gain a better understanding of these BCs, we tested them on five random cases of the control group. Type A was used in this thesis to represent a linear boundary condition and is referred to as the Linear model. This set of BCs was chosen because it has been used in the previous studies of Falcinelli et al. (2014) and Qasim et al. (2016). The next few sections will describe the Linear model in detail along with two more improved boundary conditions implemented in this study, referred to as the MPC and Contact model.

Table 7.1 The common boundary conditions used in the literature to represent the side fall configuration.

Type	Boundary Conditions	
	At the greater trochanter	**At the distal end**
A	A single node (the most lateral node in the greater trochanter) is constrained in the opposing direction to the applied load and free to translate in the x and z directions.	All the nodes are fully constrained
B	A group of nodes is constrained in the y direction and free to translate in the x and z directions.	
C	A group of nodes is coupled to a pilot node using the rigid surface constrained method. The pilot node is constrained in the y direction while it is free to translate in the x and z directions and free to rotate around all axes.	

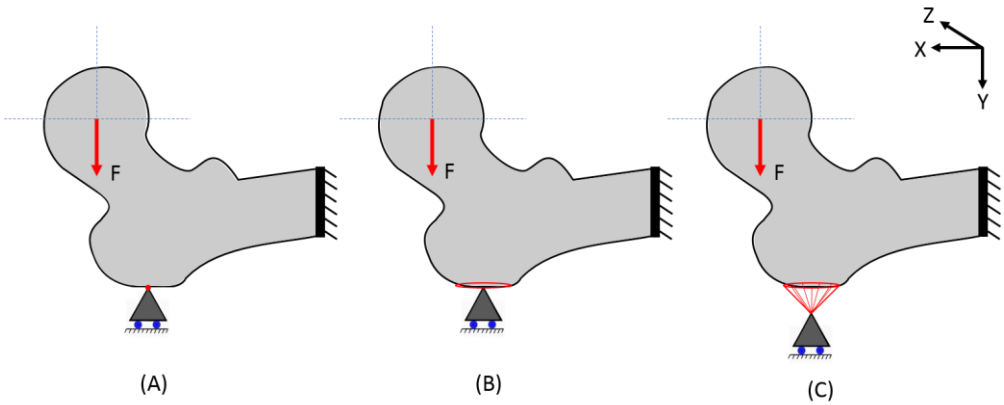

Figure 7.1 Schematic of finite element models with the three different boundary conditions reported in the literature. The details of each boundary condition are described in Table 7.1. Type A is the boundary conditions selected here to represent the common BC used in the literature and is referred to as the Linear model in this thesis.

7.2.1 Linear model

After orientating all the femora using the coordinate system as described in Chapter four (Section 4.3.4), boundary constraints were applied at the most lateral node on the greater trochanter. The displacement of the node was constrained in the y direction, while the translation in the other two directions was kept free. This is to simulate a non-friction slider at the greater trochanter. The distal end of the proximal femur was fully constrained in the x, y and z directions (Figure 7.1A). As mentioned earlier, this boundary condition was used previously in Qasim et al. (2016), who investigated the performance of the finite element model in comparison to the aBMD (in terms of discriminating the fracture and control cases) using the same adult cohort. The limitation of such a boundary condition is the constraints at the greater trochanter, in that the movements are only allowed in the lateral plane, and the fully fixed distal end of the proximal femur. In reality, however, sideways falls are a dynamic event, where there may be multiple contact points between the body and the ground. During the impact of the hip, the greater trochanter region is (indirectly) in contact with the ground, which may lead to some slip and rotation in this area. In other words, the femur might pivot around the ankle joint. It has been shown previously that the inclusion of this movement can improve the predictive accuracy of the FE model in terms of femur stiffness (Rossman et al., 2015). The aim of the current study therefore is to take one step further and investigate if including this movement would improve the stratification accuracy of the model in terms of the risk of hip fracture. Consequently, the linear model used by Qasim et al. (2016) has been modified to implicitly include the pivoting movement, which is described in the next section.

7.2.2 MPC model

The first modified model retained the same boundary condition (non-friction slider) at the greater trochanter. At the distal end, however, a new pilot node was created at an estimated location for the centre of the knee joint centre for each patient. The centre of the knee joint was estimated and confirmed after a sensitivity study; details are provided in Section 7.2.3.2. The pilot node has six DOFs (translation and rotation in the x, y and z directions), which would allow the simulation of a rotational hinge around the knee joint. The distal end of the proximal femur was connected with the centre of the knee joint by the multi-point constraints (MPC) method. The MPC elements related all degrees of freedoms in the x, y, and z directions of the distal nodes to the pilot node. The pilot node was free to rotate around the axis transverse to

the applied load (x axis), while all other DOFs were constrained (Figure 7.2). This was proposed in order to mimic the motion of the knee joint during a fall.

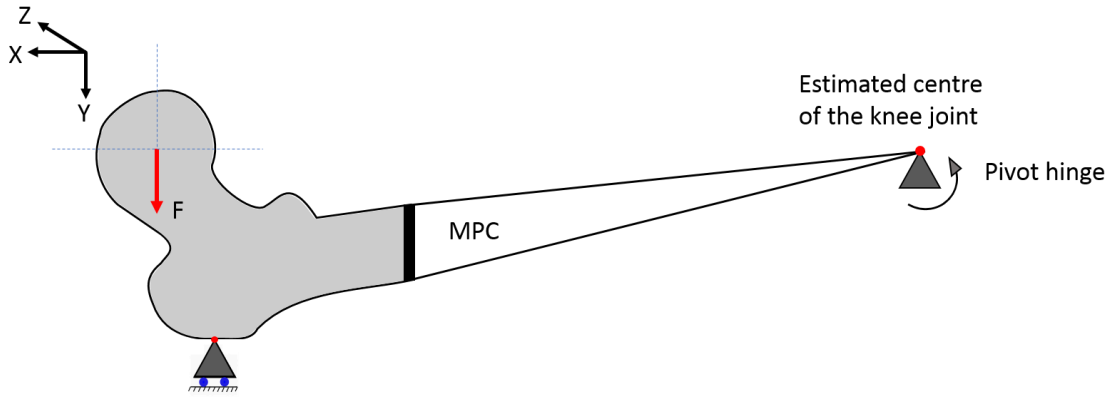

Figure 7.2 Schematic of the MPC model with a non-frictional slider at the greater trochanter and a hinge at the distal end. Multi-point constraints (MPC) elements were used to connect the distal nodes with the pilot node.

While the MPC model allowed rotation around the knee joint compared with the Linear model, it did not take into account the sliding at the lateral greater trochanter during a fall. In order to account for sliding in the simulation, a second modified model was created which allowed the femur to rotate and slide freely without a direct constraint at the greater trochanter. This was achieved by simulating nonlinear contact at the greater trochanter region, which is explained in the next section.

7.2.3 Contact model

The sideways fall condition involves bone (considered as a deformable object relative to the ground) that is in contact with the ground (assumed to be rigid). An infinitely rigid plane (target surface) was modelled at the most lateral node on the surface of the greater trochanter (contact surface) along the y-axis. The initial contact condition of the model was defined as just touching between the rigid plane and the greater trochanter surface. CONTA174 was assigned as a contact element, which is a type of element available in the ANSYS element library for surface contact. It is associated with the 3D target segment elements of 4-node Quadrilateral TARGE170 using a shared real constant set number. The non-linear surface-to-surface contact was evaluated using augmented Lagrangian algorithms.

It should be noted that the contact area continuously changes during the simulation, which is determined by the contact algorithm. Thus, the defined contact surface should be sufficiently large to capture the entire contact region without drastically increasing the CPU time. Consequently, the whole surface area of the proximal femur was selected as the contact surface, except where the boundary conditions were applied.

Similar to the MPC model, the distal cross-section of the femur was constrained to a pilot node located at the estimated centre of the knee joint. The same boundary conditions applied at the pilot node in the MPC model is used here for the contact model. A schematic of the contact model is shown in Figure 7.3.

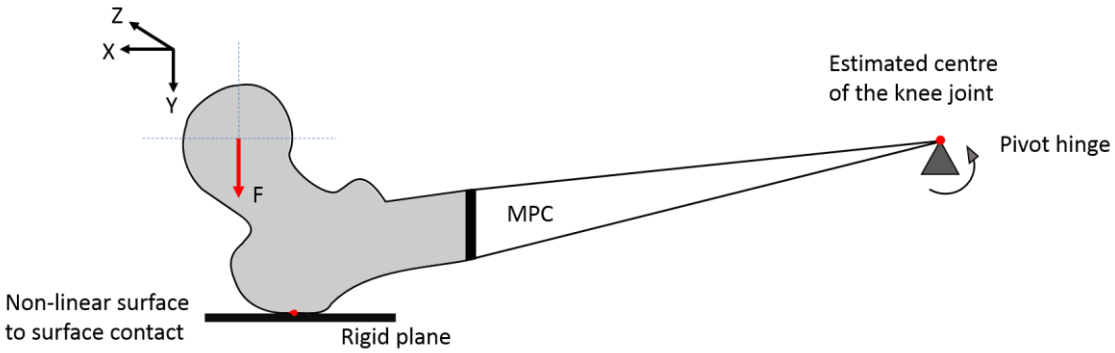

Figure 7.3 Schematic of the Contact model. Nonlinear surface-to-surface contact was defined at the greater trochanter while Multi-point constraints elements (MPC) were used to connect the distal nodes with a pilot node at the estimated centre of the knee joint. The model was free to rotate around a remote pivot point (pilot node) in the z direction with a pivot hinge.

At the time of impact after the fall, high impact forces are generated that could cause high strains on the proximal femur. Due to the irregularity of the femoral geometry, these high strains tend to occur in the weak regions. The exact location of impact will change according to the direction of the fall, however, thereby affecting the distribution of predicted strains. It is therefore important to account for various possible fall directions in the simulation. The next section will describe the range of loading directions used here in the FE models.

7.2.3.1 Loading conditions

A concentrated arbitrary point load of 1 kN was applied to the centre of the femoral head. For both Linear and MPC models the resulting strains can be scaled linearly as the models had

linear mechanical response. A load sensitivity study was performed on the Contact model to confirm that the non-linearity of the contact in the boundary condition would not affect the global linearity of the model. Details of the load intensity study are described in section 7.2.3.2.

Two sets of loading conditions were investigated in this study. The first set consisted of 28 loading directions (LCs), which cover both anterolateral and posterolateral falls. The loading angle was incremented by 10° from 0° to 30° in the frontal plane (adduction) and from -30° to +30° in the transverse plane (internal-external rotation), as shown in Figure 7.4. The lateral angles were not considered because with these orientations (abducted leg), the knee will hit the ground first during the fall, i.e. before the hip. The second set consisted of 16 LCs, which is a subset of the first one in which only the LCs of posterolateral falls were considered (0° to 30° in both frontal and transverse planes with a 10° increment).

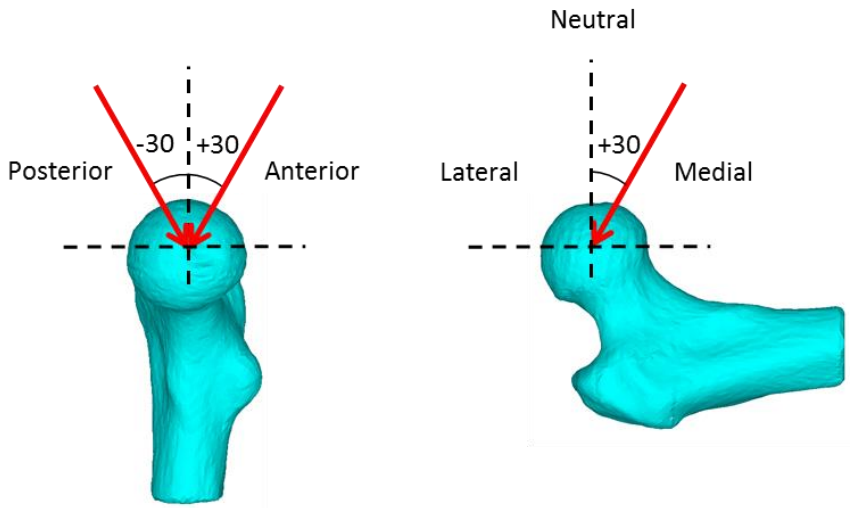

28LCs		Posterior				Anterior		
		-30	-20	-10	0	10	20	30
Medial	0	-	-	-	-	-	-	-
	10	-	-	-	-	-	-	-
	20	-	-	-	-	-	-	-
	30	-	-	-	-	-	-	-

Figure 7.4 Multiple loading conditions (through point force applied to the centre of the femoral head) were used to sample 28 different sideways falls by varying the force direction from 0° to +30° on the medial-lateral plane and from -30° to +30° on the anterior-posterior plane.

7.2.3.2 Sensitivity studies

In order to verify the various settings used for the Contact model, a number of sensitivity studies were carried out, which are described below:

- *Sensitivity analysis of the mesh*

Refinement of the mesh was decided based on post-hoc verification of the strain field smoothness. This was monitored in terms of strain energy error (*ANSYS*, Inc. *Theory Reference)*, which in no case exceeded 8% within the volume of interest, representing the whole surface area of the proximal femur except where the BCs were applied. A mesh convergence study was performed for the model with the highest post-hoc error. Four different element sizes were used (1.5, 3, 3.5 and 4 mm). The mesh reached convergence at an element size of 3 mm, with a predicted maximum difference of 4% in the maximum and minimum principal strains within the volume of interest between the 3 mm mesh and the finest mesh at 1.5 mm (see Figure 7.5). This is comparable with a previous mesh convergence reported in Ariza et al. (2015).

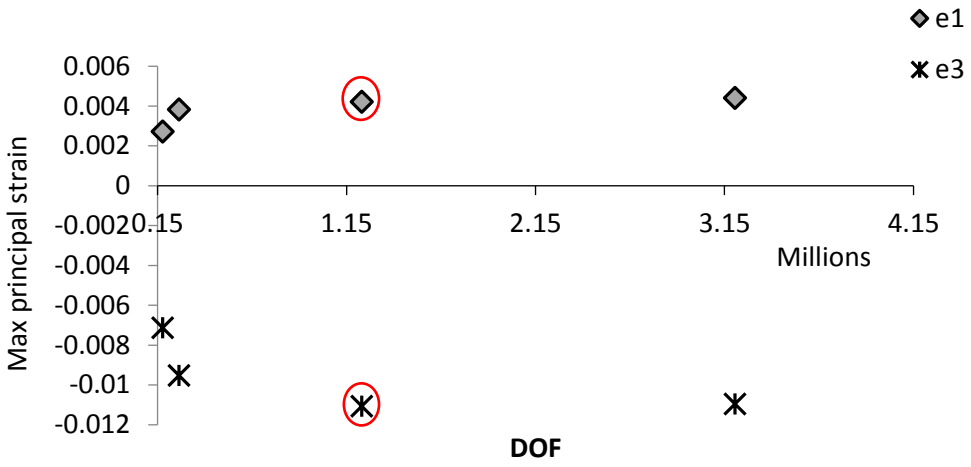

Figure 7.5 Convergence test to evaluate the required level of mesh refinement performed on the model with the highest strain error energy in the cohort. Four different element sizes were used (1.5, 3, 3.5 and 4 mm). The maximum principal strains, e1 and e3, for each mesh are plotted against the number of degrees of freedom of the model. The convergence is achieved with an element size of 3 mm, highlighted by the red circles.

- *Sensitivity analysis of the contact area*

Three different sizes of the contact area were tested for three femurs under three different loading directions. These were: 2 mm (around 500 nodes), 8 mm (around 3000 nodes), and the full surface of the proximal femur except where the BCs were applied (around 30000 nodes). Note that the last number varied according to the fall direction, due to asymmetry. The results showed very small sliding in the contact region, with a maximum value of 0.1 mm. There was no difference in the predicted maximum and minimum first principal strains with little increase in computational cost either. For simplicity, therefore, the full surface of the proximal femur was selected as the contact surface during simulation.

- *Sensitivity analysis of the knee centre location*

The coordinates of the estimated centre of the knee joint were extracted from a full femur anatomy using rigid-body registration and statistical shape model-guided fit (Qasim et al., 2016). Two landmarks were created at the two condyles of the distal end. The midpoint between these two landmarks was estimated as the knee joint centre (see Figure 7.6). A sensitivity study was conducted in order to investigate the effect of the length of the (estimated full) femur on the predicted mechanical response, where the coordinates of the knee joint centre (along the length of the femur) were varied by ±25 mm. The resulting differences in the maximum and minimum predicted principal strains were less than 1%.

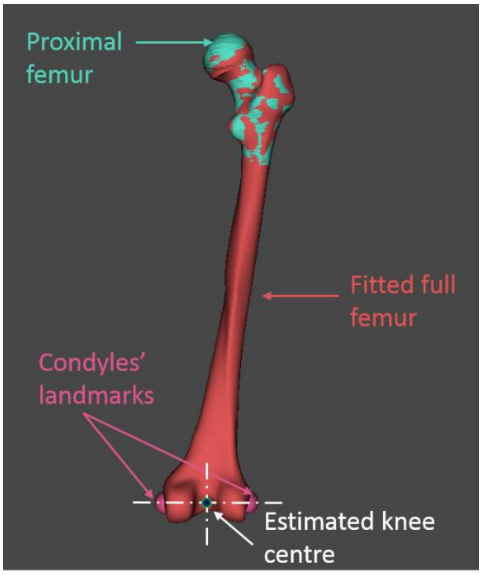

Figure 7.6 A proximal femur (green) superimposed with the fitted full femur (red) for a 64 year old individual. The centre of the knee joint was estimated at the midpoint between the lateral condyles.

- *Load intensity study*

By changing the applied load value from 1 kN to 5 kN, a perfect linear relationship was found between the value of the applied load and the predicted peak principal strain values, whereas the contact pressure changed by up to 50% at the contact area. This confirmed that the nonlinearity of the contact boundary condition does not change the global linearity of the FE model.

- *Solvers and computational time*

A few solvers have been tested to solve the simulation for the nonlinear model, as shown in Figure 7.7. The Spare solver was the most computationally expensive, with 15 hours per loading case. The PCG solver (with Gauss integration point) reduced the computing time to 5 hours. The PCG solver (in combination with the nodal detection method) reduced the computing time further to half an hour per loading case. Therefore, the PCG solver with nodal detection method was used for the simulation.

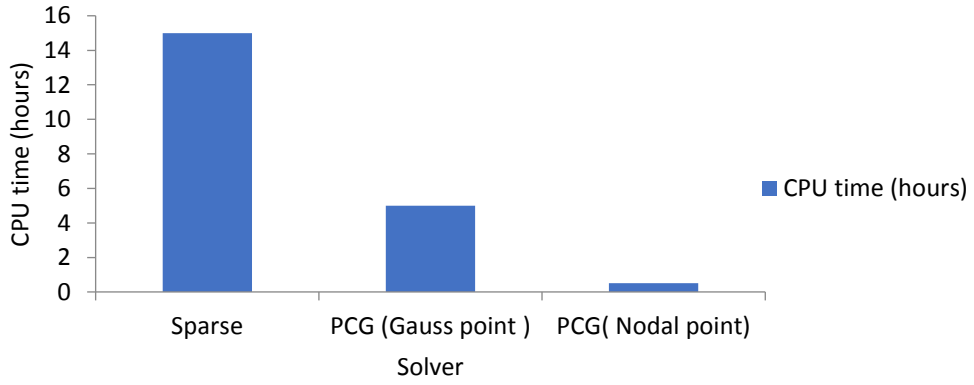

Figure 7.7 CPU time using different solvers: Sparse, PCG solvers with Gauss point and nodal detection methods. The differences in the CPU time using PCG solver are indicated relative to the Sparse solver.

7.3 Strength assessment

7.3.1 Region of interest and differentiation of fracture sites

The region of interest was selected to cover the whole surface area of the femur except for the areas where the BCs were applied. Maximum (first) and minimum (third) principal strains of the surface nodes were analysed under different loading conditions and used to define the fracture type. The predicted fracture types in the FE model were defined as follows. When

the maximum or minimum strain (tensile or compressive) at failure load occurred in sub-capital or trans-cervical regions, sub-capital (SCF) and trans-cervical (TCF) fractures were identified, with both being considered as neck fractures (NF). Similarly, if the maximum or minimum strain occurred at the intertrochanteric or anterior aspect of the trochanteric regions, inter-trochanteric (ITF) and per-trochanteric (PTF) fractures were identified, respectively; both being considered as trochanteric fractures (TF). The fracture types corresponding to the predicted fracture sites are shown in Figure 7.8.

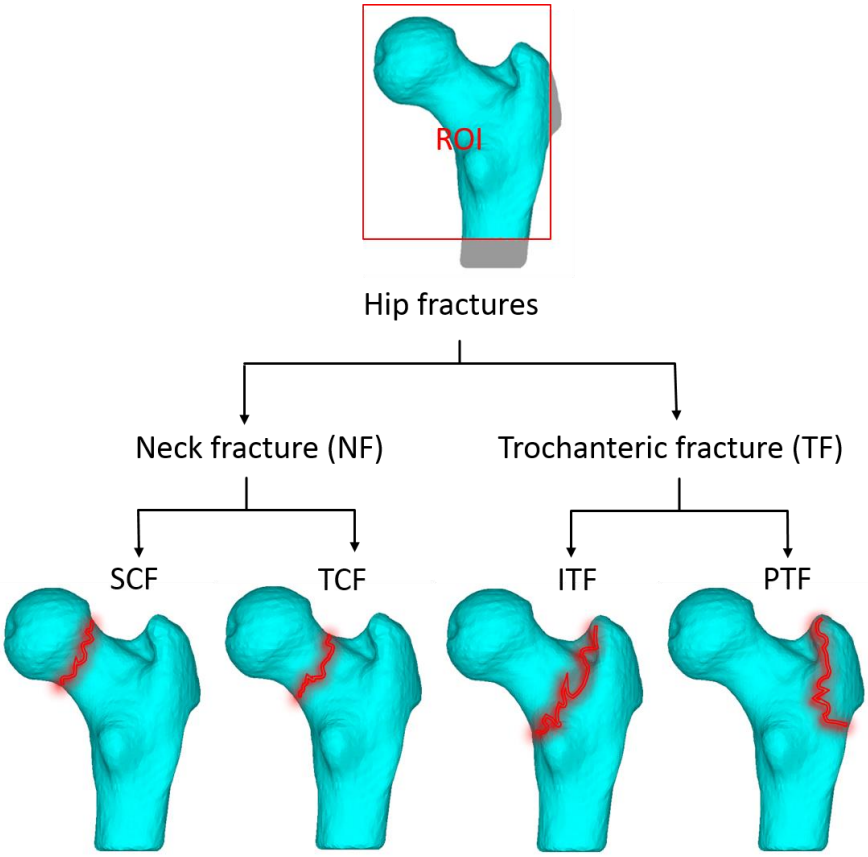

Figure 7.8 The region of interest (ROI) used for the FE analysis of the strength of the femur is highlighted with the red box. Fracture types were classified according to the location of the maximum (first principal strain) or minimum (third principal strain) strain over the surface nodes of the femur. Neck fractures (NF) include both sub-capital (SCF) and trans-cervical (TCF) fractures, and trochanteric fractures include both inter-trochanteric (ITF) and per-trochanteric (PTF) fractures.

7.3.2 Failure criteria

Maximum principal strain criteria were used to estimate the FE strength of the femur. Maximum and minimum principal strains were predicted in the region of interest under each simulated loading direction to find the strength of the femur under that specific falling direction. The threshold values were 0.73% and 1.04% for tensile and compressive strains, respectively (Bayraktar et al., 2004). The principal strains were averaged at the surface nodes on a circle of 3 mm radius, in order to follow the continuum hypothesis avoiding the local effects of the load.

Because of the extensive loading directions intended to be investigated in this study, and furthermore the substantial number of femora to be simulated, a script was coded using Ansys Parametric Design Language, which allowed all simulations to run automatically. The Contact model was solved with a large deflection option and automatic time stepping for the Newton-Raphson scheme available in Ansys for Augmented-Lagrangian contact problems (ANSYS, Inc. Help Guide). All simulations were solved using the preconditioned conjugate gradient-iterative solver (PCG) with a tolerance value of 1E-8. The FE models were run on a high-performance computing cluster at the University of Sheffield (Iceberg). The average running time (for one loading direction) for linear, MPC and contact models was 3 min, 8 min, and 1 hr, respectively.

7.3.3 Statistical analysis

Strength under each loading direction was predicted for all cases. The minimum fall strength (MFS) was then calculated for each patient by identifying the minimum value of the strength across all simulated loading directions. The paired t-test was performed to determine the differences between MFS predicted by the three different models (Linear, MPC and Contact model), and logistic regression models were used to determine the ability of MFS minimum femur strength to classify between the fracture and control group. The area under the receiver operating characteristic (ROC) curve (AUC) was calculated in order to investigate the ability of finite element models to differentiate between the two groups. SPSS software was used to analyse the data (versions SPSS 23.0, and IBM SPSS Statistics 23, IBM Corporation, Chicago, IL, USA). The test was considered to be statistically significant when the p-value was smaller than 0.05.

7.4 Results

7.4.1 Minimum femur strength predicted by Linear, MPC and Contact models

The MFS predicted by the Linear model was larger than that by the MPC and Contact models, with an average difference of 25% (±15%) and 21% (±16%). The mean MFS predicted by the Linear model was 2333 N (SD=604), compared with 1724 N (SD=484) and 1794 N (SD=463) for the MPC and Contact models, respectively. The MFS was significantly different between the control and fracture groups for all FE models, as shown in Table 7.2. Logistic regression showed MFS calculated using Linear, MPC, and Contact models to be normally distributed and significantly associated with the fracture status ($p<0.0001$).

Table 7.2 Minimum femur strength (MFS) in Newtons predicted by the Linear, MPC and Contact models for the control and fracture groups. MFS is significantly different (p-value < 0.0001) between the control and fracture groups for all FE models.

FE Model	Number of LCs	Mean MFS (SD)		% Difference	AUC
		Controls	Fractures		
Linear model	16	2699(494)	2069(545)	23	0.79
	28	2651(506)	2015(525)	24	0.80
MPC model	16	2060(428)	1590(419)	23	0.79
	28	1964(411)	1484(404)	24	0.80
Contact model	16	2100(421)	1630(405)	22	0.79
	28	2033(410)	1555(384)	24	0.82

7.4.2 Minimum femur strength under various loading scenarios

The mean and SD of the MFS under each LC is reported in Table 7.3 for Linear, MPC and Contact models. In general, when the angle in the frontal plane (medial angle in Figure 7.9) increased, the MFS decreased. Similarly, the MFS decreased when the angle in the transverse plane increased (anterior and posterior angles in Figure 7.9). For each of the three models, the minimum mean level of the MFS was found when the direction of the applied load was at 30° in both the frontal and transverse planes. This loading direction represents a posterolateral fall at the most extreme angle of the spectrum. In contrast, the maximum mean of the MFS was found when the loading angle was at -10° in the transverse plane, in both the MPC and Contact model. This load direction represents an anterolateral fall. While for the Linear model, the maximum MFS was found when the loading angle was at 10° in the

transverse plane. However, the next maximum MFS was found also under -10° in the transverse plane.

Although posterolateral falls were the most critical loading directions for most cases, the MFS of a large number of cases was predicted under anterolateral falls: the Linear model predicted 40 cases, the MPC model predicted 27 cases, and the Contact model predicted 23 cases. These numbers are the sum of the cases under all the posterior LCs, as shown in Table 7.4.

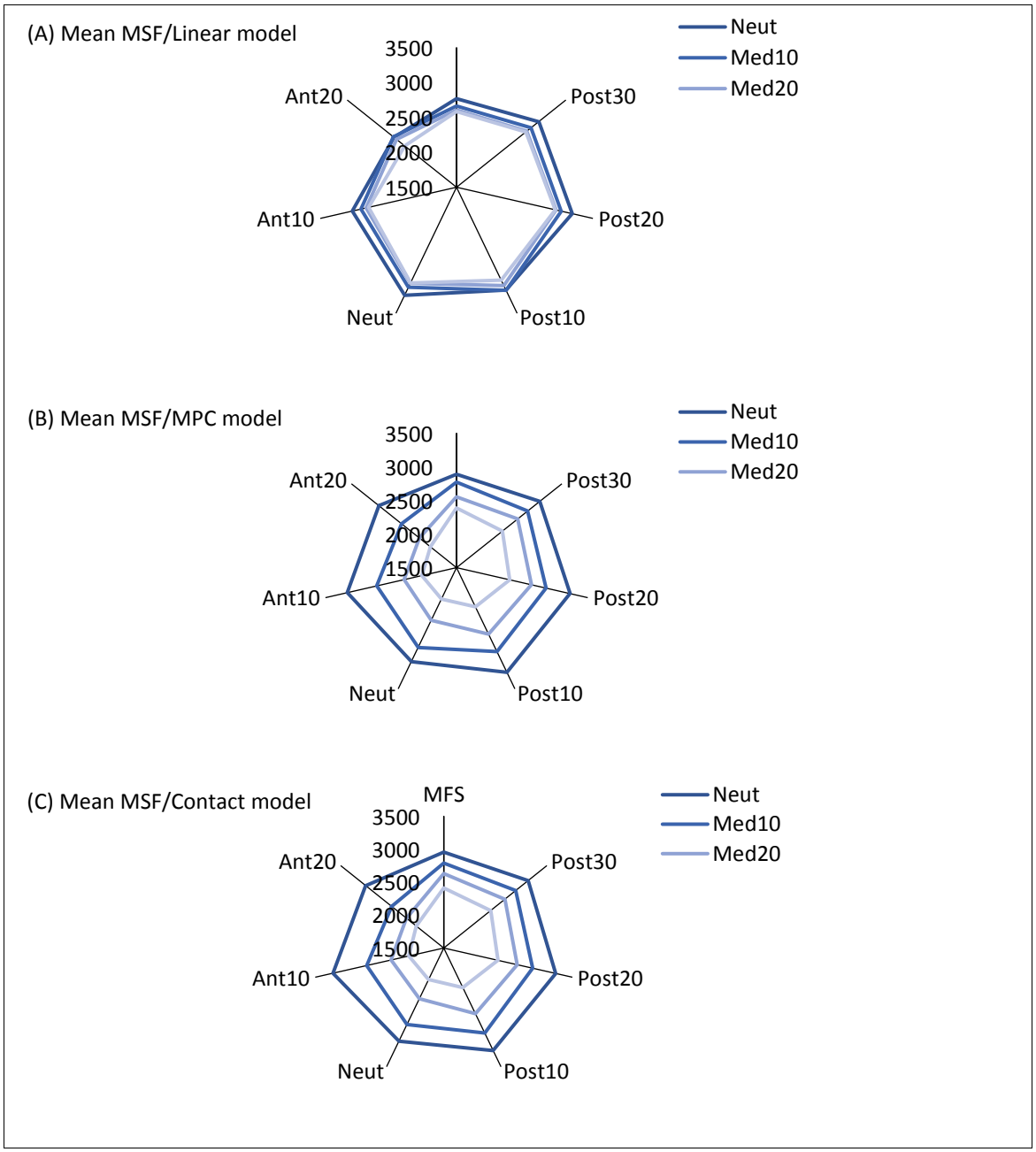

Figure 7.9 Mean of MFS plotted for each LC for: (A) Linear model, (B) MPC model, and (C) Contact model.

Table 7.3 The predicted mean MFS with the standard deviation (SD) under each LC for Linear, MPC and Contact models.

			Mean (SD) of MFS (N)						
			Posterior			Neutral	Anterior		
			-30	-20	-10	0	10	20	30
Medial angle	Linear model	0	2768(809)	3005(878)	3197(921)	3132(868)	3214(899)	3030(781)	2648(698)
		10	2663(765)	2863(815)	3035(854)	3135(883)	3088(845)	2903(727)	2656(652)
		20	2606(735)	2786(778)	2959(822)	3060(852)	3023(801)	2827(688)	2599(929)
		30	2584(732)	2767(766)	2948(809)	2975(790)	3019(783)	2791(673)	2450(617)
	MPC model	0	2888(825)	3081(901)	3231(928)	3227(907)	3050(847)	3167(926)	2977(858)
		10	2771(807)	2849(825)	2865(837)	2885(833)	2816(875)	2718(901)	2545(908)
		20	2552(807)	2660(784)	2642(751)	2597(806)	2368(727)	2300(713)	2208(629)
		30	2387(727)	2369(651)	2310(651)	2146(619)	2021(544)	2030(414)	1999(540)
	Contact model	0	2953(808)	3139(863)	3241(915)	3227(913)	3068(853)	3224(919)	3015(840)
		10	2787(812)	2896(833)	2883(825)	2932(878)	2789(781)	2699(772)	2511(689)
		20	2628(837)	2684(786)	2642(734)	2606(796)	2353(703)	2320(694)	2223(615)
		30	2409(702)	2409(742)	2343(652)	2167(796)	2031(533)	2044(504)	2032(534)

Table 7.4 Number of patients predicted with an MFS under each LC for Linear, MPC and Contact models. NA means that no case was predicted with MFS under that LC.

			Number of patients						
			Posterior LCs			Neutral	Anterior LCs		
			-30	-20	-10	0	10	20	30
Medial angle	Linear model	0	NA	NA	NA	NA	NA	NA	3
		10	4	NA	1	NA	NA	NA	10
		20	8	NA	1	NA	NA	1	23
		30	24	2	NA	NA	NA	2	19
	MPC model	0	4	NA	NA	NA	NA	NA	NA
		10	1	NA	NA	NA	NA	NA	2
		20	10	1	1	4	7	4	4
		30	4	5	1	3	15	7	25
	Contact model	0	3	NA	NA	NA	NA	NA	NA
		10	1	1	NA	NA	NA	NA	2
		20	6	NA	1	2	9	3	4
		30	7	2	2	8	18	9	20

7.4.3 Discrimination of fracture and control cases

The highest discrimination accuracy was achieved by the Contact model, when considering both anterolateral and posterolateral fall directions (see Table 7.1). The value was 7% better than aBMD. Under the largest spectrum of loading angles (28LCs), AUC was found to be 0.80, 0.80 and 0.82 for Linear, MPC and Contact models, respectively, compared to 0.75 using aBMD alone, as measured previously by Qasim et al. (2016) for the same cohort. A lower performance was found when all the anterolateral falls were removed (i.e. accounting for posterolateral falls only), with an AUC of 0.79 for each of the Linear, MPC and Contact models.

7.4.4 Prediction of Fracture types

Different types of femur fractures were predicted by the MPC and Contact models, as shown in Figure 7.10. By analysing the fracture type that is associated with the MFS (e.g. the weakest orientation among all loading directions), NFs were the most frequently predicted fracture types. The MPC model predicted 66 cases with NFs and 32 cases with TFs (four cases were PTFs), while the Contact model predicted 72 cases with NFs and 19 cases with TFs (three cases were PTFs).

When fracture type was analysed for each of the simulated LCs, however, PTFs were also predicted in 10 cases by the MPC model and in 13 cases by the Contact model. In contrast, the Linear model did not predict any PTFs.

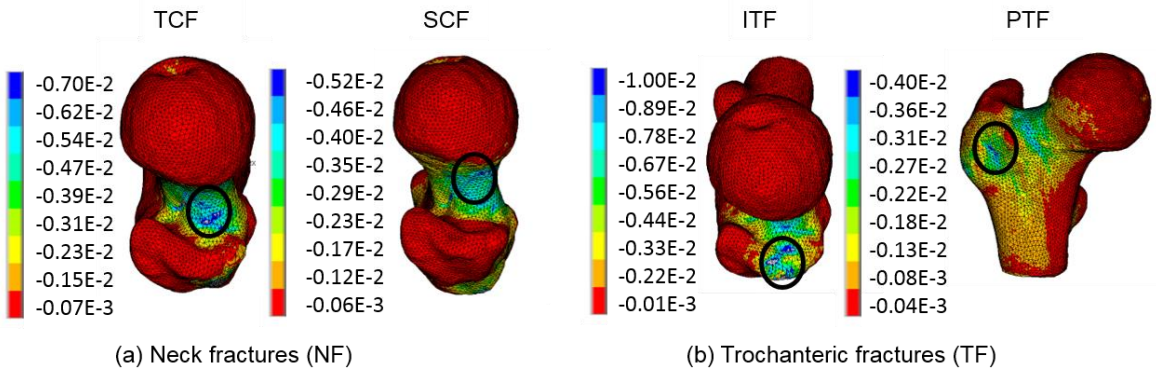

Figure 7.10 Fracture types corresponding to each of the predicted fracture sites using the Contact model. Circled: Predicted fracture site. (a) The predicted fracture sites located at the neck region, either trans-cervical (TCF) or sub-capital fractures (SCF). (b) The predicted fracture sites located at the trochanteric region, either inter-trochanteric (ITF) or per-trochanteric fractures (PTF).

7.5 Discussion

The main aim of this study was to investigate the improvement in the accuracy of the FE approach in terms of stratifying patients under the risk of fracture. The improvements considered in this chapter are: (a) Three types of displacement boundary constraints; and (b) Different ranges of fall directions.

Our result showed that posterolateral falls were the critical fall conditions producing minimum load to fail, as suggested by previous literature. For a considerable proportion of cases, however, minimum femur strength was also associated with a fall to the front (anterolateral falls). This might be related to the variations in the geometry of the proximal femur and the material properties of the bone at tissue level. These results suggest that it may be inappropriate to consider the same critical fall direction for all individuals. By ignoring anterolateral falls, therefore, one may reduce the ability of the FE model to classify patients according to their risk of fracture. This may also explain the reason behind the high predictive accuracy of Nishiyama et al. (2014) (AUC=0.94), compared to Falcinelli et al. (2014) and Qasim et al. (2016), since Nishiyama et al. considered a range of falls including both anterolateral and posterolateral falls.

Considering the effect of displacement and loading conditions on the predictive accuracy of the FE model, the stratification accuracy of the Contact model (AUC=0.82) was higher than the MPC and Linear model (AUC=0.80), when both anterolateral and posterolateral falls were considered. When only the posterolateral falls were considered, AUC for all three models was less than 0.79. It is clear, therefore, that the use of multiple loading directions in the Contact model provided the best discrimination between fracture and control groups. This is however, with a trade-off of computational time, since the MPC model is less computationally expensive than the Contact Model (8 min versus 1 hr for a typical simulation). It should be noted that although the 2% increase in AUC is subtle, this could be significant depending on the specific application, especially if the main aim of the proposed study is to accurately stratify or predict fracture. The boundary condition should therefore be carefully chosen depending on the intended outcomes of the study and the available resources.

Although under posterolateral fall conditions, the classification accuracy of the three models was equal (AUC=0.79), the femur strength predicted by the MPC and Contact model was

substantially less than that predicted by the Linear model (by 26% and 23%, respectively). This suggests that the inclusion of the MPC method at the distal end of the femur had a similar effect (although not identical) to the non-linear contact condition, and both models are less constrained compared with the Linear model (also used in Qasim et al., 2016). Other studies (Dragomir-Daescu et al., 2011; Keyak, 2001; Rossman et al., 2015) have also reported an overestimation of femur strength when direct displacement constraints were applied to the greater trochanter. Among these studies, Rossman et al. (2015) also investigated the effect of using contact and MPC methods, but their results are not directly comparable with the current study because they used a slightly different boundary condition (with two contact regions being modelled at both the femoral head and the greater trochanter). This highlights the importance of using appropriate boundary conditions at the trochanteric and distal aspect of the proximal femur in order to represent a more realistic sideways fall.

Despite the close similarity in the MFS predicted by the MPC and Contact models for the majority of the cases in our study, with an absolute difference of less than 10%, nine cases had higher differences, with a range of 20%-42%. This could be related to the inter-personal variation in trochanteric geometry, which in turn has a greater sensitivity towards the type of displacement boundary condition. In general, the contact interaction is more sensitive to complex trochanteric geometry (compared with the MPC constraint). This could lead to the larger difference seen in these nine patients.

Under the critical LCs of each case, maximum principal strain was predicted at different regions of the proximal femur, the locations of which indicate the potential fracture patterns. For the majority of cases, maximum compressive strains mainly developed in the superior region of the neck (Verhulp et al., 2008), which gives the potential to produce NFs. The Contact model predicted 72 cases with NFs, while the MPC model predicted 66 cases. For patients predicted to have TFs, maximum strains were located in either the superior intertrochanteric region (compressive strains), or the inferior region (tensile strains). Among these TFs, there were three predicted PTF cases from the MPC and Contact models. When analysing the fracture patterns considering all 28 LCs, however, PTF was predicted in 13 cases by the Contact model and ten cases by MPC model.

The results showed that an improved boundary condition (either non-linear contact or a kinematically equivalent linearized version using MPC) can simulate PTFs, since the Linear

model did not predict any PTF. A good agreement between the strain locations predicted by FE models using those boundary conditions (Contact and MPC) and the experiments has been reported previously (Ariza et al., 2015; Dragomir-Daescu et al., 2011). Unfortunately, neither of those studies reported if per-trochanteric fractures (PTF) were predicted by the FE model. This could be because neither study conducted a specific investigation on the prediction of PTF.

In conclusion, this study showed that, although posterolateral falls represent the critical fall conditions for most cases, anterolateral falls are critical falls for other cases. Therefore, accounting for both fall conditions when classifying fractured and non-fractured femurs is necessary for an accurate classification. Both the MPC and Contact model performed better than the more commonly used Linear model in terms of both fracture-type prediction and stratification power. Although both models were able to predict PTF, the Contact model had a better classification power than the MPC model but was more computationally expensive. Therefore, caution needs to be taken in selecting the best method depending on the study objective and resources available. The study also demonstrated the importance of including a more physically representative boundary condition, as well as a wide range of loading directions, in order to predict femur strength accurately.

8 GENERAL DISCUSSION, LIMITATIONS AND FUTURE WORK

The main aim of this thesis was to develop a subject-specific CT/FE modelling procedure to investigate the mechanical response of human long bones under various loading conditions, for two different age groups: young children (in particular, femur and humerus) and elderlies (proximal femur and hip fracture). In order to achieve this, the thesis was divided into three different studies. Study I: strength of the paediatric femur under bending and torsional loads, study II: spontaneous humeral fractures in infants, and study III: strength of the proximal femur under side fall loading conditions.

In the first study, a novel CT/FE modelling procedure was developed in order to predict the strength of the paediatric femur under bending and torsional loads, which could help to provide quantitative information on fracture tolerance in very young children (zero to three years old). In the second study, by using a similar modelling procedure, an existing hypothesis on spontaneous humeral fracture (in infants while rolling) was investigated. Finally, in the third study, three different BCs of a subject-specific CT/FE modelling of a side fall configuration were investigated in order further to increase the classification accuracy (between fracture and non-fracture cases) using the predicted minimum femoral strength under a wide range of falling directions.

For the paediatric studies, the predicted strength values were compared against those previously reported in the literature. For the adult study, the improvement in the classification accuracy of the CT/FE models was compared by calculating the AUC for each of the tested BCs.

Each of the following sections considers the limitations of the three studies and future work that might be undertaken in order to improve the CT/FE models presented in this thesis. Note that the objectives might be different according to the specific areas of application.

8.1 Study I

The results of this study showed that CT/FE method can be effectively used to investigate the biomechanical behaviour of paediatric bone, in a way that is similar to adults. CT/ FE analysis has been previously shown to be an effective method to study adult bones non-distractively. Although this approach has been adopted to study various children's bones (Angadi et al., 2015; Meng et al., 2017; Tsai et al., 2017; Yadav et al., 2017), it was never systematically used to determine bone strength quantitatively over a defined age range for a specific long bone.

The model developed in this study provided predicted strengths for 30 cases of very young children (from new-born to three years old) under both bending and torsion (for the first time) loads. These values are a promising first step towards age (or developmental) related quantification of fracture tolerance in children. Such information is scarce for very young children and could provide a valuable input when diagnosing accidental and inflicted injuries. Furthermore, such data can also be use in different industrial applications aimed to improve child safety, such as car seat manufacturers, pram manufacturers, etc.

Although none of the cases has died because of any bone disease, some causes of death, such as the hypoplastic left heart syndrome, may have secondary effects on the skeletal development as they might had affected the mobility of the infant. However, it should be noted that all cases were carefully reviewed by an experienced paediatric radiologist. This was to ensure that any conditions directly affecting the musculoskeletal development, and hence the bone properties, was excluded.

The material properties (density and modulus of elasticity) of the bone were mapped from the attenuation coefficient of the CT scans using the relationship obtained in the literature. The elements were assigned inhomogeneous isotropic material properties. Paediatric bone is more isotropic than adult bone, especially at the diaphysis (Cheong, 2014). It became more anisotropic at the ends of the long bone around the region of the epiphyseal plates (Cheong, 2014). Since the loads applied in the current study was at the diaphysis of the bone, the assumption of isotropy is considered to be sufficient. However, further studies in the future are needed to investigate the level of anisotropy of paediatric bone compare to adults' bone.

The age distribution of the cohort is non-uniform. The majority of the cases were younger than six months old, while only two cases were one year old, one was two years old, and one

was three years old. This makes it difficult to suggest a robust regression analysis on the relationship between bone strength and age/mass. Two possible relationships were therefore proposed (linear and quadratic, Figure 5.8 and Figure 5.12). It is probably reasonable to assume that at birth bone strength cannot be zero. This would invalidate some of the linear regression results because at this age they produced negative bone strengths. This should be taken into account when using regression results in the future. There is, however, an on-going post-mortem study at the Sheffield Children's Hospital where more CT scans are being collected on children. It is therefore likely that more cases will be added to the study in the future, especially those aged between six months and three years old. These additions would help to build a unique collection of children's CT data for various long bones (even the whole skeleton), based on which regression analysis can be carried out in order to determine the relationship between bone strength and age/mass or developmental stages. Furthermore, such a database would also allow us to create surrogate models that can be used to enhance our understanding of bone growth and the injury tolerance of developing bones.

One of the current study assumptions was that cortical bone in children behaves similar to adults' bone and fails under the same peak strain (Bayraktar et al., 2004). Therefore, failure strain criterion used for adults' bone could be adapted and used for children's bone. It has been reported that the peak elastic modulus in infants and adults is comparable (Li et al., 2015). Therefore, assuming bone as a fragile material is somehow conservative with respect to the amount of energy absorption before failure. In reality children's bone behaves more like a ductile material, which means the load to failure would be higher. Nevertheless, if failure was assumed when the proportionality limit is exceeded, the results would be quite similar to those reported here.

Because data on paediatric bone at a very young age (such as infants) are scarce in the literature, the high correlation reported by Öhman et al. (2011) between the ash density and both strength and stiffness was applied here. The main limitation of this is that Öhman studied children aged 4–15 years old, compared with the age range of 0–3 years old in the current study. Nonetheless, these assumptions do lead to results that are comparable to the previous experimental data: the predicted failure strength in this study was within the range of those reported in Forman et al. (2012), Miltner and Kallieris (1989) and Ouyang et al. (2003). Future

studies are required to further confirm the ash density to stiffness correlation in children, however, especially in the infant age range.

Changes in paediatric bone at the tissue level were not taken into account in the current computational model. Changes in the microstructure of bone during early life are influenced by the mineralization level, bone matrix structure, and collagen composition. These in turn may have an effect on the biomechanical properties (Bennett and Pierce, 2010). While it would be possible to include these in the FE model, HRpQCT images would be needed to inform the microstructure. This is beyond the scope of the current study, but would be a desirable area to explore in the future, particularly if the models were to be applied to study paediatric musculoskeletal diseases, such as osteogenesis imperfecta.

Simulating other loading conditions will also be helpful in order to provide a full spectrum of injury tolerance. These loading conditions could include compression, tensile and combination loadings, which are frequently presented in both accidental and inflicted injuries. In real life, various loads act on the bone leading to fracture at various locations and with different patterns. The model prediction of bone fracture (or not) can be compared with the force resultant from the physical events described by parents/carer predicted from a dynamic model, to provide quantitative evidence of the likelihood for such injury to occur. In the future, this will provide additional information to assist clinical diagnosis in potentially abusive fractures.

Every FE model must be validated in order to ensure that it accurately predicts the mechanical behaviour of bones. Work is therefore needed in the future to confirm the validity of the models developed here. As reported in Cheong et al. (2017), testing young animal bones can be one potential approach, taking into account the differences between animals and humans.

8.2 Study II

The second study investigated the possibility of producing spontaneous humeral fracture in infants when rolling from a prone to supine position without the intervention of any external forces. This was done using the CT-based finite element modelling approach developed in Study I.

The results showed that the predicted maximum first principal strain for all the simulated positions of child's hand were lower than the elastic limit of human bone. Moreover, the highest predicted strains were substantially lower with a difference (on average) of more than 80%. Therefore, the results of this study suggest that it is highly unlikely for the bone to fail spontaneously, given the underlying modelling assumptions.

Contrary opinions exist about the hypothesis of spontaneous humerus fracture for infants at the rolling age (Jenny, 2014; Rosado, 2014; Somers et al., 2014). Most of these reports, however, rely on examination of the injury and description of the caretakers, with little quantitative evidence. One of the important factors that can be readily investigated by the FE model is to compare between the force acting on the bone and failure (fracture) force. This dilemma was therefore investigated here for the first time using a CT/FE modelling approach that takes account of personalized geometry and the material properties of the bone. The current results support the opinion that children at very young age (such as rolling stage), who can barely support their body weight against the gravity, would not have sufficient strength to exceed failure limit of a long bone, such as the humerus (Rosado, 2014). However, in order to confirm this finding, further investigations are required.

Since this study is the first of its kind, there are number of limitations to be addressed in the future. First, only a small number of cases (three) were simulated, which was insufficient to draw a clear conclusion about the hypothesis. This can be addressed in the future when more cases within the specified age range are collected at the Sheffield Children's Hospital. A number of assumptions were also made during this study, due to a lack of input data in the literature. For example, the time needed by an infant to complete a rolling manoeuvre, and the portion of the body mass contributing to the rolling motion are unknown. Consequently, a worst-case scenario was chosen. The minimum time to complete a roll (collected from online resources as mentioned in in section 6.2.2) was used to calculate the accelerations. Similarly, it is reasonable to assume that not all the body mass of the child contributes to the rolling (e.g. the head of the child). Nonetheless, to provide the worst-case scenario, the whole-body mass was considered in the model to calculate the required moment of each child. These assumptions are likely to provide a gross over-estimation of the moment. Future work should also aim at establishing more accurate boundary conditions for the rolling manoeuvre. This needs to be combined with more accurate calculation of the loads acting on

the humerus during rolling from prone to supine position. This can be achieved by monitoring the motion of a rolling infant using motion sensors and estimating the amount of force acting on the humerus using whole body dynamic models developed for children. This could be achieved following similar approaches as those used to capture various body motions in adult investigations (Bonnet et al., 2013; Latella et al., 2016; Rajagopal et al., 2016; Tamburini et al., 2018). Such information would help to enable a more accurate measurement of the moment produced by the body during rolling, specifically that acting on the humerus. It should be noted, however, that all the currently available dynamic models were developed to simulate adults only. Further investigations are therefore required in order to apply these to children.

Lastly, the non-mineralized bone at the proximal humerus (which forms most of the shoulder joint) was not taken into account in the FE modelling. One possibility is that a distortion of the shoulder joint might occur before humerus fracture. To study that, there would be a need to model the whole shoulder joint with both the mineralized and non-mineralized bones and surrounding soft tissues. Investigations are therefore needed in the future, perhaps with a whole shoulder model similar to those developed to study adult shoulder joint biomechanics (Büchler et al., 2002; Favre et al., 2009; Zheng et al., 2017).

Experimental laboratory studies could be done in the future to understand the biomechanics of such accidents (humeral fractures during a roll). This could be conducted using an instrumented test dummy to assess the biomechanics associated with such injury and examine the risks. Such dummies have been used in the past to investigate paediatric injury risk, such as falling from a short distance (Bertocci et al., 2003; Ibrahim and Margulies, 2010) and playground accidents (Sherker et al., 2003).

Epidemiological information, if available, can help to evaluate the incidence of such fractures and the common fracture locations/patterns. Such data can help to collect the missing information that are needed to carry out similar studies to reach a well-informed conclusion.

8.3 Study III

The main aim of this study was to investigate the improvement in the accuracy of the CT/FE models of side fall configuration to classify fracture and non-fracture cases. This was done by simulating various BCs and loading conditions. Another aim was to investigate if CT/FE models are able to predict all types of fractures observed clinically, including per-trochanteric fracture.

The study results showed that including multiple side fall directions (i.e. both anterolateral and posterolateral falls) and refined boundary conditions could increase the classification accuracy of the FE models. With these improvements, the highest classification accuracy predicted by the current study was 82%, which is modestly higher than DXA/aBMD at 75% (Qasim et al., 2016). Although this is not a large increase, it should be taken into account that the model is very close to the highest predictive accuracy that can be achieved by FE models (Viceconti et al., 2018).

One of the limitations of the current study was not accounting for the soft tissues surrounding the greater trochanter, which are likely to have some damping effects upon impact. A direct contact between the bone and ground was assumed in the Contact model. Soft tissue provides protection by absorbing some of the impact forces during the fall. Yet, during the fall the region of impact is the greater trochanter area where there is very little soft tissue, so its effect is likely to be marginal. However, the thickness of the soft tissue in the greater trochanter region will vary among individuals. In addition, a person wearing a thick layer of clothes (heavy coat for example) would also add to the damping effects upon impact. Including these factors in the simulation was considered beyond the scope of the current study, but can be investigated in the future, using statistical models for example.

The probability of fall in different directions vary for each patient, thus, the fall direction associated with the minimum strength predicted by the current study may never occur for that patient. Therefore, considering the same range of falls for all patients, while the geometry of the femur and the orientations of the femoral neck are different among individuals, could be considered as a weak assumption. The same could be said regarding the importance of including the whole femur, as considering the proximal femur only may lead to uncertainties in the anatomical orientation and hence alignment of applied force. It has been

shown that this issue could be minimized to some extent by correcting the anatomical orientation of the proximal femora using atlas information (Qasim et al., 2016), which was also considered in the current study.

Another limitation is that a fall event may have multiple impact points instead of a single forward impact to the hip, which was considered here. A person may extent the hand to prevent the fall, thus the upper limb could be the first impact point before the hip lands on the ground. This would be an interesting area to investigate using dynamic models at the body in the future. A more advanced model could also include multiscale information, such as patient's height and weight, in order to predict the risk of fracture. Although studies are already available at the body level, work that readily combines quantitative data at both levels only recently emerged via the multiscale approach.

In contrast to the FE model of paediatric bone, CT/FE models of side fall in adults have already undergone enormous developments to achieve the current predictive accuracy in terms of bone strength. Studies are still ongoing to improve the classification accuracy further, however.

Improvements can be made in the Contact model definition. For example, one could model the soft tissue surrounding the greater trochanter (skin, fat and muscles). It has been reported that considering soft tissue may increase the predicted fracture limit of the bone in adults by 11% (Kerrigan et al., 2003). Another improvement would be to introduce frictional contact between the skin and the impacted surface of different kinds of materials, from very stiff to softer surfaces. Such improvements would further increase the nonlinearity of the model, however, and hence increase the computational demand.

In order to mimic a more realistic fall event, a dynamic model could be developed, which can allow the sliding/or slipping of the hip over the impact surface. This would include a possible change in direction of the impact force, which may lead to a change in the amount of force transferring to the proximal femur. Dynamic modelling software (e.g. LS-DYNA) could be used for such a model.

9 SUMMARY AND CONCLUSIONS

The overall aim of this thesis was to develop non-invasive tools that can accurately predict the strength of human long bone in very young children and older adults. Two applications were presented in this thesis: (1) predicting injury tolerance within the paediatric population, and (2) fracture risk prediction in elderly patients during a fall, so as to discriminate between patients under according to their risk of fracture more accurately (classifying fracture and non-fracture cases). The work of this thesis gathered techniques from different fields, including both engineering and medicine.

An exhaustive literature review was conducted on the incidence and epidemiology of long bone fractures in very young children and fragile hip fractures among the elderly. The review of the literature revealed that paediatric long bone fractures make up about 31-76% of all inflicted injury cases (Caffey, 1946; King et al., 1988; Loder et al., 2006; Worlock et al., 1986), and osteoporotic hip fractures occur among approximately 40–50% of elderly women (Johnell and Kanis, 2005), with 90% of all fractures resulted from falls (Hayes et al., 1993).

In the current clinical regime, identification of inflicted injuries in young children and differentiating them from fractures sustained from unintentional accident is challenging. This is partly due to the lack of information available in the literature on paediatric bone. In order to provide some much-needed quantitative information, a novel CT/FE model was developed in Study I. The study reported the fracture tolerance of 30 young children, aged between new-born and three years old. The strength of the femora was successfully predicted under two different loading types, bending and torsion.

Study II showed that the CT/FE technique developed in Study I can be tailored to study a specific case of suspected injury: spontaneous humeral fracture of infants while rolling from prone to supine. It was found that, with the current assumptions, it is unlikely that infants are able to fracture their humeri while rolling from prone to supine without any external forces.

In biomechanical studies of adults, the ability of the FE model to predict different fracture types as observed in the clinic was investigated. To cover these objectives, three different BCs were investigated under a wide range of fall directions. Comparison was made to select the

most appropriate BCs that mimic most closely the side fall event, and that could therefore improve the accuracy in terms of classification and fracture prediction. It was found that more relaxed BCs (MPC and Contact models) performed better than more constrained BCs (Linear model), in terms of both fracture-type prediction and classification accuracy. In terms of classification accuracy, the Contact model produced the best classification power but was computationally expensive. The selection of the best method to use in a particular circumstance therefore needs to be done carefully, taking account of the study objectives and availability of resources.

In summary, the novel features of this thesis include the following:

1) The development of an innovative CT/FE model that can successfully predict the strength of paediatric long bones under bending and (for the first time) torsion loads;

2) The enhancement of the literature in respect to the fracture tolerance of children's femora at a very young age (new-born to 3 years old);

3) Study II was the first of its kind to examine a hypothesis in respect to paediatric fracture using personalized FE models, debating that hypothesis under the current assumptions;

4) The comparison of the effect of various boundary conditions, representing side fall configuration, on the classification accuracy of the CT/FE model for fracture and non-fracture patients;

5) The consideration of a wide range of loading conditions, covering all the possible fall directions, including various posterolateral and anterolateral falls, while investigating the accuracy of the CT/FE model in terms of prediction and classification, and;

6) The prediction of all hip fracture types including per-trochanteric fracture, which has rarely been predicted and reported in the literature on previous FE models.

REFERENCES

Anderson, C., 1994. Bone histomorphometry, Bone and Mineral. doi:10.1016/S0169-6009(08)80063-3

Angadi, D.S., Shepherd, D.E.T., Vadivelu, R., Barrett, T.G., 2015. Orthogonal Digital Radiographs - A Novel Template for a Paediatric Femur Finite Element Model Development, in: IFMBE Proceedings. Springer International Publishing, Vietnam, pp. 175–178. doi:10.1007/978-3-319-11776-8

AO Fundation, 2018. AO/OTA Fracture and Dislocation Classification Compendium [WWW Document]. J. Orthop. Trauma. URL https://www.aofoundation.org/Structure/search-center/Pages/AOSearchResults.aspx?include=Top/anatomy/radius-ulna&k=fracture+classification

Ariza, O., Gilchrist, S., Widmer, R.P., Guy, P., Ferguson, S.J., Cripton, P. a, Helgason, B., 2015. Comparison of explicit fi nite element and mechanical simulation of the proximal femur during dynamic drop-tower testing. J. Biomech. 48, 224–232. doi:10.1016/j.jbiomech.2014.11.042

Barber, M.A., Sibert, J.R., 2000. Diagnosing Physical Child Abuse: the way forward. J. Contin. Med. Educ. 76, 743–749.

Bardyn, T., Reyes, M., Larrea, X., Büchler, P., 2010. Influence of smoothing on voxel-based mesh accuracy in micro-finite element, in: Computational Biomechanics for Medicine. pp. 85–93. doi:10.1007/978-1-4419-5874-7_10

Basu, P., Beall, A., Simmons, D., Vannier, M., 1985. 3-D femoral stress analysis using CT scans and p-version FEM . Biomater Med Devices Artif Organs 13, 163–186.

Baudoin, C., Fardellone, P., Sebert, J.-L., 1993. Effect of sex and age on the ratio of cervical to trochanteric hip fracture: A meta-analysis of 16 reports on 36,451 cases. Acta Orthop. Scand. 64, 647–653. doi:10.3109/17453679308994590

Bayraktar, H.H., Morgan, E.F., Niebur, G.L., Morris, G.E., Wong, E.K., Keaveny, T.M., 2004. Comparison of the elastic and yield properties of human femoral trabecular and cortical

bone tissue. J. Biomech. 37, 27–35. doi:10.1016/S0021-9290(03)00257-4

Bennett, L.B., Pierce, M.C., 2010. Bone health and development, in: Jenny, C. (Ed.), Child Abuse and Neglect: Diagnosis, Treatment, and Evidence. Elsevier Inc., St. Louis, Missouri.

Bertocci, G.E., Pierce, M.C., Deemer, E., Aguel, F., Janosky, J.E., Vogeley, E., 2003. Using test dummy experiments to investigate pediatric injury risk in simulated short-distance falls. Arch. Pediatr. Adolesc. Med. 157, 480–486. doi:10.1001/archpedi.157.5.480

Bessho, M., Ohnishi, I., Matsumoto, T., Ohashi, S., Matsuyama, J., Tobita, K., Kaneko, M., Nakamura, K., 2009. Prediction of proximal femur strength using a CT-based nonlinear finite element method: Differences in predicted fracture load and site with changing load and boundary conditions. Bone 45, 226–231. doi:10.1016/j.bone.2009.04.241

Bessho, M., Ohnishi, I., Okazaki, H., Sato, W., Kominami, H., Matsunaga, S., Nakamura, K., 2004. Prediction of the strength and fracture location of the femoral neck by CT-based finite-element method: A preliminary study on patients with hip fracture. J. Orthop. Sci. 9, 545–550. doi:10.1007/s00776-004-0824-1

Bonnet, V., Mazza, C., Fraisse, P., Cappozzo, A., 2013. Real-time estimate of body kinematics during a planar squat task using a single inertial measurement unit. IEEE Trans. Biomed. Eng. 60, 1920–1926. doi:10.1109/TBME.2013.2245131

Boskey, A.L., Coleman, R., 2010. Critical reviews in oral biology & medicine: Aging and bone. J. Dent. Res. 89, 1333–1348. doi:10.1177/0022034510377791

Boyce, T.M., Bloebaum, R.D., 1993. Cortical aging differences and fracture implications for the human femoral neck. Bone 14, 769–778. doi:10.1016/8756-3282(93)90209-S

Brand, R.A., 2010. Biographical sketch: julius wolff, 1836-1902. Clin. Orthop. Relat. Res. 468, 1047–1049. doi:10.1007/s11999-010-1258-z

Büchler, P., Ramaniraka, N.A., Rakotomanana, L.R., Iannotti, J.P., Farron, A., 2002. A finite element model of the shoulder: Application to the comparison of normal and osteoarthritic joints. Clin. Biomech. 17, 630–639. doi:10.1016/S0268-0033(02)00106-7

Bueno, E.M., Glowacki, J., 2011. Biologic Foundations for Skeletal Tissue Engineering. Synth. Lect. Tissue Eng. 3, 1–220. doi:10.2200/S00329ED1V01Y201101TIS007

Caffey, J., 1946. Multiple fractures in the long bones of infants suffering from chronic subdural hematoma. Radiology 194, 163–173. doi:10.1007/s11999-010-1666-0

Carter, D.R., Hayes, W.C.., 1977. The Compressive Behavior Porous of Bone Structure as a Two-Phase Porous Structure. J. Bone Jt. Surg. 59, 954–962. doi:10.1007/978-1-4471-5451-8_116

Carty, H., 1997. Pediatric radiology Review article Non-accidental injury : a review of the radiology. Eur. Radiol. 7, 1365–1367.

Cauley, J.A., Lui, L.Y., Genant, H.K., Salamone, L., Browner, W., Fink, H.A., Cohen, P., Hillier, T., Bauer, D.C., Cummings, S.R., 2009. Risk factors for severity and type of the hip fracture. J. Bone Miner. Res. 24, 943–955. doi:10.1359/jbmr.081246

Cheong, V.S., 2014. Structural failure and fracture of immature bone. Imperial College London A.

Cheong, V.S., Karunaratne, A., Amis, A.A., Bull, A.M.J., 2017. Strain rate dependency of fractures of immature bone. J. Mech. Behav. Biomed. Mater. 66, 68–76. doi:10.1016/j.jmbbm.2016.10.023

Cody, D.D., Gross, G.J., J. Hou, F., Spencer, H.J., Goldstein, S. a., P. Fyhrie, D., 1999. Femoral strength is better predicted by finite element models than QCT and DXA. J. Biomech. 32, 1013–1020. doi:10.1016/S0021-9290(99)00099-8

Cooper, C., Dennison, E.M., Leufkens, H.G.M., Bishop, N., van Staa, T.P., 2004. Epidemiology of childhood fractures in Britain: a study using the general practice research database. J. Bone Miner. Res. 19, 1976–1981. doi:10.1359/JBMR.040902

Courtney, a. C., Wachtel, E.F., Myers, E.R., Hayes, W.C., 1994. Effects of loading rate on strength of the proximal femur. Calcif. Tissue Int. 55, 53–58. doi:10.1007/BF00310169

Cowgill, L.W., Warrener, A., Pontzer, H., Ocobock, C., 2010. Waddling and toddling: The biomechanical effects of an immature gait. Am. J. Phys. Anthropol. 143, 52–61. doi:10.1002/ajpa.21289

Currey, J.D., 1979. Changes in the impact energy absorption of bone with age. J. Biomech. 12, 459–469. doi:10.1016/0021-9290(79)90031-9

Currey, J.D., Brear, K., Zioupos, P., 1996. The effects of ageing and changes in mineral content in degrading the toughness of human femora. J. Biomech. 29, 257–260. doi:10.1016/0021-9290(95)00048-8

Currey, J.D., Butler, G., 1975. The Mechanical Properties of Bone Tissue in Children. J. Bone Jt. Surg. 57–A, 810–814.

Dall'ara, E., Luisier, B., Schmidt, R., Kainberger, F., Zysset, P., Pahr, D., 2012. A nonlinear QCT-based finite element model validation study for the human femur tested in two configurations in vitro. Bone 52, 27–38. doi:10.1016/j.bone.2012.09.006

de Bakker, P.M., Manske, S.L., Ebacher, V., Oxland, T.R., Cripton, P. a., Guy, P., 2009. During sideways falls proximal femur fractures initiate in the superolateral cortex: Evidence from high-speed video of simulated fractures. J. Biomech. 42, 1917–1925. doi:10.1016/j.jbiomech.2009.05.001

Dragomir-Daescu, D., Op Den Buijs, J., McEligot, S., Dai, Y., Entwistle, R.C., Salas, C., Melton, L.J., Bennet, K.E., Khosla, S., Amin, S., 2011. Robust QCT/FEA models of proximal femur stiffness and fracture load during a sideways fall on the hip. Ann. Biomed. Eng. 39, 742–755. doi:10.1007/s10439-010-0196-y

Duboeuf, F., Hans, D., Schott, A.M., Kotzki, P.O., Favier, F., Marcelli, C., Meunier, P.J., Delmas, P.D., 1997. Different morphometric and densitometric parameters predict cervical and trochanteric hip fracture: The EPIDOS study. J. Bone Miner. Res. 12, 1895–1902. doi:10.1359/jbmr.1997.12.11.1895

Duda, G.N., Schneider, E., Chao, E.Y.S., 1997. Internal forces and moments in the femur during walking. J. Biomech. 30, 933–941. doi:10.1016/S0021-9290(97)00057-2

Duda, G.N.G.N., Heller, M., Albinger, J., Schulz, O., Schneider, E., Claes, L., 1998. Influence of muscle forces on femoral strain distribution. J. Biomech. 31, 841–846. doi:10.1016/S0021-9290(98)00080-3

European Communities, 2018. Population structure and ageing [WWW Document]. doi:http://ec.europa.eu/eurostat/statistics-explained/index.php/Population_structure_and_ageing

Evans, F.G., 1976. Mechanical properties and histology of cortical bone from younger and older men. Anat. Rec. 185, 1–11. doi:10.1002/ar.1091850102

Falcinelli, C., Schileo, E., Balistreri, L., Baruffaldi, F., Bordini, B., Viceconti, M., Albisinni, U., Ceccarelli, F., Milandri, L., Toni, A., Taddei, F., 2014. Multiple loading conditions analysis can improve the association between finite element bone strength estimates and proximal femur fractures: A preliminary study in elderly women. Bone 67, 71–80. doi:10.1016/j.bone.2014.06.038

Favre, P., Snedeker, J.G., Gerber, C., 2009. Numerical modelling of the shoulder for clinical applications. Philos. Trans. R. Soc. A Math. Phys. Eng. Sci. 367, 2095–2118. doi:10.1098/rsta.2008.0282

Ford, C.M., Keaveny, T.M., Hayes, W.C., 1996. The effect of impact direction on the structural capacity of the proximal femur during falls. J. Bone Miner. Res. 11, 377–383. doi:10.1002/jbmr.5650110311

Forman, J.L., Dios, P. De, Symeonidis, I., Duart, J., Kerrigan, J.R., Salzar, R.S., Balasubramanian, S., Gomez, M.S., Kent, R.W., 2012. Fracture Tolerance Related to Skeletal Development and Aging Throughout Life: 3-Point Bending of Human Femurs. IRCOBI Conf. 524–539. doi:10.1002/mrm.10658

Gallagher, J.C., Melton, L.J., Riggs, B.L., Bergstrath, E., 1980. Epidemiology of fractures of the proximal femur in Rochester, Minnesota. Clin Orthop Relat Res 150, 163–171.

Geusens, P., Van Geel, T., Van Den Bergh, J., 2010. Can hip fracture prediction in women be estimated beyond bone mineral density measurement alone? Ther. Adv. Musculoskelet. Dis. 2, 63–77. doi:10.1177/1759720X09359541

Gosman, J.H., Hubbell, Z.R., Shaw, C.N., Ryan, T.M., 2013. Development of Cortical Bone Geometry in the Human Femoral and Tibial Diaphysis. Anat. Rec. 296, 774–787. doi:10.1002/ar.22688

Grassi, L., Schileo, E., Taddei, F., Zani, L., Juszczyk, M., Cristofolini, L., Viceconti, M., 2012. Accuracy of finite element predictions in sideways load configurations for the proximal human femur. J. Biomech. 45, 394–399. doi:10.1016/j.jbiomech.2011.10.019

Gray, D.J., Gardner, E., 1969. The prenatal development of the human humerus. Am. J. Anat. 124, 431–445. doi:10.1002/aja.1001240403

Greenspan, S.L., Myers, E.R., Maitland, L.A., Kido, T.H., Krasnow, M.B., Hayes, W.C., 1994. Trochanteric bone mineral density is associated with type of hip fracture in the elderly. J Bone Min. Res 9, 1889–1894. doi:10.1002/jbmr.5650091208

Hadjidakis, D.J., Androulakis, I.I., 2006. Bone remodeling. Ann. N. Y. Acad. Sci. 1092, 385–396. doi:10.1196/annals.1365.035

Haider, I.T., Speirs, A.D., Frei, H., 2013. Effect of boundary conditions, impact loading and hydraulic stiffening on femoral fracture strength. J. Biomech. 46, 2115–2121. doi:10.1016/j.jbiomech.2013.07.004

Hambli, R., Benhamou, C.L., Jennane, R., Lespessailles, E., Skalli, W., Laporte, S., Laredo, J.D., Bousson, V., Zarka, J., 2013. Combined finite element model of human proximal femur behaviour considering remodeling and fracture. Irbm 34, 191–195. doi:10.1016/j.irbm.2013.01.011

Hansman, C.E., 1962. Apperance and fusion of ossification centres in the human skelaton. Am. J. Roentgenol. 88, 476–482.

Hayes, W.C., Myers, E.R., Morris, J.N., Gerhart, T.N., Yett, H.S., Lipsitz, L. a, 1993. Impact near the hip dominates fracture risk in elderly nursing home residents who fall. Calcif. Tissue Int. 52, 192–198. doi:10.1007/BF00298717

Helgason, B., Taddei, F., Pálsson, H., Schileo, E., Cristofolini, L., Viceconti, M., Brynjólfsson, S., 2008. A modified method for assigning material properties to FE models of bones. Med. Eng. Phys. 30, 444–453. doi:10.1016/j.medengphy.2007.05.006

Herman-Giddens, M.E., Brown, G., Verbiest, S., Carlson, P.J., Hooten, E.G., Howell, E., Butts, J.D., 1999. Underascertainment of child abuse mortality in the United States. JAMA 282, 463–467. doi:10.1001/jama.282.5.463

Hirsch, C., Evans, F., 1965. Studies on some physical properties of infant compact bone. Acta Orthop. Scand. 503, 300–313. doi:10.3109/17453676508989361

Huiskes, R., Chao, E.Y.S., 1983. A survey of finite element analysis in orthopedic biomechanics:

The first decade. J. Biomech. 16, 385–409. doi:10.1016/0021-9290(83)90072-6

Hymel, P.K., Jenny, C., 1996. Abusive Spiral Fractures of the Humerus: A Videotaped Exception. Arch Pediatr Adoles Med 150, 226–228.

Ibrahim, N.G., Margulies, S.S., 2010. Biomechanics of the toddler head during low-height falls: an anthropomorphic dummy analysis. J. Neurosurg. Pediatr. 6, 57–68. doi:10.3171/2010.3.PEDS09357

Ivarsson, B., Crandall, J., Longhitano, D., Okamoto, M., 2004. Lateral Injury Criteria for the 6-year-old Pedestrian – Part II: Criteria for the Upper and Lower Extremities, in: SAE World Congress. pp. 1–19. doi:10.4271/2004-01-0323

Jayakumar, P., Barry, M., Ramachandran, M., 2010. Orthopaedic aspects of paediatric non-accidental injury. J. Bone Joint Surg. Br. 92, 189–95. doi:10.1302/0301-620X.92B2.22923

Jee, W.S.S., 2001. Integrated Bone Tissue Physiology: Anatomy and Physiology, in: Cowin, S.C. (Ed.), Bone Mechanics Handbook. CRC Press LLC, pp. 1–24. doi:10.1016/0268-0033(90)90036-6

Jenny, C., 2014. A possible mechanism for accidental humeral fractures in infants. Pediatr. Radiol. 44, 1218–1218. doi:10.1007/s00247-014-3098-6

Johnell, O., Kanis, J., 2005. Epidemiology of osteoporotic fractures. Osteoporos. Int. 16, 6–10. doi:10.1007/s00198-004-1702-6

Kaneko, T.S., Pejcic, M.R., Tehranzadeh, J., Keyak, J.H., 2003. Relationships between material properties and CT scan data of cortical bone with and without metastatic lesions. Med. Eng. Phys. 25, 445–454. doi:10.1016/S1350-4533(03)00030-4

Kanis, J.A., Harvey, N.C., Johansson, H., Odén, A., McCloskey, E. V., Leslie, W.D., 2017. Overview of Fracture Prediction Tools. J. Clin. Densitom. 20, 444–450. doi:10.1016/j.jocd.2017.06.013

Keller, T.S., 1994. Predicting the compressive mechanical behavior of bone. J. Biomech. 27, 1159–1168. doi:10.1016/0021-9290(94)90056-6

Kerrigan, J.R., Bhalla, K.S., Madeley, N.J., Funk, J.R., Bose, D., Crandall, J.R., 2003. Experiments for Establishing Pedestrian-Impact Lower Limb Injury Criteria, in: SAE World Congress.

doi:10.4271/2003-01-0895

Keyak, J.H., 2001. Improved prediction of proximal femoral fracture load using nonlinear finite element models. Med. Eng. Phys. 23, 165–73.

Keyak, J.H., Kaneko, T.S., Tehranzadeh, J., Skinner, H.B., 2005. Predicting proximal femoral strength using structural engineering models. Clin. Orthop. Relat. Res. 219–228. doi:10.1097/01.blo.0000164400.37905.22

Keyak, J.H., Rossi, S. a, Jones, K. a, Skinner, H.B., 1997. Prediction of Femoral Fracture Load using Automated Finite Element Modelling. J Biomech 31, 125–133. doi:10.1016/S0021-9290(97)00123-1

Keyak, J.H., Sigurdsson, S., Karlsdottir, G., Oskarsdottir, D., Sigmarsdottir, a., Zhao, S., Kornak, J., Harris, T.B., Sigurdsson, G., Jonsson, B.Y., Siggeirsdottir, K., Eiriksdottir, G., Gudnason, V., Lang, T.F., 2011. Male-female differences in the association between incident hip fracture and proximal femoral strength: A finite element analysis study. Bone 48, 1239–1245. doi:10.1016/j.bone.2011.03.682

Keyak, J.H., Sigurdsson, S., Karlsdottir, G.S., Oskarsdottir, D., Sigmarsdottir, a., Kornak, J., Harris, T.B., Sigurdsson, G., Jonsson, B.Y., Siggeirsdottir, K., Eiriksdottir, G., Gudnason, V., Lang, T.F., 2013. Effect of finite element model loading condition on fracture risk assessment in men and women: The AGES-Reykjavik study. Bone 57, 18–29. doi:10.1016/j.bone.2013.07.028

Keyak, J.H., Skinner, H.B., Fleming, J. a., 2001. Effect of force direction on femoral fracture load for two types of loading conditions. J. Orthop. Res. 19, 539–544. doi:10.1016/S0736-0266(00)00046-2

King, J., Diefendorf, D., Apthorp, J., Negrete, V.F., Carlson, M., 1988. Analysis of 429 fractures in 189 battered children. J. Pediatr. Orthop. 8, 585–589.

Kleinman, P.K., Perez-Rossello, J.M., Newton, A.W., Feldman, H.A., Kleinman, P.L., 2011. Prevalence of the classic metaphyseal lesion in infants at low versus high risk for abuse. Am. J. Roentgenol. 197, 1005–1008. doi:10.2214/AJR.11.6540

Koivumäki, J.E.M., Thevenot, J., Pulkkinen, P., Kuhn, V., Link, T.M., Eckstein, F., Jämsä, T., 2012.

Ct-based finite element models can be used to estimate experimentally measured failure loads in the proximal femur. Bone 50, 824–829. doi:10.1016/j.bone.2012.01.012

Kopperdahl, D.L., Aspelund, T., Hoffmann, P.F., Sigurdsson, S., Siggeirsdottir, K., Harris, T.B., Gudnason, V., Keaveny, T.M., 2014. Assessment of incident spine and hip fractures in women and men using finite element analysis of CT scans. J Bone Min. Res 29, 570–580. doi:10.1002/jbmr.2069

Kowal-Vern, A., Paxton, T.P., Ros, S.P., Lietz, H., Fitzgerald, M., Gamelli, R.L., 1992. Fractures in the Under-3-Year-Old Age Cohort. Clin. Pediatr. (Phila). 31, 653–659. doi:10.1177/000992289203101103

Kress, T., Porta, D., Snider, J., Fuller, P., Paihogios, J., Heck, W., Frick, S., Wasserman, J., 1995. Fracture patterns of human cadaver long bones, in: International Research Counsel on the Biomechanics of Impact. pp. 155–169.

Kuhns, L., Finnstorm, O., 1976. New standers of ossification of the newborn. Radiology 119, 655–660.

Latella, C., Kuppuswamy, N., Romano, F., Traversaro, S., Nori, F., 2016. Whole-body human inverse dynamics with distributed micro-accelerometers, gyros and force sensing. Sensors (Switzerland) 16, 1–17. doi:10.3390/s16050727

Leal, J., Gray, a. M., Prieto-Alhambra, D., Arden, N.K., Cooper, C., Javaid, M.K., Judge, A., 2015. Impact of hip fracture on hospital care costs: a population-based study. Osteoporos. Int. 27, 549–558. doi:10.1007/s00198-015-3277-9

Lefèvre, E., Lasaygues, P., Baron, C., Payan, C., Launay, F., Follet, H., Pithioux, M., 2015. Analyzing the anisotropic Hooke's law for children's cortical bone. J. Mech. Behav. Biomed. Mater. 49, 370–377. doi:10.1016/j.jmbbm.2015.05.013

Leventhal, J.M., 1999. The challenges of recognizing child abuse: Seeing is believing. J. Am. Med. Assoc. 281, 657–659. doi:10.1001/jama.281.7.657

Li, X., Viceconti, M., Cohen, M.C., Reilly, G.C., Carre, M.J., Offiah, A.C., 2015. Developing CT based computational models of pediatric femurs. J. Biomech. 48, 2034–2040. doi:10.1016/j.jbiomech.2015.03.027

Loder, R.T., Bookout, C., 1991. Fracture Patterns in Battered Children. J. Orthop. Trauma 5, 428–433. doi:10.1097/00005131-199112000-00007

Loder, R.T., O'Donnell, P.W., Feinberg, J.R., 2006. Epidemiology and mechanisms of femur fractures in children. J. Pediatr. Orthop. 26, 561–566. doi:10.1097/01.bpo.0000230335.19029.ab

Lotz, J.C., Cheal, E.J., Hayes, W.C., 1995. Stress distributions within the proximal femur during gait and falls: Implications for osteoporotic fracture. Osteoporos. Int. 5, 252–261. doi:10.1007/BF01774015

Lotz, J.C., Cheal, E.J., Hayes, W.C., 1991. Fracture prediction for the proximal femur using finite element models: Part I--Linear analysis. J Biomech Eng 113, 353–360.

Lotz, J.C., Cheal, E.J., Hayes, W.C., 1991. Fracture Prediction for the Proximal Femur Using Finite Element Models: Part II—Nonlinear Analysis. J. Biomech. Eng. 113, 361–365. doi:10.1115/1.2895413

Lotz, J.C., Hayes, W.C., 1990. The use of quantitative computed tomography to estimate risk of fracture of the hip from falls Use of Quantitative to Estimate Computed Risk Tomography of Fracture of the Hip from. J. Bone Jt. Surg. 72, 689–700.

Majumder, S., Roychowdhury, A., Pal, S., 2009. Effects of body configuration on pelvic injury in backward fall simulation using 3D finite element models of pelvis-femur-soft tissue complex. J. Biomech. 42, 1475–1482. doi:10.1016/j.jbiomech.2009.03.044

Marieb, E.N., Wilhelm, P.B., Mallatt, J., 2016. Human Anatomy, 8th ed. Pearson. doi:10.1016/j.mrgentox.2012.03.010

Martin, R.B., Burr, D.B., Sharkey, N.A., Fyhrie, D.P., 2015. Growth, Modeling and Remodeling of Bone, in: Skeletal Tissue Mechanics. Springer, pp. 95–173.

Martin, R.B., Ishida, J., 1989. The relative effects of collagen fiber orientation, porosity, density, and mineralization on bone strength. J. Biomech. 22, 419–426. doi:10.1016/0021-9290(89)90202-9

Mayhew, P.M., Thomas, C.D., Clement, J.G., Loveridge, N., Beck, T.J., Bonfield, W., Burgoyne, C.J., Reeve, J., 2005. Relation between age, femoral neck cortical stability, and hip

fracture risk. Lancet 366, 129–135. doi:10.1016/S0140-6736(05)66870-5

McCreadie, B.R., Goldstein, S.A., 2000. Biomechanics of fracture: Is bone mineral density sufficient to assess risk? J. Bone Miner. Res. 15, 2305–2308. doi:10.1359/jbmr.2000.15.12.2305

Melton, L.J., Chrischilles, E.A., Cooper, C., Lane, A.W., Riggs, B.L., 1992. How Many Women Have Osteoporosis ? J. Bone Miner. Res. 7, 1005–1010. doi:10.1359/jbmr.2005.20.5.886

Menees, T., Holly, L., 1932. The Ossification in the Extremities of the New-Born. Am J Roentgnol 28, 389–390.

Meng, Y., Pak, W., Guleyupoglu, B., Koya, B., Gayzik, F.S., Untaroiu, C.D., 2017. A finite element model of a six-year-old child for simulating pedestrian accidents. Accid. Anal. Prev. 98, 206–213. doi:10.1016/j.aap.2016.10.002

Merten, D.F., Radkowski, M.A., Leonidas, J.C., 1983. The abused child: a radiological reappraisal. Radiology 146, 377–381. doi:10.1148/radiology.146.2.6849085

Miltner, E., Kallieris, D., 1989. Quasi-static and dynamic bending stress of the pediatric femur for producing a femoral fracture. Zeitschrift fur Rechtsmedizin J. Leg. Med. 102, 535–544.

Morgan, E.F., Bayraktar, H.H., Keaveny, T.M., 2003. Trabecular bone modulus-density relationships depend on anatomic site. J. Biomech. 36, 897–904. doi:10.1016/S0021-9290(03)00071-X

Moyad, M. a., 2003. Osteoporosis: A rapid review of risk factors and screening methods. Urol. Oncol. Semin. Orig. Investig. 21, 375–379. doi:10.1016/S1078-1439(03)00140-6

Mueller, K.H., Trias, A., Ray, R.D., 1966. Bone density and compostiton. Age-related and pathological changes in water and mineral content. J Bone Jt. Surg 48(1), 140–148.

Nahum, A., Melvin, J., 2002. Accidental Injury, Springer New York. doi:10.1007/978-1-4757-2264-2

Nakamura, N., Kyou, T., Takaoka, K., Ohzono, K., Ono, K., 1992. Bone mineral density in the proximal femur and hip fracture type in the elderly. J. Bone Miner. Res. 7, 755–759. doi:10.1002/jbmr.5650070705

Nieves, J.W., Bilezikian, J.P., Lane, J.M., Einhorn, T.A., Wang, Y., Steinbuch, M., Cosman, F., 2010. Fragility fractures of the hip and femur: Incidence and patient characteristics. Osteoporos. Int. 21, 399–408. doi:10.1007/s00198-009-0962-6

Nishiyama, K.K., Gilchrist, S., Guy, P., Cripton, P., Boyd, S.K., 2013. Proximal femur bone strength estimated by a computationally fast finite element analysis in a sideways fall configuration. J. Biomech. 46, 1231–1236. doi:10.1016/j.jbiomech.2013.02.025

Nishiyama, K.K., Ito, M., Harada, a., Boyd, S.K., 2014. Classification of women with and without hip fracture based on quantitative computed tomography and finite element analysis. Osteoporos. Int. 25, 619–626. doi:10.1007/s00198-013-2459-6

Norton, M.R., Gamble, C., 2001. Bone classification: an objective scale of bone density using the computerized tomography scan. Clin. Oral Implants Res. 12, 79–84. doi:10.1034/j.1600-0501.2001.012001079.x

Ogden, J.A., 1984. The uniqueness of growing bones, in: Fractures in Children. Philadelphia, PA, Lippincott, pp. 1–86.

Öhman, C., Baleani, M., Pani, C., Taddei, F., Alberghini, M., Viceconti, M., Manfrini, M., 2011. Compressive behaviour of child and adult cortical bone. Bone 49, 769–776. doi:10.1016/j.bone.2011.06.035

Orwoll, E.S., Marshall, L.M., Nielson, C.M., Cummings, S.R., Lapidus, J., Cauley, J. a, Ensrud, K., Lane, N., Hoffmann, P.R., Kopperdahl, D.L., Keaveny, T.M., 2009. Finite element analysis of the proximal femur and hip fracture risk in older men. J. Bone Miner. Res. 24, 475–483. doi:10.1359/jbmr.081201

Ott, S.M., 1990. Editorial: Attainment of peak bone mass. J. Clin. Endocrinol. Metab. 71, 1082A–1082C. doi:10.1210/jcem-71-5-1082

Ouyang, J., Zhu, Q., Zhao, W., Xu, Y., Chen, W., Zhong, S., 2003. Biomechanical Character of Extremity Long Bones in Children and Its Significance. Chinese J. Clin. Anat. 21, 620–623. doi:10.1017/CBO9781107415324.004

Pal, S., 2014. Mechanical properties of biological materials, in: Design of Artificial Human Joints & Organs. Springer Science+Business Media New York, pp. 32–31.

doi:10.1007/978-1-4614-6255-2

Parker, M., Johansen, A., 2006. Hip fracture. BMJ 333, 27–30. doi:10.1136/bmj.333.7557.27

Pearce, A.I., Richards, R.G., Milz, S., Schneider, E., Pearce, S.G., 2007. Animal models for implant biomaterial research in bone: A review. Eur. Cells Mater. 13, 1–10. doi:10.22203/eCM.v013a01

Peng, L., Bai, J., Zeng, X., Zhou, Y., 2006. Comparison of isotropic and orthotropic material property assignments on femoral finite element models under two loading conditions. Med. Eng. Phys. 28, 227–233. doi:10.1016/j.medengphy.2005.06.003

Pierce, M.C., Bertocci, G., 2008. Injury Biomechanics and Child Abuse. Annu. Rev. Biomed. Eng. 10, 85–106. doi:10.1146/annurev.bioeng.9.060906.151907

Pierce, M.C., Bertocci, G.E., Vogeley, E., Moreland, M.S., 2004. Evaluating long bone fractures in children: A biomechanical approach with illustrative cases. Child Abus. Negl. 28, 505–524. doi:10.1016/j.chiabu.2003.01.001

Pierce, M.C., Valdevit, A., Anderson, L., Inoue, N., 2000. Biomechanical Evaluation of Dual-Energy X-Ray Absorptiometry for Predicting Fracture Loads of the Infant Femur for Injury Investigation: An In Vitro Porcine Model. J. Orthop. Trauma 14, 571–576.

Pinilla, T.P., Boardman, K.C., Bouxsein, M.L., Myers, E.R., Hayes, W.C., 1996. Impact direction from a fall influences the failure load of the proximal femur as much as age-related bone loss. Calcif. Tissue Int. 58, 231–235. doi:10.1007/s002239900040

Pottecher, P., Engelke, K., Duchemin, L., Museyko, O., Moser, T., Mitton, D., Vicaut, E., Adams, J., Skalli, W., Laredo, J.D., Bousson, V., 2016. Prediction of Hip Failure Load: In Vitro Study of 80 Femurs Using Three Imaging Methods and Finite Element Models—The European Fracture Study (EFFECT). Radiology 280, 837–847. doi:10.1148/radiol.2016142796

Qasim, M., Farinella, G., Zhang, J., Li, X., Yang, L., Eastell, R., Viceconti, M., 2016. Patient-specific finite element estimated femur strength as a predictor of the risk of hip fracture: the effect of methodological determinants. Osteoporos. Int. 27, 2815–2822. doi:10.1007/s00198-016-3597-4

Rajagopal, A., Dembia, C., DeMers, M., Delp, D., Hicks, J., Delp, S., 2016. Full body

musculoskeletal model for muscle-driven simulation of human gait. IEEE Trans. Biomed. Eng. 63, 2068–2079. doi:10.1109/TBME.2016.2586891

Rennie, L., Court-Brown, C.M., Mok, J.Y.Q., Beattie, T.F., 2007. The epidemiology of fractures in children. Injury 38, 913–922. doi:10.1016/j.injury.2007.01.036

Resnick, B. (Ed.), 2004. Restorative Care Nursing for Older Adults: A Guide for All Care Settings. Springer, New York.

Rex, C., Kay, P.R., 2000. Features of femoral fractures in nonaccidental injury. J. Pediatr. Orthop. 20, 411–413. doi:10.1097/00004694-200005000-00028

Riggs, B.L., Wahner, H.W., Seeman, E., Offord, K.P., Dunn, W.L., Mazess, R.B., Johnson, K. a., Melton, L.J., 1982. Changes in bone mineral density of the proximal femur and spine with aging. Differences between the postmenopausal and senile osteoporosis syndromes. J. Clin. Invest. 70, 716–723.

Rodríguez, J.I., Palacios, J., García-Alix, A., Pastor, I., Paniagua, R., 1988. Effects of immobilization on fetal bone development. A morphometric study in newborns with congenital neuromuscular diseases with intrauterine onset. Calcif. Tissue Int. 43, 335–339. doi:10.1007/BF02553275

Rosado, N., 2014. Incorrect postulate regarding humeral fractures in non-ambulant infants. Pediatr. Radiol. 44, 1332. doi:10.1007/s00247-014-3124-8

Ross, P.D., Norimatsu, H., Davis, J.W., Yano, K., Wasnich, R.D., Fujiwara, S., Hosoda, Y., Melton, L.J., 1991. A comparison of hip fracture incidence among native Japanese, Japanese Americans, and American Caucasians. Am. J. Epidemiol. 133, 801–809. doi:10.1093/oxfordjournals.aje.a115959

Rossman, T., Kushvaha, V., Dragomir-Daescu, D., 2015. QCT/FEA predictions of femoral stiffness are strongly affected by boundary condition modeling. Comput. Methods Biomech. Biomed. Engin. 19, 208–216. doi:10.1080/10255842.2015.1006209

Rubin, K.H., Friis-Holmberg, T., Hermann, A.P., Abrahamsen, B., Brixen, K., 2013. Risk assessment tools to identify women with increased risk of osteoporotic fracture: Complexity or simplicity? A systematic review. J. Bone Miner. Res. 28, 1701–1717.

doi:10.1002/jbmr.1956

Ryan, T.M., Krovitz, G.E., 2006. Trabecular bone ontogeny in the human proximal femur. J. Hum. Evol. 51, 591–602. doi:10.1016/j.jhevol.2006.06.004

Saint-Georges, P., Warzee, G., Beauwens, R., Notay, Y., 1996. High-performance PCG solvers for FEM structural analysis. Int. J. Numer. Methods Eng. 39, 1313–1340. doi:10.1002/(SICI)1097-0207(19960430)39:8<1313::AID-NME906>3.0.CO;2-J

Scherl, S. a, Miller, L., Lively, N., Russinoff, S., Sullivan, C.M., Tornetta, P., 2000. Accidental and nonaccidental femur fractures in children. Clin. Orthop. Relat. Res. 83, 96–105.

Scheuer, L., Black, S., Christie, A., 2000. Developmental Juvenile Osteology, 1st ed, Developmental Juvenile Osteology. Elsevier. doi:10.1016/B978-012624000-9/50015-0

Schileo, E., Dall'Ara, E., Taddei, F., Malandrino, A., Schotkamp, T., Baleani, M., Viceconti, M., 2008a. An accurate estimation of bone density improves the accuracy of subject-specific finite element models. J. Biomech. 41, 2483–2491. doi:10.1016/j.jbiomech.2008.05.017

Schileo, E., Taddei, F., Cristofolini, L., Viceconti, M., 2008b. Subject-specific finite element models implementing a maximum principal strain criterion are able to estimate failure risk and fracture location on human femurs tested in vitro. J. Biomech. 41, 356–367. doi:10.1016/j.jbiomech.2007.09.009

Schileo, E., Taddei, F., Malandrino, A., Cristofolini, L., Viceconti, M., 2007. Subject-specific finite element models can accurately predict strain levels in long bones. J. Biomech. 40, 2982–2989. doi:10.1016/j.jbiomech.2007.02.010

Shen, M., Zhu, F., Mao, H., Fan, H., Mone, N., Sanghavi, V., Kalra, A., Jin, X., Chou, C.C., Yang, K.H., Shen, M., Zhu, F., Sanghavi, N., Kalra, V., Chou, X., Yang, C.C., 2015. Finite element modelling of 10-year-old child pelvis and lower extremities with growth plates for pedestrian protection. Int. J. Veh. Saf. J. Veh. Saf. 8, 263–286. doi:10.1504/IJVS.2015.070788

Sherker, S., Ozanne-Smith, J., Rechnitzer, G., Grzebieta, R., 2003. Development of a multidisciplinary method to determine risk factors for arm fracture in falls from playground equipment. Inj. Prev. 9, 279–283. doi:10.1136/ip.9.3.279

Singleton, R., 2010. The chief adviser on the safety of children, First annual report to the parliament -2010.

Slaughter, W., Petrolito, J., 2002. Constitutive Equations, in: Linearized Theory of Elasticity. Birkhäuser Basel, pp. 193–220. doi:10.1115/1.1497478

Smith, R.W., Walker, R.R., 1964. Femoral Expansion In Aging Women: Implications For Osteoporosis And Fractures. Science (80-.). 145, 156–157. doi:10.1126/SCIENCE.145.3628.156

Somers, J.M., Halliday, K.E., Chapman, S., 2014. Humeral fracture in non-ambulant infants: a possible accidental mechanism. Pediatr. Radiol. 44, 1219–1223. doi:10.1007/s00247-014-2954-8

Spencer, B.Y., 1974. Traumatic bowing of the forearm in children. J. Bone Jt. Surg. 56–A, 611–616.

Steven, L.F., Eric, T.J., 2009. Skeletal growth, development, and healing as related to pediatric trauma, in: Green, N., Swiontkowski, M. (Eds.), Skeletal Trauma in Children. Philadelphia, PA : Saunders/Elsevier, pp. 1–18. doi:10.1016/B978-1-4160-4900-5.10004-4

Taddei, F., Cristofolini, L., Martelli, S., Gill, H.S., Viceconti, M., 2006. Subject-specific finite element models of long bones: An in vitro evaluation of the overall accuracy. J. Biomech. 39, 2457–2467. doi:10.1016/j.jbiomech.2005.07.018

Taddei, F., Palmadori, I., Taylor, W.R., Heller, M.O., Bordini, B., Toni, A., Schileo, E., 2014. Safety factor of the proximal femur during gait: a population-based finite element study Article. J. Biomech. 47, 3433–3440. doi:10.1016/j.jbiomech.2014.08.030

Taddei, F., Pancanti, A., Viceconti, M., 2004. An improved method for the automatic mapping of computed tomography numbers onto finite element models. Med. Eng. Phys. 26, 61–69. doi:10.1016/S1350-4533(03)00138-3

Tamburini, P., Storm, F., Buckley, C., Bisi, M.C., Stagni, R., Mazzà, C., 2018. Moving from laboratory to real life conditions: Influence on the assessment of variability and stability of gait. Gait Posture 59, 248–252. doi:10.1016/j.gaitpost.2017.10.024

Taylor, W.R., Roland, E., Ploeg, H., Hertig, D., Klabunde, R., Warner, M.D., Hobatho, M.C.,

Rakotomanana, L., Clift, S.E., 2002. Determination of orthotropic bone elastic constants using FEA and modal analysis. J. Biomech. 35, 767–773. doi:10.1016/S0021-9290(02)00022-2

Theobald, P.S., Qureshi, A., Jones, M.D., 2012. Biomechanical investigation into the torsional failure of immature long bone. J. Clin. Orthop. Trauma 3, 24–27. doi:10.1016/j.jcot.2012.02.001

Thomas, S., Rosenfield, N., Leventhal, J., Markowitz, R., 1991. Long-Bone Fracturesin YoungChildren : Distinguishing AccidentalInjuriesFrom ChildAbuse 88, 471–476.

Tortora, G.J., Grabowski, S.R., 2003. Principles of Anatomy and Physiology, 10th ed, Jone Wiley & Sons, Inc.

Tsai, A., Coats, B., Kleinman, P.K., 2017. Biomechanics of the classic metaphyseal lesion: finite element analysis. Pediatr. Radiol. 47, 1622–1630. doi:10.1007/s00247-017-3921-y

Turner, C.H., Burr, D.B., 1993. Basic biomechanical measurements of bone: A tutorial. Bone 14, 595–608. doi:10.1016/8756-3282(93)90081-K

Turner, C.H., Rho, J., Takano, Y., Tsui, T.Y., Pharr, G.M., 1999. The elastic properties of trabecular and cortical bone tissues are similar: Results from two microscopic measurement techniques. J. Biomech. 32, 437–441. doi:10.1016/S0021-9290(98)00177-8

van den Kroonenberg, A., Munih, P., Weigent-Hayes, M., McMahon, T., 1992. Hip impact velocities and body configrations for experemental falls from standing height. ORS 24.

Van Den Munckhof, S., Zadpoor, A.A., 2014. How accurately can we predict the fracture load of the proximal femur using finite element models? Clin. Biomech. 29, 373–380. doi:10.1016/j.clinbiomech.2013.12.018

Vega, E., Mautalen, C., Gomez, H., Garrido, A., Melo, L., Sahores, A.O., 1991. Bone mineral density in patients with cervical and trochanteric fractures of the proximal femur. Osteoporos Int 1, 81–86.

Verhulp, E., van Rietbergen, B., Huiskes, R., 2008. Load distribution in the healthy and osteoporotic human proximal femur during a fall to the side. Bone 42, 30–35.

doi:10.1016/j.bone.2007.08.039

Viceconti, M., 2012. Multiscale Modelling of the Skeletal System. Cambridge University Press, New York.

Viceconti, M., Bellingeri, L., Cristofolini, L., Toni, A., 1998. A comparative study on different methods of automatic mesh generation of human femurs. Med. Eng. Phys. 20, 1–10. doi:10.1016/S1350-4533(97)00049-0

Viceconti, M., Hunter, P., Hose, R., 2015. Big Data, Big Knowledge: Big Data for Personalized Healthcare. IEEE J. Biomed. Heal. Informatics 19, 1209–1215. doi:10.1109/JBHI.2015.2406883

Viceconti, M., Qasim, M., Bhattacharya, P., Li, X., 2018. Are CT-Based Finite Element Model Predictions of Femoral Bone Strengthening Clinically Useful ? Curr. Osteoporos. Rep. 16, 216–223.

Wainwright, S.A., Marshall, L.M., Ensrud, K.E., Cauley, J.A., Black, D.M., Hillier, T.A., Hochberg, M.C., Vogt, M.T., Orwoll, E.S., 2005. Hip fracture in women without osteoporosis. J. Clin. Endocrinol. Metab. 90, 2787–2793. doi:10.1210/jc.2004-1568

Wendlova, J., 2008. Bone quality. Elasticity and strength. Bratislava Med. J. 109, 383–386.

Wirtz, D.C., Pandorf, T., Portheine, F., Radermacher, K., Schiffers, N., Prescher, A., Weichert, D., Niethard, F.U., 2003. Concept and development of an orthotropic FE model of the proximal femur. J. Biomech. 36, 289–293. doi:10.1016/S0021-9290(02)00309-3

World Health organization, 1994. Assessment of fracture risk and its implication to screening for postmenopausal osteoporosis Technical Report Series 843.

Worlock, P., Stower, M., Barbor, P., 1986. Patterns of fractures in accidental and non-accidental injury in children: A comparative study. Br. Med. J. (Clin. Res. Ed). 293, 100–102. doi:10.1136/bmj.293.6539.100

Wriggers, P., 2007. Computational Contact Mechanics, 1st ed. John Wiley & Sons Ltd.

Wu, G., Siegler, S., Allard, P., Kirtley, C., Leardini, A., Rosenbaum, D., Whittle, M., D'Lima, D.D., Cristofolini, L., Witte, H., Schmid, O., Stokes, I., 2002. ISB recommendation on definitions of joint coordinate system of various joints for the reporting of human joint motion—

part I: ankle, hip, and spine. J. Biomech. 35, 543–548. doi:10.1016/S0021-9290(01)00222-6

Yadav, P., Shefelbine, S.J., Pontén, E., Gutierrez-Farewik, E.M., 2017. Influence of muscle groups' activation on proximal femoral growth tendency. Biomech. Model. Mechanobiol. 1–15. doi:10.1007/s10237-017-0925-3

Zani, L., Erani, P., Grassi, L., Taddei, F., Cristofolini, L., 2015. Strain distribution in the proximal Human femur during in vitro simulated sideways fall. J. Biomech. 1–14. doi:10.1016/j.jbiomech.2015.02.022

Zannoni, C., Mantovani, R., Viceconti, M., 1998. Material properties assignment to finite element models of bone structures: a new method. Med. Eng. Phys. 20, 735–740. doi:S1350453398000812 [pii]

Zebaze, R.M.D., Jones, A., Welsh, F., Knackstedt, M., Seeman, E., 2005. Femoral neck shape and the spatial distribution of its mineral mass varies with its size: Clinical and biomechanical implications. Bone 37, 243–252. doi:10.1016/j.bone.2005.03.019

Zheng, M., Zou, Z., Bartolo, P. jorge D. silva, Peach, C., Ren, L., 2017. Finite element models of the human shoulder complex: a review of their clinical implications and modelling techniques. Int. j. numer. method. biomed. eng. 33. doi:10.1002/cnm.2777

Zhong, Z.-H., 1993. Finite element procedures for contact-impact problems, Oxford science publications.

Zysset, P., Pahr, D., Engelke, K., Genant, H.K., McClung, M.R., Kendler, D.L., Recknor, C., Kinzl, M., Schwiedrzik, J., Museyko, O., Wang, A., Libanati, C., 2015. Comparison of proximal femur and vertebral body strength improvements in the FREEDOM trial using an alternative finite element methodology. Bone 81, 122–130. doi:10.1016/j.bone.2015.06.025

Zysset, P.K., Dall'Ara, E., Varga, P., Pahr, D.H., 2013. Finite element analysis for prediction of bone strength. Bonekey Rep. 2, 1–9. doi:10.1038/bonekey.2013.120

Zysset, P.K., Edward Guo, X., Edward Hoffler, C., Moore, K.E., Goldstein, S.A., 1999. Elastic modulus and hardness of cortical and trabecular bone lamellae measured by

nanoindentation in the human femur. J. Biomech. 32, 1005–1012. doi:10.1016/S0021-9290(99)00111-6

APPENDIX A

The following two tables are related to the results of the Study I. These shows the predicted moment to failure against; age, body mass, cross-sectional area, and length of the femur for the tested paediatric cohort under internal loading condition.

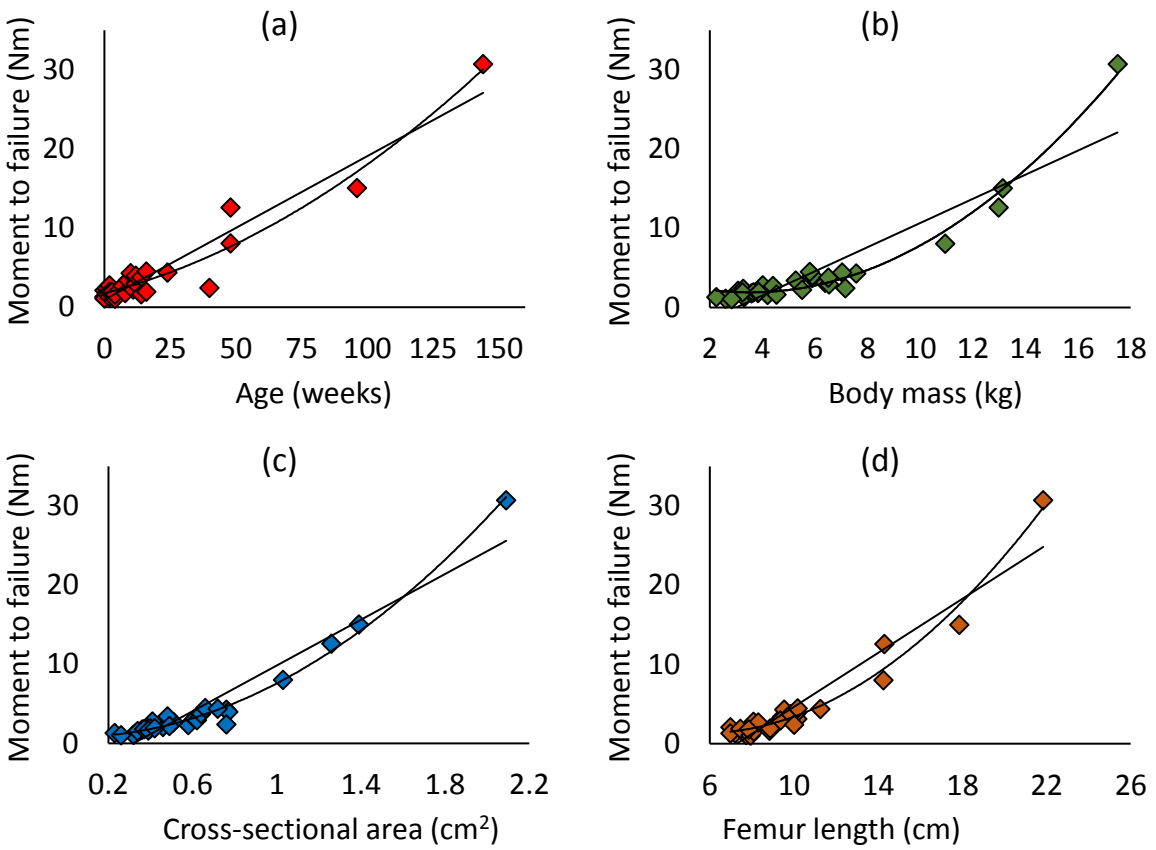

Regression equations:

$M = a \times w + b$

$M = A \times w^2 + B \times w + C$

where M is the moment to failure, w is the body mass or age, parameters a, b, A, B, C are shown below

	Linear regression	R^2	Quadratic regression	R^2
(a) Age	a= 0.182 b= 0.938	0.91	A=0.001 B=0.086 C=1.766	0.94
(b) Body mass	a= 1.524 b=- 4.572	0.84	A=0.141 B=- 0.992 C=3.654	0.98
(c) Cross-sectional area	a= 14.447 b=-4.601	0.91	A=7.092 B=0.310 C=0.804	0.99
(d) Femur length	a= 1.705 b=-12.396	0.90	A=0.108 B=-1.196 C=4.626	0.97

Figure A.1 Predicted moment to failure under internal rotation (Nm) plotted against (a) age, (b) body mass, (c) cross-sectional area, and (d) femur length. Two possible regressions were stated: linear and quadratic. The outlier (case 26) is indicated with a cross in each graph.

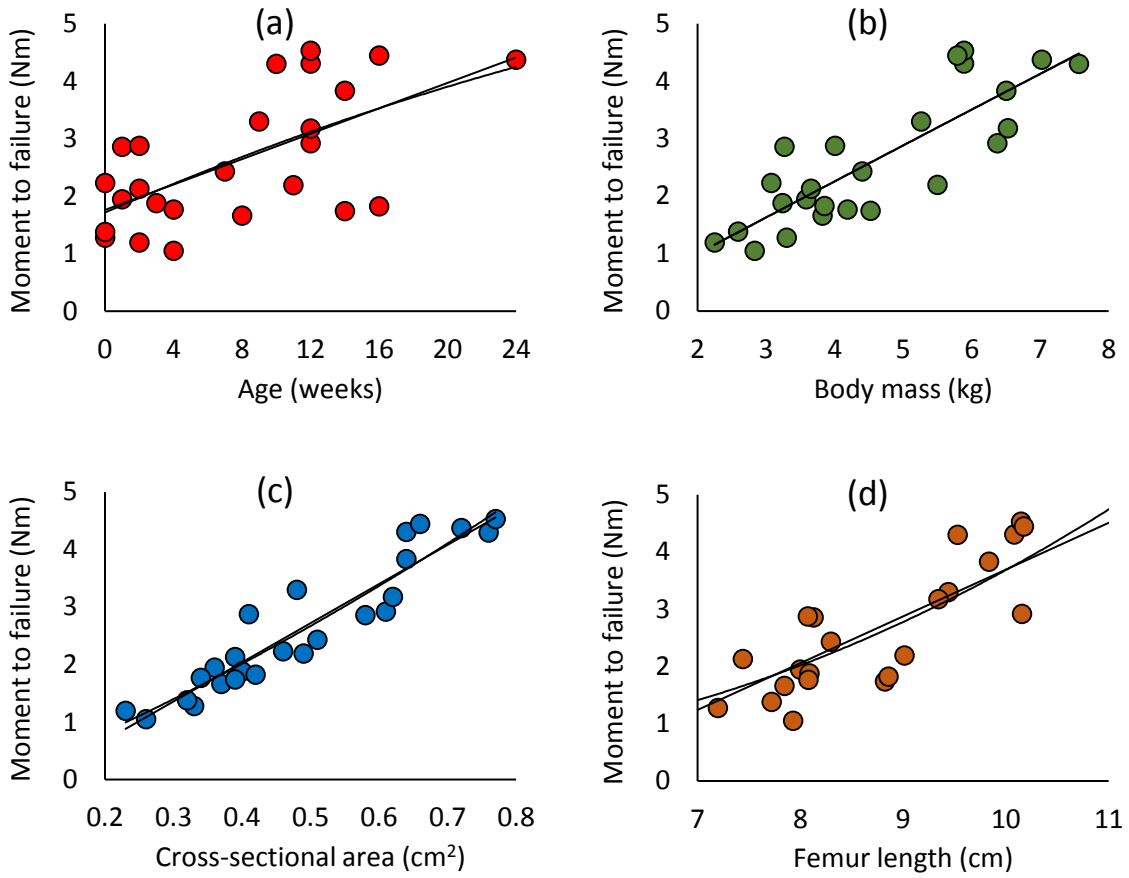

Regression equations:

$M = a \times w + b$

$M = A \times w^2 + B \times w + C$

where M is the moment to failure, w is the body mass or age, parameters a, b, A, B, C are shown below

	Linear regression	R^2	Quadratic regression	R^2
(a) Age	a= 0.116 b= 1.622	0.47	A=0.001 B=0.138 C=1.566	0.47
(b) Body mass	a= 0.622 b=- 0.330	0.75	A=-0.003 B= 0.595 C=-0.270	0.75
(c) Cross-sectional area	a= 6.809 b=-0.684	0.89	A=2.077 B=4.693 C=-0.196	0.89
(d) Femur length	a= 0.817 b=-4.477	0.70	A=0.075 B=- 0.514 C=1.342	0.71

Figure A.2 Moment to failure (Nm) under internal rotation against (a) age, (b) body mass, (c) cross-sectional area, and (d) femur length. The plotted data is for age ranged between zero and six months old to illustrate the trend in the very young infant age range.